Lawrence Berkeley National Laboratory
Recent Work

Title

DC SQUIDS as Radio-Frequency Amplifiers and Application to the Detection of Nuclear Quadrupole Resonance

Permalink

https://escholarship.org/uc/item/3053f0c6

Author

Hilbert, C.

Publication Date

1985-11-01

Lawrence Berkeley Laboratory

UNIVERSITY OF CALIFORNIA

Materials & Molecular Research Division

DC SQUIDS AS RADIO-FREQUENCY AMPLIFIERS AND
APPLICATION TO THE DETECTION OF NUCLEAR
QUADRUPOLE RESONANCE

C. Hilbert
(Ph.D. Thesis)

November 1985

DISCLAIMER

DC SQUIDS AS RADIO-FREQUENCY AMPLIFIERS AND

APPLICATION TO THE DETECTION OF NUCLEAR QUADRUPOLE RESONANCE

Claude Hilbert

Ph.D. Thesis

Department of Physics
University of California
Berkeley, CA 94720

and

Materials and Molecular Research Division
Lawrence Berkeley Laboratory
Berkeley, CA 94720

November, 1985

DC SQUIDS AS RADIO-FREQUENCY AMPLIFIERS

AND APPLICATION TO THE DETECTION OF NUCLEAR QUADRUPOLE RESONANCE

Claude Hilbert

Abstract

The high sensitivity of dc SQUID amplifiers is extended to the radio-frequency range. We perform a detailed investigation of the dynamic input impedance of tightly coupled dc SQUIDs and of the influence of parasitic capacitance between the SQUID and the input circuit on the SQUID characteristics. The reactive part of the dynamic input impedance is found to be determined by the inductive coupling, whereas the resistive part is found to be dominated by capacitive feedback. We also discuss the optimization of the input circuits for both tuned and untuned amplifiers and derive expressions for the optimum source resistance, gain and noise temperature for a given frequency, input coil and coupling. The performance of the amplifiers designed according to these prescriptions is measured. The gain of an untuned amplifier operated at 100 MHz at 4.2K is 16.5 ± 0.5dB with a noise temperature of 3.8 ± 0.9K; at 1.5K the gain increases to 19.5 ± 0.5dB while the noise temperature decreases to 0.9 ± 0.4K. A tuned amplifier operated at 93 MHz and 4.2K has a gain of 18.6 ± 0.5dB and a noise temperature of 1.7 ± 0.5K. These results are in good agreement with predicted values.

The usefulness of these sensitive amplifiers for the detection of magnetic resonance is demonstrated. A SQUID system for pulsed nuclear quadrupole resonance at about 30 MHz is developed. At a bath temperature of 4.2K, a total system noise temperature of 6 ± 1K is achieved, with a quality factor Q of 2,500. A novel Q-spoiler, consisting of an

array of Josephson tunnel junctions, reduces the ring-down time of the pick-up circuit after each pulse. The minimum number of nuclear Bohr magnetons observable after a single pulse is about 2×10^{16} in a bandwidth of 10 kHz. Finally the low-noise SQUID amplifiers make it possible to use a novel technique for observing magnetic resonance in the absence of an externally applied radio-frequency field, by measuring the spectral density of the Nyquist noise current in a tuned circuit coupled to the sample. In thermal equilibrium, a dip is observed in the spectral density at the spin resonant frequency. For zero spin polarization, on the other hand, a bump in the spectral density is observed. This bump is due to temperature-independent fluctuations in the magnetization, and represents spontaneous emission from the spins into the circuit.

John Clarke

October 21, 1985

Acknowledgements

First I want to thank especially Professor John Clarke, my thesis adviser, for his invaluable guidance and advice. This work would not have been possible without his scientific input. I also thank Professor Erwin L. Hahn. His enthusiasm and encouragement was always a great source of inspiration. Special thanks must also go to John M. Martinis who initiated me to the delicate art of SQUID fabrication, and to Tycho Sleator whose collaboration was essential for the success of the magnetic resonance experiments.

I also want to thank Rita Jones who typed most of this thesis, and Gloria Petalowski who patiently drew all the figures for it.

I wish to express my appreciation to all my colleagues, past and present, in the Clarke group for their help and their friendship.

Although a few words cannot do justice to them, I also would like to thank my parents and my wife Sara for their support and encouragement over the years.

TABLE OF CONTENTS

CHAPTER I

INTRODUCTION

The dc SQUID [Superconducting QUantum Interference Device] first appeared in 1964 (Jaklevic et al., 1964). As shown in Fig. 1.1(a), a dc SQUID consists of two Josephson junctions (Josephson, 1962) of critical current I_0 and self-capacitance C interrupting a superconducting loop of inductance L. In order to eliminate hysteresis on the current-voltage (I-V) characteristic of the SQUID, it is necessary to add an external shunt resistance R to each junction such that $\beta_c = 2\pi I_0 R^2 C/\Phi_0 \lesssim 1$ (Stewart, 1968), where $\Phi_0 = h/2e \approx 2\times10^{-15}$ Wb is the flux quantum. The maximum current that can pass through the dc SQUID without producing a voltage V across it, oscillates as a function of the magnetic flux Φ threading the loop with a period Φ_0. As Φ is slowly varied, the I-V characteristic modulates between the two extrema shown in Fig. 1.1(b). In normal operation one biases the SQUID with a constant current I_B in the non-zero voltage regime. In this situation the voltage V is periodic in Φ as indicated in Fig. 1.1(c), and any change in flux Φ is transformed into a voltage change at the SQUID output. Thus the SQUID is essentially a flux-to-voltage transducer with a transfer function $V_\Phi = (\partial V/\partial\Phi)_I$ that is a maximum when the SQUID is biased with a constant flux Φ_B close to $(2n+1)\Phi_0/4$ where n is an integer.

The potential of this device as a sensitive magnetometer, and hence as a detector of many other physical quantities, was immediately recognized. In most practical applications, the SQUID is coupled to a superconducting input coil and can be used to measure, for example, magnetic fields, magnetic field gradients, magnetic susceptibilities,

(a)

$\phi = n\phi_0$

$\phi = (n+1/2)\phi_0$

(c)

ϕ/ϕ_0
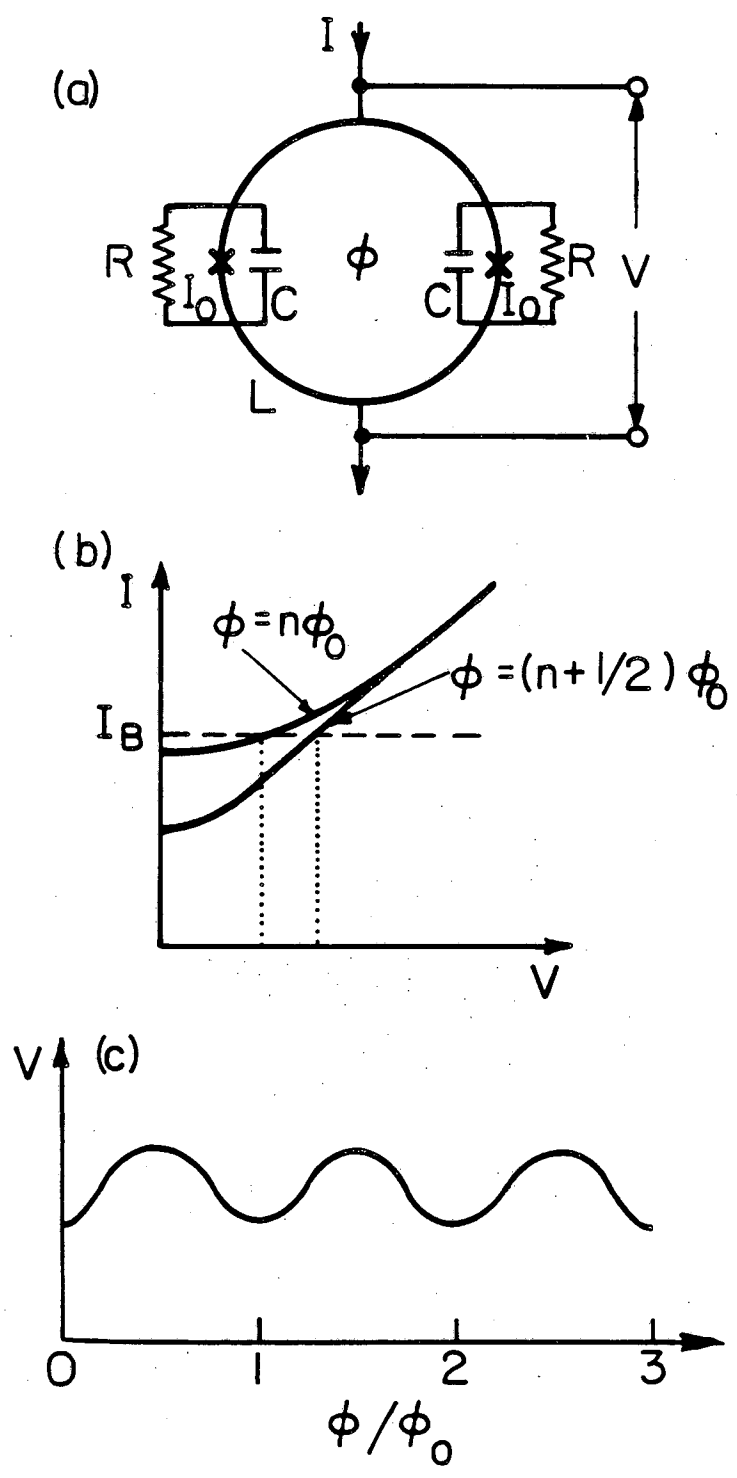
XBL 802-4740

Fig. 1.1 (a) Configuration of dc SQUID.
(b) Current-voltage (I-V) characteristic with $\Phi = n\Phi_0$ and $(n+1/2)\Phi_0$.
(c) V versus Φ at constant bias current.

currents, voltages, displacements, gravity waves and so on. They are being applied in a variety of fields ranging from magneto-tellurics to biomagnetism. In the past, however, most applications have been limited to frequencies below, say, a few tens of kilohertz.

It is the purpose of this work to extend the high sensitivity of dc SQUID amplifiers into the radio-frequency range, and to demonstrate the usefulness of these devices in such new fields of applications as the detection of magnetic resonance, or the amplification of the intermediate frequency for mixers based on superconductor-insulator-superconductor quasiparticle tunnel junctions. However, as will be shown in the following chapters, the development of this new radio-frequency amplifier made it necessary to address a whole new set of problems concerning dc SQUIDs, that had not been of importance in the low frequency range.

In Chapter II we will summarize a theory for the signal and noise in a dc SQUID amplifier coupled to an input circuit that is based on a lumped circuit approximation and was developed by Martinis and Clarke (1985). In Chapter III we will briefly describe our SQUID amplifiers and the fabrication procedures. Chapter IV examines the validity of the lumped circuit approximation used in the above-mentioned theory, and describes in detail measurements of the dynamic input impedance of a dc SQUID and the effects of the parasitic capacitance existing between the SQUID and the input circuit on the SQUID characteristics. The impedance reflected by the dc SQUID into the coupled input circuit may be unimportant for many low frequency applications, but plays a major role in the design of radio-frequency amplifiers. In Chapter V we present a theory for the optimization of the input circuit and the performance of radio-

frequency amplifiers based on dc SQUIDs, both in the tuned and untuned case. Chapter VI describes the experimental measurements of the actual performance of our dc SQUID amplifiers at radio-frequencies, and compares the results to the theoretical predictions. The remaining part of this Thesis describes two applications of these sensitive radio-frequency amplifiers in the field of magnetic resonance. In Chapter VII we describe the development of a dc SQUID system for the direct detection of pulsed nuclear quadrupole resonance around 30 MHz and analyze its performance. This particular application also required the use of a novel Q-spoiler, consisting of a series array of Josephson tunnel junctions that will be described. Finally Chapter VIII introduces a new technique for observing magnetic resonance in the absence of any externally applied radio-frequency fields, by simply measuring the current fluctuations in a tuned RLC-circuit containing the sample. In this way magnetic resonance has been detected with the sample in thermal equilibrium. Finally, by first saturating the spins, we have achieved the first observation of nuclear spin fluctuations.

CHAPTER II

SIGNAL AND NOISE THEORY FOR A COUPLED DC SQUID

1. Introduction

As mentioned in Chapter I, we will present here a theory for dc SQUID amplifiers developed by Martinis and Clarke (1985). This basic theory is necessary for the understanding of the present thesis. It generalizes the theory proposed by Clarke, Tesche, and Giffard (1979) for weakly coupled SQUIDs to SQUID amplifiers with arbitrarily large coupling to the input circuit.

This theory attempts to construct an equivalent circuit model for the amplification and noise properties of a dc SQUID coupled to an input circuit and to an output circuit. Such a model is desirable because the exact solution of the nonlinear circuit equations on a computer for given input and output circuits is time consuming, and must be repeated for a range of circuit parameters to enable one to optimize the parameter values. The approach adopted by Martinis and Clarke (1985), and described in Sec. 2, is to break up the full equations of motion into linear and nonlinear parts. The nonlinear part is assumed to be solved on a computer for the transfer functions and noise parameters that are then used in the equivalent circuit model obtained from the linear part of the equations. The equivalent circuit model and the values of the transfer functions and noise parameters depend on how the equations are divided into linear and nonlinear parts. Within the approximations made in Sec. 2, this division is made so that the nonlinear part describes a "reduced SQUID" (Koch, 1982; Tesche, 1982a, 1983a, 1983b) with a reduced inductance that depends only on the

effective coupling coefficient to the input circuit, and is independent of frequency. As a result, one is required to compute the transfer functions and noise parameters for a single value of inductance only; these values can be used in the equivalent circuit model that enables one to optimize the circuit parameters in a straightforward way.

In Sec. 3 we comment briefly on a formal method of incorporating the effects of parasitic capacitance into the theory, while Sec. 4 contains a concluding discussion.

2. Theory of the Coupled dc SQUID

2.1 Model Circuit

Our model for an amplifier involving a dc SQUID is shown in Fig. 2.1. The SQUID consists of two identical Josephson tunnel junctions, each with a critical current I_o, a self-capacitance C, and a shunt resistance R. The SQUID is biased with a constant current I, and develops a voltage $V(t)$ across the input impedance, Z_A, of the next stage, which might be a transformer, a tuned circuit or a preamplifier. The SQUID loop, which has an inductance L, is coupled to the inductance L_i of the input circuit via a mutual inductance $M_i = \alpha(LL_i)^{1/2}$. The input circuit contains a pick-up loop with inductance L_p, a stray inductance, L_s, a capacitance C_i, and a resistance R_i. Thus, the total impedance of the input circuit is

$$Z_T(\omega) = R_i + 1/j\omega C_i + j\omega(L_i + L_p + L_s)$$

$$= R_i + 1/j\omega C_i + j\omega L_T. \tag{2.1}$$
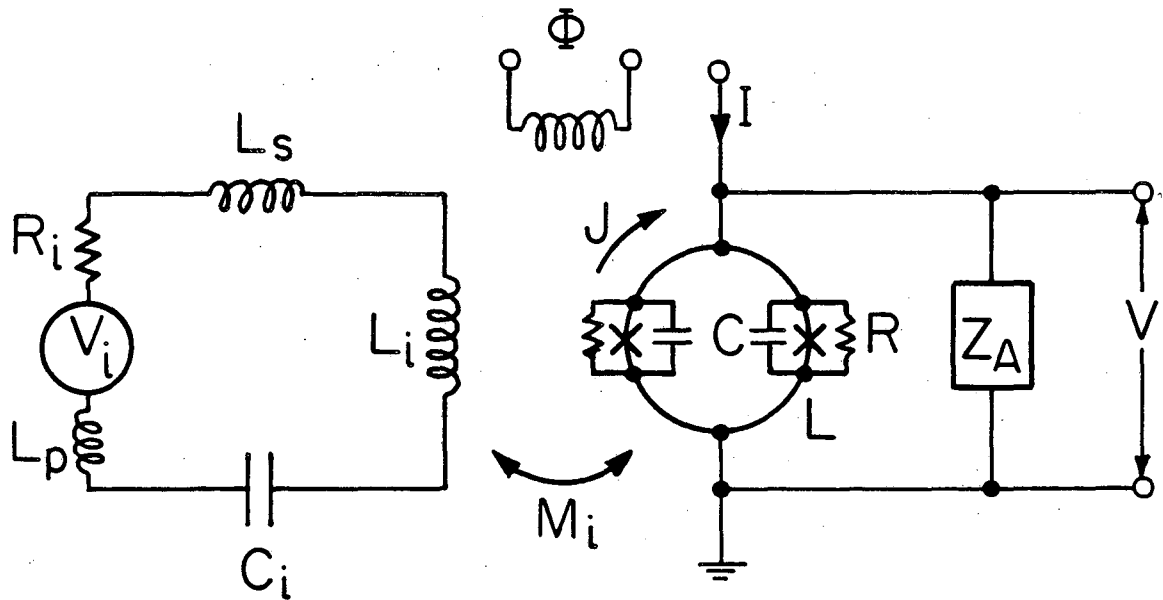
XBL 853-5937

Fig. 2.1   Model circuit for a voltage amplifier based on a dc SQUID.

The input voltage, V_i, could arise from a voltage source (the resistance of which is included in R_i) or from a time-varying magnetic flux in the pick-up coil. By choosing L_p, C_i and R_i appropriately, one can use this circuit to represent a voltage amplifier or a magnetometer, tuned or untuned.

The circuit shown in Fig. 2.1 neglects parasitic capacitance, for example, between turns of the input coil or between the input coil and the SQUID, that may have a significant effect on the dynamics of the SQUID at the Josephson frequency. These effects may be particularly important for thin-film devices with tightly coupled input coils. The lumped circuit model is expected also to break down if the wavelength at the Josephson frequency becomes comparable with the dimensions of the input circuit. At the signal frequency, which we assume to be much less than the Josephson frequency, the parasitic capacitances should be relatively unimportant. For the moment, we neglect these parasitic effects, and concern ourselves with developing a solution to the equations of motion that describe Fig. 2.1.

2.2 Equations of Motion for the Coupled dc SQUID

In the time domain, the equations of motion for the SQUID coupled to an input circuit are

$$V(t) = [\dot{\delta}_1(t) + \dot{\delta}_2(t)]\hbar/4e, \tag{2.2}$$

$$\frac{\hbar C}{2e}\ddot{\delta}_1(t) + \frac{\hbar}{2eR}\dot{\delta}_1(t) = I_1(t) - J(t) - I_0\sin\delta_1(t) + I_{N1}(t), \tag{2.3}$$

$$\frac{\hbar C}{2e}\ddot{\delta}_2(t) + \frac{\hbar}{2eR}\dot{\delta}_2(t) = I_2(t) + J(t) - I_0\sin\delta_2(t) + I_{N2}(t), \tag{2.4}$$

$$I_1(t) + I_2(t) = I - \overline{Z_A^{-1}(\omega)} * V, \tag{2.5}$$

and

$$[\delta_1(t) - \delta_2(t)]\Phi_0/2\pi = \Phi + LJ(t) + M_i I_i(t), \qquad (2.6)$$

where $\dot{\delta} \equiv \partial\delta/\partial t$, $\ddot{\delta} \equiv \partial^2\delta/\partial t^2$, $\bar{f}$ denotes the Fourier transform of f, and $(f * g)(t)$ denotes the convolution $(2\pi)^{-1/2} \int_{-\infty}^{+\infty} f(t')g(t - t')dt'$. In these equations, V is the voltage across the SQUID, J is the current around the SQUID loop, Φ is the externally applied magnetic flux, and I_i is the current in the input circuit. The phase differences across the junctions are δ_1 and δ_2, the currents through these junctions are I_1 and I_2, and the noise currents produced by the shunt resistors are I_{N1} and I_{N2}. The equations are identical to those used previously to describe the bare dc SQUID (Tesche and Clarke, 1977), with the addition of the last (linear) term on the right hand side of Eqs. (2.5) and (2.6) which account for the loading of the SQUID by the next stage and for the influence of the input circuit (Koch, 1982; Tesche, 1982a, 1983a, 1983b), respectively.

In the frequency domain, the current $J(\omega)$ in the SQUID loop induces a voltage $-j\omega M_i J(\omega)$ into the input circuit, so that

$$I_i(\omega) = [V_i(\omega) - j\omega M_i J(\omega)]/Z_T(\omega). \qquad (2.7)$$

In order to resolve the equations into linear and nonlinear parts, we now introduce low and high frequency filter functions, $[\ ]_{LF}$ and $[\ ]_{HF}$, into the terms that represent the coupling of the SQUID to the input and output circuits. The cutoff frequencies of these filter functions are chosen to lie between the signal and Josephson frequencies in

order to separate effects at the signal frequency from those at the Josephson frequency. Thus, we rewrite Eqs. (2.5)-(2.7) in the form

$$I_1(t) + I_2(t) = I - [\overline{Z_A^{-1}(\omega)} * V]_{LF} - [\overline{Z_A^{-1}(\omega)} * V]_{HF} \qquad (2.8)$$

and

$$[\delta_1(t) - \delta_2(t)]\Phi_0/2\pi = \Phi + LJ + \{-[\overline{j\omega M_i^2/Z_T(\omega)}] * J + [\overline{M_i/Z_T(\omega)}] * V_i\}_{LF}$$

$$- \{[\overline{j\omega M_i^2/Z_T(\omega)}] * J\}_{HF}. \qquad (2.9)$$

To simplify Eqs. (2.8) and (2.9), we introduce two assumptions. The first is that the output loading of the SQUID is negligible at the Josephson frequency, $\omega_J/2\pi$, so that the high frequency term in Eq. (2.8) is negligible. The second assumption is that $R_i, |1/j\omega_J C_i| \ll |j\omega_J L_T|$, so that $Z_T(\omega_J) = j\omega_J L_T$. Under this assumption, the high frequency term in Eq. (2.9) becomes $[-\alpha_e^2 LJ]_{HF}$, where

$$\alpha_e^2 = M_i^2/LL_T, \qquad (2.10)$$

is an effective coupling coefficient involving the total inductance of the input circuit. To solve the nonlinear equations of motion for a SQUID inductance that is independent of frequency and the input circuit, by using $J = J_{LF} + J_{HF}$ we make the separation

$$[-\alpha_e^2 LJ]_{HF} = -\alpha_e^2 LJ + [\alpha_e^2 LJ]_{LF}. \qquad (2.11)$$

Because the $[\ ]_{LF}$ terms in Eqs. (2.8) and (2.9) are at frequencies much less than the Josephson frequency, these terms can be regarded as

small changes ΔI and $\Delta\Phi$ in the bias parameters I and Φ. We can then rewrite Eqs. (2.8) and (2.9) as

$$I_1(t) + I_2(t) = I + \Delta I(t) \qquad (2.12)$$

and

$$[\delta_1(t) - \delta_2(t)]\Phi_0/2\pi = \Phi + (1 - \alpha_e^2)LJ + \Delta\Phi(t), \qquad (2.13)$$

where

$$\Delta I(t) = - [\overline{Z_A^{-1}(\omega)}] * V]_{LF}, \qquad (2.14)$$

and

$$\Delta\Phi(t) = \{[\overline{M_i/Z_T(\omega)}] * V_i - [\overline{j\omega M_i^2/Z_T(\omega)}] * J + \alpha_e^2 LJ\}_{LF}. \qquad (2.15)$$

With $\Delta I = \Delta\Phi = 0$, Eqs. (2.3), (2.4), (2.12), and (2.14) are the equations of motion for a reduced SQUID (Koch, 1982; Tesche, 1982a, 1983a, 1983b) with an inductance $(1 - \alpha_e^2)L$: The inductance is reduced by the shielding effect of the input circuit which we have assumed to be purely inductive at the Josephson frequency.

In the next section, we describe a method for solving the equations of motion.

2.3 The Linear Approximation

To solve for the effects of the input and output circuits using the linear approximation, we initially set $\Delta I = \Delta\Phi = 0$ and solve Eqs. (2.2)-(2.4), (2.12) and (2.13) for the set of low frequency transfer

functions that represent time-averages over the voltage and current at the Josephson frequency, $V_\Phi^r \equiv (\partial V/\partial \Phi)^r$, $V_I^r \equiv (\partial V/\partial I)^r$, $J_\Phi^r \equiv (\partial J/\partial \Phi)^r$ and $J_I^r \equiv (\partial J/\partial I)^r$, and for the voltage and current noise terms $V_N^r(t)$ and $J_N^r(t)$. The superscript "r" implies that these quantities are computed for a SQUID with reduced inductance $(1 - \alpha_e^2)L$. We note that, in general, the transfer functions will contain both real and imaginary components (Hilbert and Clarke, 1985a; MacDonald, 1984). The noise terms are characterized by the low frequency spectral densities S_V^r and S_J^r and cross-spectral density S_{VJ}^r.

We now reintroduce the <u>low frequency</u> terms ΔI and $\Delta \Phi$ by regarding them as small changes in the bias parameters. We use the small signal, linear approximation to find the new output voltage and circulating current at low frequency with these terms included:

$$V(t) = V_N^r(t) + V_\Phi^r \Delta\Phi(t) + V_I^r \Delta I(t) \tag{2.16}$$

and

$$J(t) = J_N^r(t) + J_\Phi^r \Delta\Phi(t) + J_I^r \Delta I(t). \tag{2.17}$$

Inserting Eqs. (2.13) and (2.15) into Eqs. (2.16) and (2.17), we obtain, at low frequency,

$$
\begin{bmatrix} V(\omega) \\ J(\omega) \end{bmatrix} = \begin{bmatrix} \dfrac{-V_I^r}{Z_A(\omega)} & V_\Phi^r\left[\dfrac{-j\omega M_i^2}{Z_T(\omega)} + \alpha_e^2 L\right] \\ \dfrac{-J_I^r}{Z_A(\omega)} & J_\Phi^r\left[\dfrac{-j\omega M_i^2}{Z_T(\omega)} + \alpha_e^2 L\right] \end{bmatrix} \begin{bmatrix} V(\omega) \\ J(\omega) \end{bmatrix} + \begin{bmatrix} V_N^r(\omega) + \dfrac{V_\Phi^r M_i V_i(\omega)}{Z_T(\omega)} \\ J_N^r(\omega) + \dfrac{J_\Phi^r M_i V_i(\omega)}{Z_T(\omega)} \end{bmatrix}. \tag{2.18}
$$

The linear Eqs. (2.18) can be solved in a straightforward manner. To focus attention on the interaction of the input circuit and the SQUID

and to simplify the solution, we consider the limit $Z_A(\omega) \to \infty$ in which the loading of the SQUID by the following circuitry is negligible. This is an excellent approximation for the amplifiers studied in this thesis. In this limit, we solve Eqs. (2.18) to find

$$V(\omega) = V_N^r(\omega) + M_i V_\phi^r \left[\frac{V_i(\omega) + M_i J_N^r(\omega)(R_i + 1/j\omega C_i)/L_T}{Z_T(\omega) - J_\phi^r M_i^2 (R_i + 1/j\omega C_i)/L_T} \right] . \quad (2.19)$$

Equation (2.19) expresses the output voltage in terms of reduced SQUID parameters that are dependent only on the effective coupling coefficient, α_e, and are otherwise independent of the input circuit. Thus, one can readily use Eq. (2.19) to optimize the component values for any type of input circuit. The second term in square brackets represents the noise current flowing in the input circuit in the equivalent circuit model: this current produces a flux in the SQUID and thus an additional voltage noise at the output. The term $-J_\phi^r M_i^2 (R_i + 1/j\omega C_i)/L_T$ in the denominator represents the modification of the input circuit by the presence of the SQUID. This term modifies both the signal and noise measured at the output of the SQUID.

3. Effects of Parasitic Capacitance

Practical SQUID amplifiers generally contain parasitic capacitances, for example, among the turns of the input coil or between the input coil and the SQUID. As a result, even when the input coil is open-circuited, the high frequency dynamics, and therefore the low frequency transfer coefficients and noise, may differ from those for a bare SQUID. One common manifestation of these parasitic effects is the appearance of structure on the current-voltage characteristics (Hilbert and Clarke, 1985a; Muhlfelder and Johnson, 1984). Because these capacitances are

distributed, it is difficult to incorporate their effects into the equation of motion. However, in a formal sense one can allow for these effects, together with any other parasitic effects due to the breakdown of the simple lumped circuit of Fig. 2.1, by replacing $Z_A^{-1}(\omega)$ and $j\omega M_i^2/Z_T(\omega)$ in the high frequency parts of Eqs. (2.9) and (2.10) with the functions $U_A(\omega)$ and $U_i(\omega)$, respectively, to obtain

$$I_1(t) + I_2(t) = I - [\overline{Z_A^{-1}(\omega)} * V]_{LF} - [\overline{U_A(\omega)} * V]_{HF}, \qquad (2.20)$$

and

$$[\delta_1(t) - \delta_2(t)]\Phi_0/2\pi = \Phi + LJ + \{-[\overline{j\omega M_i^2/Z_T(\omega)}] * J + [\overline{M_i/Z_T(\omega)}] * V_i\}_{LF}$$

$$- [\overline{U_i(\omega)} * J]_{HF}. \qquad (2.21)$$

If $U_A(\omega)$ and $U_i(\omega)$ are known, one can proceed as in Sec. 2, and, at least in principle, the problem can be solved.

As a simple example, we consider the limiting case $U_A(\omega_J) = U_i(\omega_J) = 0$, that is, that no currents at the Josephson frequency flow in the input circuit or in the stage following the SQUID. The result can be found easily using the approach of Sec. 2 and by noting that the reduced SQUID parameters are replaced with the bare SQUID parameters. For the case $Z_A(\omega) \to \infty$, one finds

$$V(\omega) = V_N(\omega) + M_i V_\Phi \left[\frac{V_i - j\omega M_i J_N(\omega)}{Z_T(\omega) + j\omega M_i^2 J_\Phi} \right]. \qquad (2.22)$$

The form of the equivalent circuit model of Eq. (2.22) differs from that of Eq. (2.19) because of the way in which the high frequency parts of

the SQUID inductance were treated in the two approximations. We note that if one writes (Koch, 1982) $J_\phi = - j\omega/\mathcal{J}$, where $\mathcal{J}(\omega)$ is the dynamic impedance of the SQUID loop, the reflected SQUID impedance $j\omega M_i^2 J_\phi$ becomes $\omega^2 M_i^2/\mathcal{J}$.

4. Discussion

We have presented a theory for the gain and noise properties of an amplifier based on a dc SQUID. The central results are Eqs. (2.19) and (2.22). In a real SQUID, it is likely that neither of these equations is exactly applicable. Which of the two results is the more appropriate is likely to depend on the details of the structure of the SQUID and its input coil, and on the conditions under which the SQUID is operated. Thus the question of whether to use Eq. (2.19) or Eq. (2.22) to optimize the input circuit and noise temperature of the SQUID amplifier can only be answered experimentally. For this reason, the detailed discussion of the optimization of SQUID amplifiers has been deferred until Chapter V. The following two chapters are devoted to the description of our SQUID amplifiers and the experimental investigation of the effects of parasitic capacitance, the validity of the lumped circuit model, and measurements of the impedance induced into the input circuit by the presence of the SQUID.

CHAPTER III

FABRICATION OF DC SQUID AMPLIFIERS

Before we study in detail the effects of parasitic capacitance on the SQUID characteristics and the validity of the lumped circuit model used in the previous chapter, a brief description of our SQUID amplifiers and the fabrication procedures is in order.

The dc SQUIDs used in our experiments are planar, thin-film devices which are tightly coupled to a superconducting spiral input coil (Fig. 3.1). They are similar in design to the devices described by Dettmann et al. (1979), Ketchen and Jaycox (1982), and Martinis and Clarke (1983). The SQUIDs were fabricated in batches of 9 on oxidized Si wafers using standard photolithography. The first step was to deposit a 30-nm-thick Au (25wt%Cu) film patterned to produce the resistive shunts. Next we sputtered a 100-nm-thick Nb film, and etched it to form the SQUID loop and a strip that eventually made contact to the inner end of the spiral coil. The third film was a 200-nm-thick double layer of SiO, with two 2-μm-diameter windows for the junctions, a larger window to give access to the CuAu shunt, and a window at each end of the Nb strip to provide connections to the spiral coil. To improve adhesion, the deposition of the SiO films was preceded by the evaporation of ~ 1 nm of Cr. We then sputtered a 300-nm-thick Nb film which was etched to form the spiral input coil with the desired number of turns. At this point, the wafer was diced to produce 9 chips each with a single device, and the remaining steps were carried out on individual SQUIDs. The individual devices were ion-milled to clean the exposed areas of Nb and CuAu, and the niobium was oxidized with a 300-V rf-discharge in an Ar

100 μm

Nb→

20 Turn
Nb Input Coil

Pb

Windows
in SiO

Nb

Pb

Cu Au Shunts

10 μm
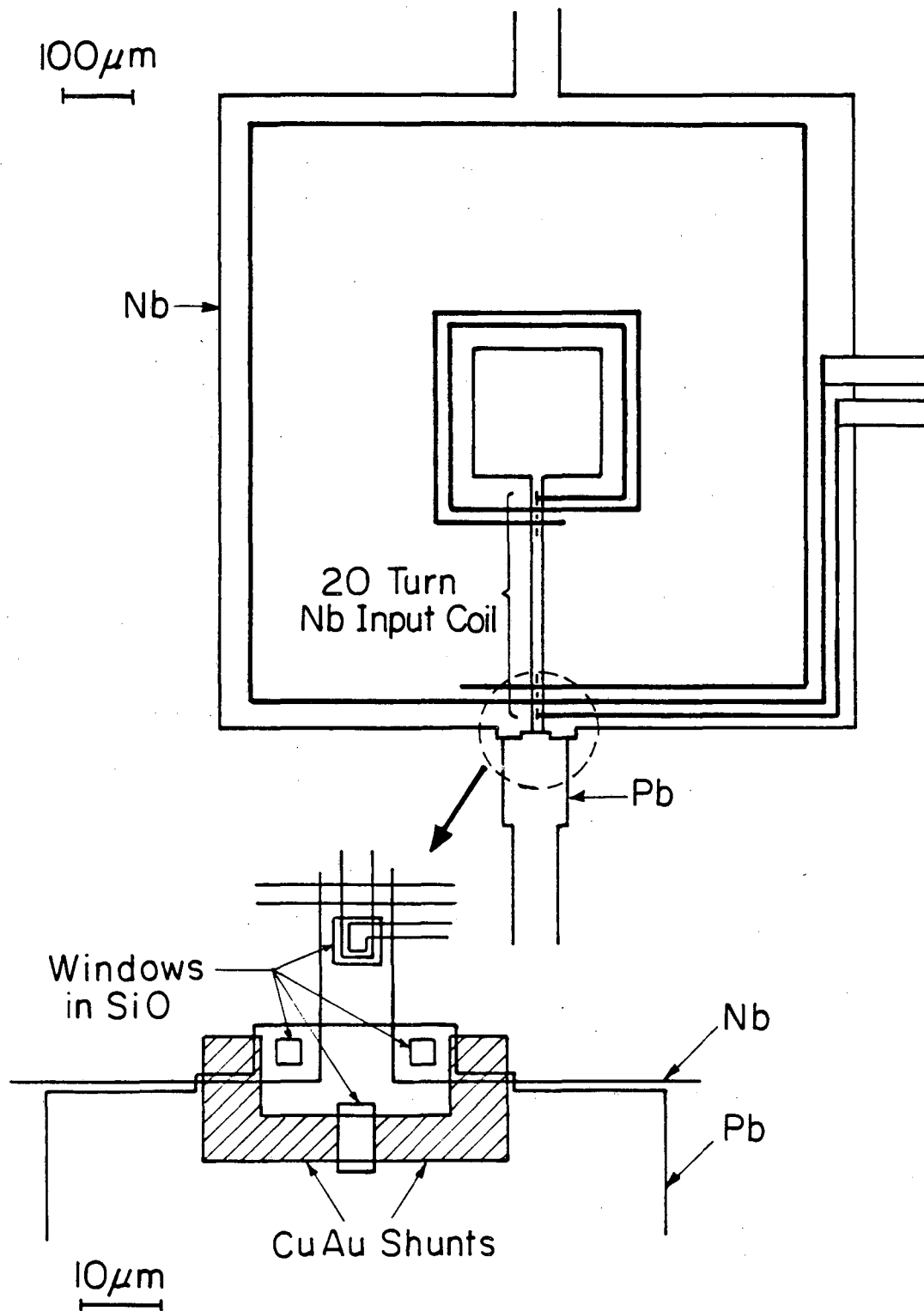
Fig. 3.1 Configuration of planar dc SQUID with 20-turn spiral input
coil.

($5vol\%O_2$) atmosphere. The 300-nm-thick Pb (5wt%In) counterelectrode was deposited and lifted off, thereby completing the junctions and making contact with the shunts. Finally, a 200-nm-thick passivation layer of SiO was deposited. For the lift-off procedures we used Shipley 1450J photoresist submitted to a 20-minute bake at $70^{\circ}C$, a 10-minute soak in chlorobenzene at $20^{\circ}C$ and finally another 10-minute bake at $70^{\circ}C$ before exposure and development. For the etching procedures we used Shipley 1350B photoresist with a 25-minute bake at $90^{\circ}C$ before exposure and development followed by a 5-minute bake at $90^{\circ}C$.

Typical SQUID parameters were L $\approx$ 0.4 nH, I_O = 3 μA, C $\approx$ 0.5 pF and R = 8 Ω, yielding β $\approx$ 1 and $\beta_c \approx$ 0.2. Three different spiral coils were fabricated with 50, 20, and 4 turns, with inductances of 800 nH, 120 nH, and 5.6 nH, and estimated values (Hilbert and Clarke, 1984) of α^2 of o.75, 0.70, and 0.65.

Figure 3.2 shows photos of a SQUID with a 50-turn input coil. The completed device was attached to a G-10 fiberglass mount, together with an auxiliary flux bias coil, and enclosed in a superconducting Nb shield. We used superconducting pressure contacts on the input and output Nb pads.
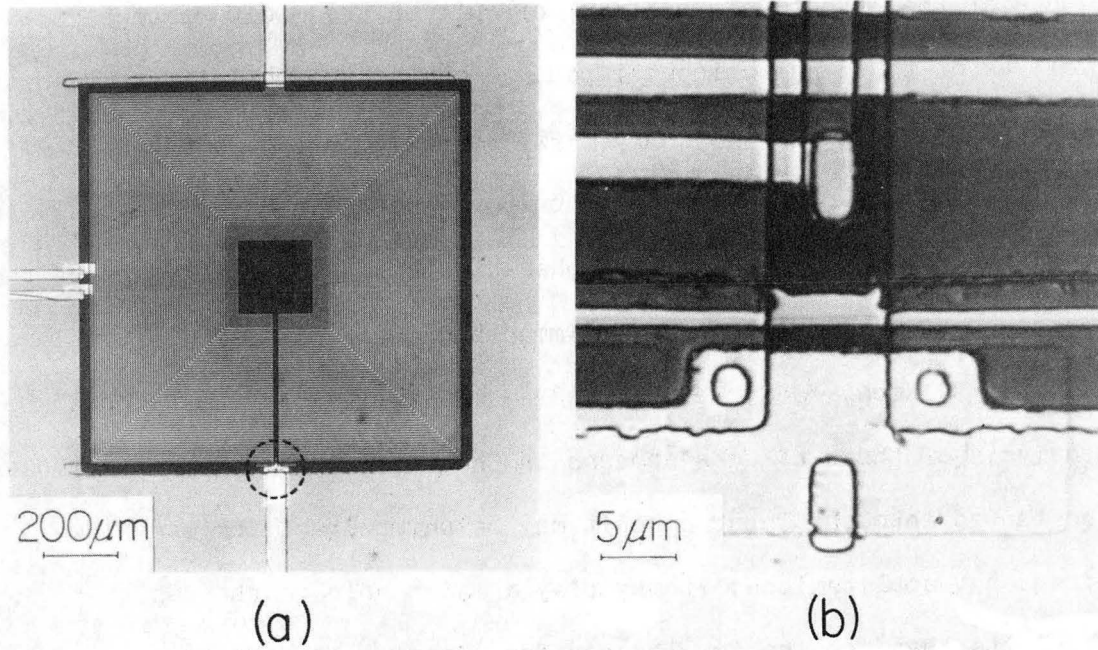
XBB 852-1563

Fig. 3.2   Photographs of dc SQUID with 50-turn spiral input coil:
           (a) complete device,
           (b) magnified view of area containing Josephson junctions
               indicated by a dashed circle in (a).

CHAPTER IV

DYNAMIC INPUT IMPEDANCE OF A DC SQUID

1. Introduction

A requirement in the optimization of SQUID amplifiers is the know-
ledge of the effects of the input circuit on the SQUID parameters, as
well as of the dynamic input impedance of the SQUID. In fact, when an
input circuit is coupled inductively to a dc SQUID to produce an ampli-
fier, one expects both an impedance to be reflected from the SQUID into
the input circuit and the SQUID characteristics to be modified by the
presence of the input circuit (Zimmerman, 1971; Claassen,1975; Clarke et
al., 1979; Koch, 1982; Tesche, 1982a, 1983a, 1983b). One approach to the
analysis of these effects appears in Chapter II. Although the impedance
reflected into the input circuit may be unimportant for many low-
frequency applications, it may play a major role in the design of
circuits that require low losses, for example, transducers for gravity
wave antennas (Boughn et al., 1977), or a precisely defined input
impedance, for example, a tuned radiofrequency amplifier (Hilbert and
Clarke, 1985a) with a high Q. The importance of determining the dynamic
input impedance of a SQUID has been long-recognized -- indeed, it has
already been measured in the rf SQUID (Giffard and Hollenhorst, 1978) --
but, to our knowledge, it has not previously been measured in the dc
SQUID.

In this chapter (Hilbert and Clarke, 1984, 1985b) we present a
detailed study of the input impedance of an amplifier based on a
thin-film dc SQUID tightly coupled to a spiral input coil, as well as of
the effects of the input circuit on the SQUID parameters. These results

should be generally applicable, to our devices as well as to other dc

SQUIDs with tightly coupled input coils. Indeed this SQUID design has

been widely adopted (Berthel and Dettmann, 1984; Ketchen and Jaycox,

1982; de Waal et al., 1983; Pegrum et al., 1985; Muhlfelder et al.,

1985; Carelli and Foglietti, 1985; Tesche et al., 1985). We begin, in

Sec. 2, by defining the dynamic input impedance, $\mathscr{J}$, of a SQUID, and in

Sec. 3 describe analog simulations of $\mathscr{J}$. Section 4 describes obser-

vations on the effect of the input circuit on the SQUID parameters. The

central part of this chapter, the measurements of $\mathscr{J}$, are presented in

Sec. 5. Section 6 contains a concluding summary.

2. Characterization of the Dynamic Input Impedance

Figure 4.1 shows a dc SQUID coupled to a tuned input circuit. When

the loading of the SQUID output by the next stage is negligible and

$\partial J/\partial I$ is assumed to be zero, as is the case for a symmetric SQUID, the

lumped circuit model presented in Chapter II [Eq. (2.19)] yields the

following expression for the voltage gain of the SQUID amplifier:

$$G_v = \frac{M_i V_\phi^r}{Z_T - \alpha_e^2 L J_\phi^r (R_i + 1/j\omega C_i)} \equiv \frac{M_i V_\phi^r}{Z_T^*} \qquad (4.1)$$

According to Eq. (4.1), an input voltage V_i induces an effective flux ϕ^*

$= M_i V_i / Z_T^*$ into the reduced SQUID.

The flux-to-current transfer coefficient of the bare SQUID, J_ϕ, can

be related to its dynamic input impedance $\mathscr{J}$ which, in general, has both

real and imaginary parts. Following Koch (1982), for frequencies $\omega/2\pi$

$\ll f_J$ we define
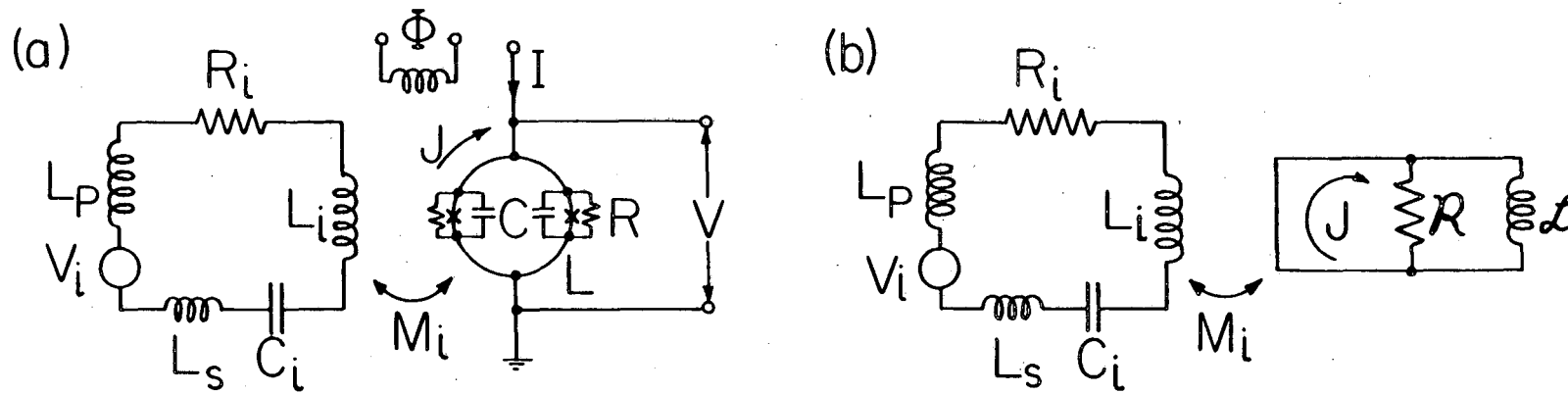
Fig. 4.1 (a) Tuned amplifier; (b) representation of dynamic input impedance of a dc SQUID.

XBL8411-8265

$$- J_\phi = \frac{j\omega}{\mathscr{Z}} = \frac{1}{\mathscr{L}} + \frac{j\omega}{\mathscr{R}} \ . \tag{4.2}$$

At $\omega = 0$, $- J_\phi$ reduces to the inverse of the dynamic inductance, $\mathscr{L}$, while for $\omega > 0$ resistive losses, represented by the dynamic resistance $\mathscr{R}$, occur. The dynamic inductance and resistance, shown schematically in Fig. 4.1(b), define the response of the current J to an applied flux ϕ. In general, $\mathscr{L}$ is very different from the geometrical inductance of the SQUID, L, which defines the flux produced by a given value of J, while $\mathscr{R}$ is also very different from R. We expect $\mathscr{L}$ and $\mathscr{R}$ to depend on both I and ϕ. In the presence of an input circuit, $\mathscr{L}$ and $\mathscr{R}$ are modified to the values $\mathscr{L}^r$ and $\mathscr{R}^r$. Combining the reduced form of Eq. (4.2) with Eq. (4.1), we obtain

$$Z_T^* = R_i\left(1 + \frac{\alpha_e^2 L}{\mathscr{L}^r}\right) + \frac{\alpha_e^2 L}{\mathscr{R}^r C_i} + j\omega\left[L_i + \alpha_e^2 L\left(\frac{R_i}{\mathscr{R}^r} - \frac{1}{\omega^2 C_i \mathscr{L}}\right) + L_p + L_s\right] + \frac{1}{j\omega C_i} \ . \tag{4.3}$$

We observe that both $\mathscr{L}^r$ and $\mathscr{R}^r$ contribute to the real and imaginary parts of Z_T^*.

In this chapter we will analyze our data in terms of Z_T^*, and we compare our experimental values of $\mathscr{Z}$, presented in Sec. 5, with those obtained from an analog simulator using both bare and reduced parameters. In this way, we can gain some insight into the importance of parasitic capacitance (Germain et al., 1984; Tesche, 1982b).
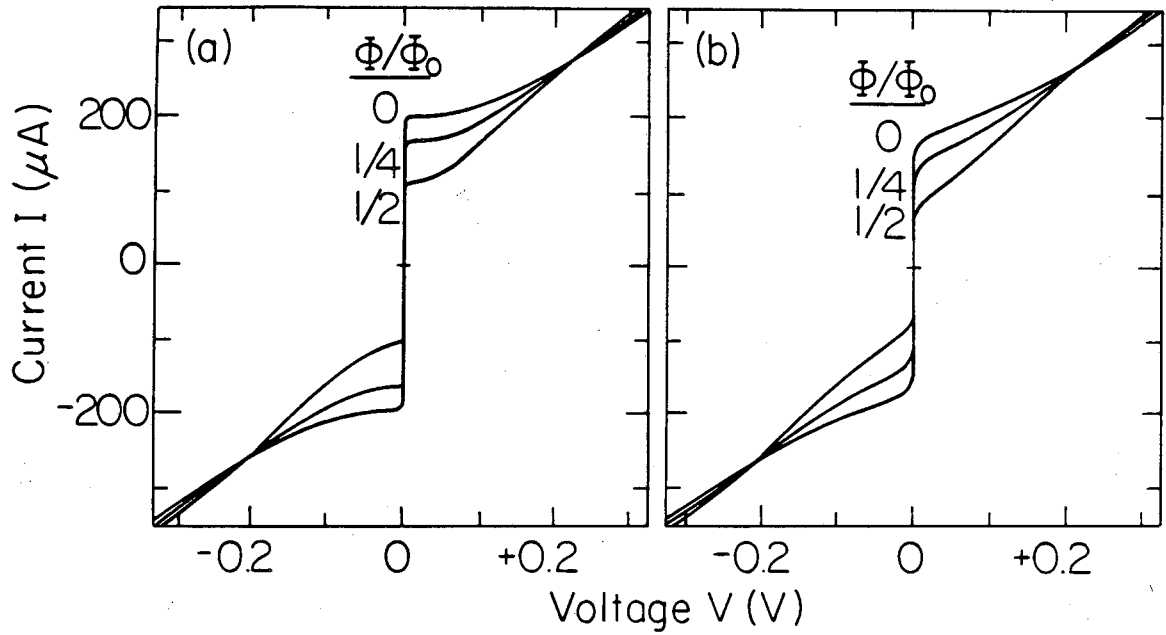

3. Analog Simulations

To carry out these simulations we used the electronic analog of the dc SQUID developed by Henry and Prober (1981), with the addition of

thermal noise. The noise was produced by two pseudo-random number generators that had white noise spectra from 0.5 Hz to 10 kHz. The simulated flux quantum, Φ_0, corresponded to 2.8×10^{-4} Wb. Typical simulator parameters were L = 1.4 H, R = 2.2 kΩ, C = 20 nF and $I_0 = 10^{-4}$ A, leading to $\beta \equiv 2LI_0/\Phi_0 = 1.0$ and $\beta_c \equiv 2\pi R^2 CI_0/\Phi_0 = 0.2$. The Josephson frequency was typically a few hundred hertz. The noise parameter $\Gamma \equiv 2\pi k_B T/I_0\Phi_0$, where T is the temperature, could be varied from 0 to 0.06, the latter value corresponding approximately to a SQUID with β = 1 at 4.2K. The uncertainties in the parameters I_0, R, C, L, Φ_0 and Γ were less than 5%, while thermal drifts produced an uncertainty of about 5% in the value of I/I_0 during the time required to acquire a set of data.

Figure 4.2 shows the I-V characteristics obtained from the simulator with and without thermal noise for the parameters listed above and for Φ/Φ_0 = 0, 0.25 and 0.5. The relative modulation depth of the critical current for Γ = 0, $\Delta I_c/2I_0 = 0.45$, is within 5% of the value obtained from digital simulations (Tesche and Clarke, 1977). The observed cross-over (de Waal et al., 1984) of the I-V curves for different values of Φ at about 0.2 V moved to lower voltages (Josephson frequenices) as C was increased, the cross-over voltage scaling approximately as $C^{-1/2}$. The cross-over was eliminated when we set C = 0. We also computed $\bar{V}(\Phi)$ and $\bar{J}(\Phi)$ as well as the noise spectral densities $S_V(f)$ and $S_J(f)$ for various bias conditions, and found agreement with digital simulations (Tesche and Clarke, 1977, 1979; Brunes et al., 1982) to within ± 10%. Thus, we demonstrated that the simulator was calibrated to within ± 10%.

We investigated the dynamic impedance of the analog SQUID by injecting a sinusoidal flux, typically at 50 Hz and with a peak-to-peak amplitude of $\Phi_0/10$, and measuring the amplitude and phase of J at the

Fig. 4.2 Current-voltage (I-V) characteristics obtained from the analog
simulator (a) without and (b) with thermal noise for 3 values
of Φ. The SQUID parameters were $\beta = 1.0$, $\beta_c \approx 0.2$, and
$\Gamma = 0$ and 0.06.

same frequency with an HP 3582 spectrum analyzer. The model shown in Fig. 4.1(b) and described by Eq. (4.2) was found to be valid for frequencies up to typically $f_J/4$, that is, the measurements yielded constant values of $\mathscr{L}$ and $\mathscr{R}$ up to that frequency.

At this point, we remark that from symmetry considerations we expect $\bar{J}(\Phi) = -\bar{J}(-\Phi)$ and hence $\mathscr{J}(\Phi) = \mathscr{J}(-\Phi)$ for a symmetric SQUID. Adding to the latter result the periodicity requirement $\mathscr{J}(\Phi) = \mathscr{J}(\Phi + \Phi_0)$, we also obtain symmetry about $\Phi_0/2$, i.e. $\mathscr{J}(\tfrac{1}{2}\Phi_0 + \Phi) = \mathscr{J}(\tfrac{1}{2}\Phi_0 - \Phi)$.

Figure 4.3 shows measured values of $L/\mathscr{L}$ and $R/\mathscr{R}$ at four values of bias current for a symmetric SQUID. The periodicity and symmetry requirements mentioned above are obviously satisfied. The dynamic inductance takes both positive and negative values; for the range of bias currents between $1.4I_0$ and $2I_0$ of practical interest; the amplitude of $L/\mathscr{L}$ varies between approximately ± 0.4. For bias points around $\pm \Phi_0/4$, where a SQUID is normally operated, $L/\mathscr{L}$ is smaller than ± 0.1. All four curves shown satisfy the requirement $\int_0^{\Phi_0} d\Phi/\mathscr{L} = 0$, that follows from the realization that $1/\mathscr{L}$ is the slope of the periodic curve $\bar{J}(\Phi)$ at zero frequency. By contrast, the dynamic resistance is positive, with $R/\mathscr{R} \leq 1.5$ for the parameters and range of bias currents studied. As for the case of the dynamic inductance, we observe additional structure in $R/\mathscr{R}$ for bias currents below $2I_0$.

We found that the simulated values of $\mathscr{L}$ and $\mathscr{R}$ were nearly independent of the value of C for $\beta_c < 0.3$. The introduction of asymmetry into the critical currents, capacitances, shunt resistances and loop inductance tended to shift the curves as a function of Φ without producing any major changes in the shape or magnitude of the curves shown in Fig. 4.3. The addition of a resistance across the SQUID terminals equivalent
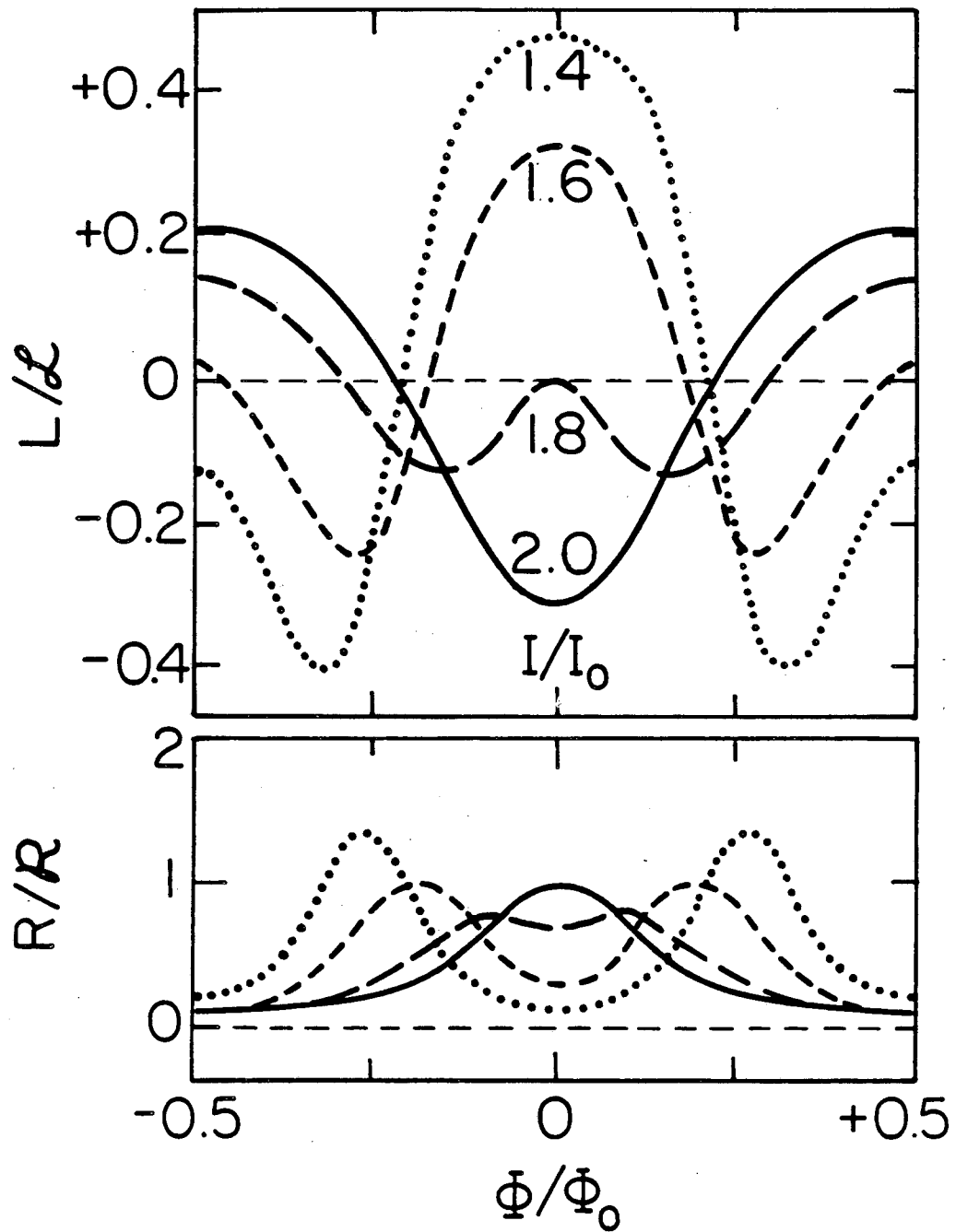
XBL 8411-8267

Fig. 4.3 Dynamic inductance $L/\mathscr{L}$ and dynamic resistance $R/\mathscr{R}$ obtained
from the analog simulator for 4 values of I as a function of
Φ. The SQUID parameters were $\beta = 1.0$, $\beta_c = 0.2$ and $\Gamma = 0.06$.

to a 50-Ω load introduced changes that were smaller than the uncertainty in the data.

4. Effects of Input Circuit on SQUID

The input circuit may modify the characteristics of the SQUID in two ways, first, through the effects of parasitic capacitance that can affect the SQUID even when the input coil is open, and, second, through the loading of the SQUID by the input circuit. The extent to which a comparison between the simulated characteristics of a bare SQUID and the experimental characteristics of a real SQUID is meaningful depends on the importance of the effects of the parasitic capacitance, and it is convenient to discuss them before turning to an investigation of the input impedance.

4.1 Parasitic Capacitance

There is a parasitic capacitance between the input coil and the SQUID that we estimate to be about 12 pF, 5 pF, and 1 pF for the 50-, 20-, and 4-turn SQUID, respectively. (Strictly speaking, there is an additional quarter turn in each case). This capacitance is clearly distributed and, as emphasized by Muhlfelder and Johnson (1984), any theoretical discussion must take this fact into account. Experimentally, the most obvious effect of the capacitance is to introduce structure onto the I-V characteristic of the SQUID (Germain et al., 1984; Muhlfelder and Johnson, 1984). To illustrate this effect, Fig. 4.4 shows the I-V characteristics of 4 SQUIDs, one with no input coil, and the other three with 4-, 20-, and 50-turn input coils; the values of β were nearly identical. The I-V characteristic of the bare SQUID [Fig.
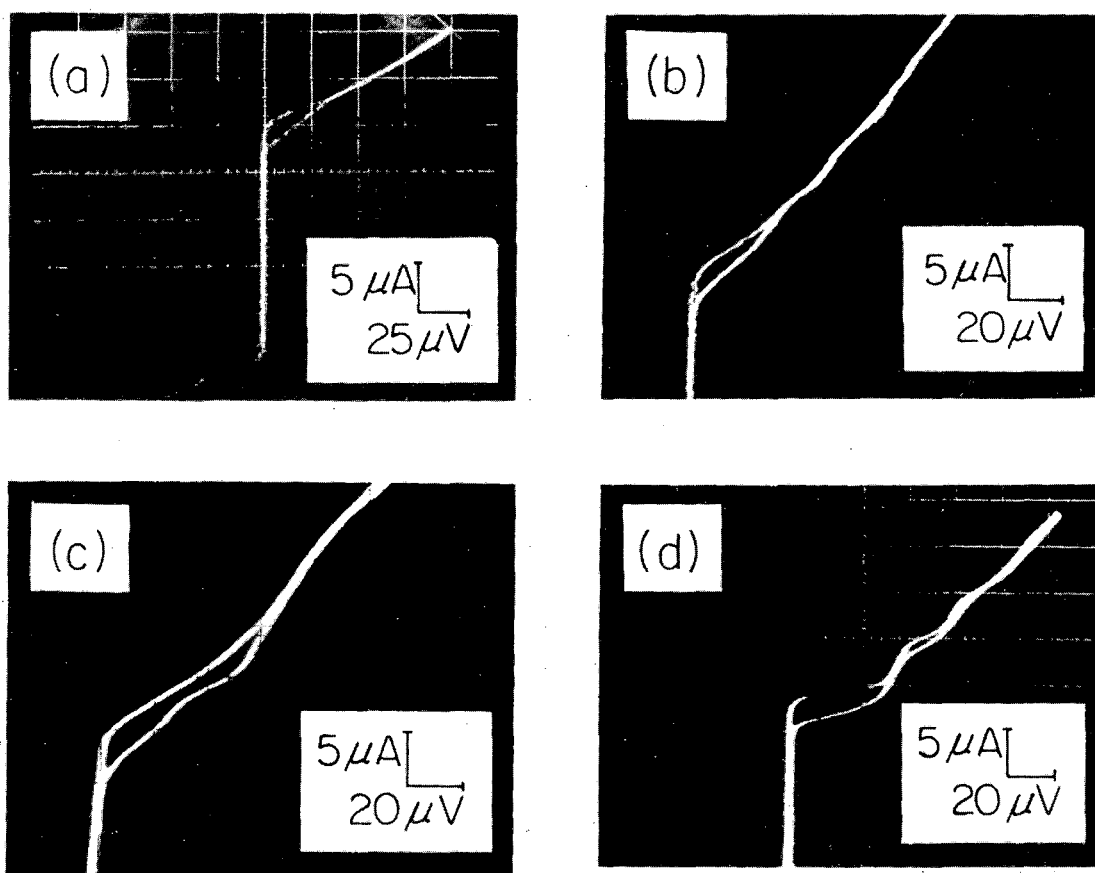
XBB 850-8159A

Fig. 4.4 I-V characteristics of 4 different dc SQUIDs: (a) no input
coil, $\beta \simeq 2.5$; (b) 4-turn input coil, $\beta \simeq 2.6$; (c) 20-turn
input coil, $\beta \simeq 2.8$; (d) 50-turn input coil, $\beta \simeq 2.4$.

4.4(a)] is smooth while the characteristics of the other three SQUIDs

exhibit current steps that grow in amplitude as the number of turns

increases. However, the steps occur at approximately constant voltage

intervals of about 30 μV for all three SQUIDs, irrespective of the

number of turns on the input coil. Thus, we believe that the steps are

associated with resonances of the stripline formed by the coil and the

SQUID, rather than with a LC-resonance involving the lumped inductance

of the input coil and its lumped capacitance to the SQUID (Tesche,

1982b). These stripline resonances are very reminiscent of those

observed by Muhlfelder et al. (1985) with a SQUID overlaying a ground

plane.

4.2 Effects of Inductive Coupling

Germain et al. (1984) studied the effects of an input circuit on the

dynamics of a SQUID by investigating the V-Φ curves with the input coil

open, shorted, or shunted with a capacitor. They found that the curves

depended markedly on the impedance connected across the input coil.

Jaycox (1981) has studied the effects of an open and shorted input coil

on the I-V characteristics of a SQUID. We have performed a related set

of experiments, as indicated in Fig. 4.5. A Pb wire was connected

directly across the pads of the 20-turn input coil of a SQUID. We

verified that the wire made superconducting contacts to the input coil

by applying a small, quasistatic magnetic field. We could break the

wire by pulling on a thread attached to it. In this way, we were able

to measure the characteristics of the same SQUID with a shorted or

opened input coil. Figure 4.6 shows the I-V characteristics at flux

biases of integral and half-integral flux quanta with opened and shorted
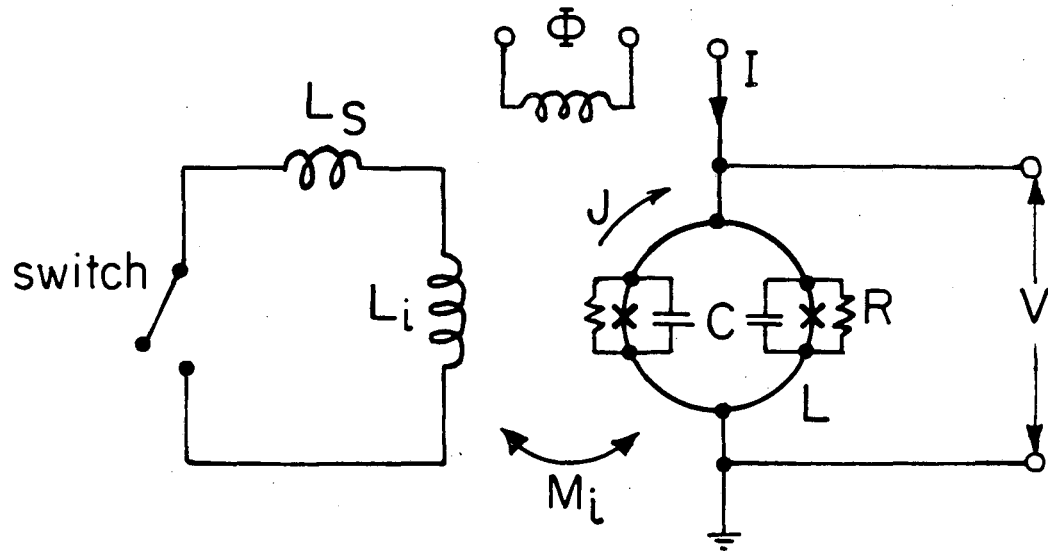
XBL 8411-8268

Fig. 4.5 Experimental configuration used to study the effects of an
open and shorted input coil on the SQUID characteristics.

input coils for a SQUID with $\beta \equiv 2LI_o/\Phi_o \approx 2$, 3 and 4; Table IV.I lists the SQUID parameters for these and two other values of β. For this series of experiments, the critical current of the junctions was progressively lowered by deliberately exposing the SQUID to a humid atmosphere. We note, incidentally, that the current steps in Fig. 4.6 become more pronounced as the critical current increases.

The modulation depth of the critical current, ΔI_c, is listed in Table IV.I. For the open input coil, the values are in good agreement with those predicted (Tesche and Clarke, 1977) for a SQUID with $L = 0.4$ nH. When the input coil is shorted, the modulation depth increases, implying that the effective SQUID inductance has been lowered. The inferred values of β(shorted) and of $\alpha_e^2 = 1 - \beta$(shorted)$/\beta$(open) are also listed in Table IV.I. The average value of α_e^2, 0.64 ± 0.06, is in good agreement with our estimated value of α^2, 0.70, reduced by a factor $1/(1 + L_s/L_i) \approx 0.92$ to 0.65; we estimate L_s to be about 10 nH. These changes in ΔI_c indicate that the SQUID is screened by the input coil at zero frequency just as one would expect. We note, however, that there are observable changes in the current modulation depth at voltages up to about 60 μV, corresponding to a Josephson frequency of about 30 GHz. Thus, it appears that the input circuit at least partially screens the SQUID up to frequencies of this order despite the presence of parasitic capacitance. In this respect, we see already that the lumped circuit model of Fig. 4.1(a) can be a useful approximation to real SQUID amplifiers.

In the same series of experiments, we also measured V_Φ^r(max), the maximum value of V_Φ^r, by injecting a small 1 kHz-flux via the auxiliary bias coil. The relative increase in V_Φ^r(max) for a given value of $2I_o$

Shorted
Input
Coil

$5\mu A$
$20\mu V$
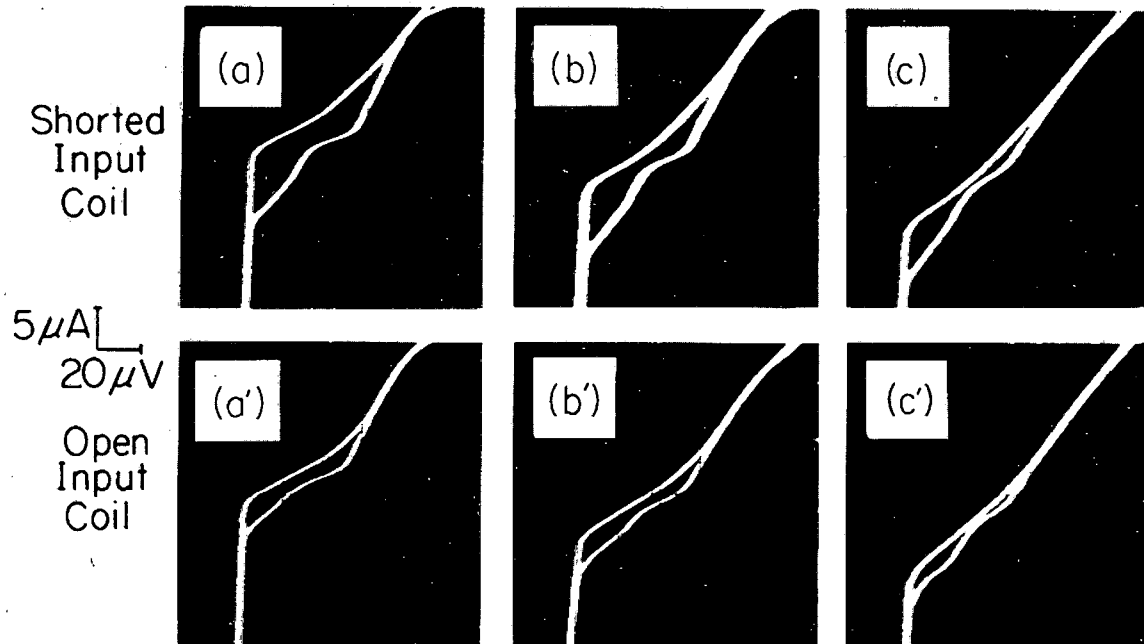
Open
Input
Coil

XBB 840-8245A

Fig. 4.6   I-V characteristics for 20-turn SQUIDs with shorted (a,b,c) and open (a',b',c') input coils: (a,a') $\beta \approx 2$, (b,b') $\beta \approx 3$, and (c,c') $\beta \approx 4$.

Table IV.I. Summary of measured parameters and α_e^2 for five 20-turn SQUIDs with shorted and open input coils.

$2I_o$ (μA)	SHORTED				OPEN				α_e^2 $= 1 - \beta^r/\beta$
	ΔI_c^r (μA)	β^r $= 2L^r I_o/\Phi_o$	I (μA)	V_Φ^r(max) (μV/Φ_o)	ΔI_c (μA)	β $= 2LI_o/\Phi_o$	I (μA)	V_Φ(max) (μV/Φ_o)	
38 ± 1	10 ± 1	2.5 ± 0.5	39	500 ± 30	4.0 ± 0.5	7.5 ± 1.2	39	280 ± 30	0.69 ± 0.08
24 ± 1	8 ± 1	1.7 ± 0.4	22	170 ± 20	4.0 ± 0.5	4.5 ± 1.0	22	120 ± 20	0.62 ± 0.12
			24	260 ± 20			24	160 ± 20	
20 ± 1	7 ± 0.5	1.6 ± 0.3	20.5	190 ± 20	3.5 ± 0.5	4.1 ± 0.9	20.5	110 ± 20	0.61 ± 0.12
			24.0	140 ± 20			24.0	95 ± 20	
16 ± 1	7 ± 0.5	1.1 ± 0.25	16.5	160 ± 20	3.5 ± 0.5	3.0 ± 0.8	16.5	120 ± 20	0.63 ± 0.12
			22.0	130 ± 20			22.0	110 ± 20	
10 ± 1	6 ± 0.5	0.65 ± 0.25	11	90 ± 20	3.0 ± 0.5	2.0 ± 0.6	11	50 ± 20	0.68 ± 0.15

when the input coil was shorted, typically a factor of 1.5, was less than the relative increase in ΔI_c, at least partly because of an associated decrease in the dynamic output resistance of the SQUID, $R_d^r \equiv (\partial V / \partial I)^r$. We conclude that, despite the presence of parasitic capacitances, a short circuited input coil reduces the effective inductance of the SQUID loop at the Josephson frequency at which the transfer function is a maximum by essentially the same factor, $(1 - \alpha_e^2)$, as it does at low frequencies.

Thus, it appears that, to good approximation, one can use the lumped circuit model in designing and analyzing amplifiers based on these SQUIDs. We note, however, at least for the SQUIDs described here, that the difference between V_ϕ and V_ϕ^r is not substantially greater than the uncertainty in V_ϕ due to uncertainties in the SQUID parameters. Furthermore, in many practical amplifiers, the additional stray inductances associated with the components in the input circuit or the presence of a pick-up loop will reduce α_e^2 to a value lower than that for the shorted input, thereby reducing the effects of the input circuit on the SQUID parameters still further. The precise values of the changes depend, of course, on the values of the critical and bias currents. We note that the changes in $V_\phi^r(\max)$ sometimes differed significantly from those listed in Table IV.I in the case of those SQUIDs with the larger values of β when they were operated on a sharp resonant step. This observation is not of great practical importance, however, since we have found that the noise level of our SQUIDs is always relatively high in the vicinity of steps, and we take care to bias our amplifiers away from these regions.

In closing this section, we note that the effects of opening and

closing the input circuit for a SQUID with a higher value of α^2, say 0.9 (Ketchen and Jaycox, 1982; Tesche et al., 1985; Germain et al., 1984), would be even more serious. For example, if the stray inductance were negligible, a shorted input coil would lower the bare SQUID inductance by an order of magnitude.
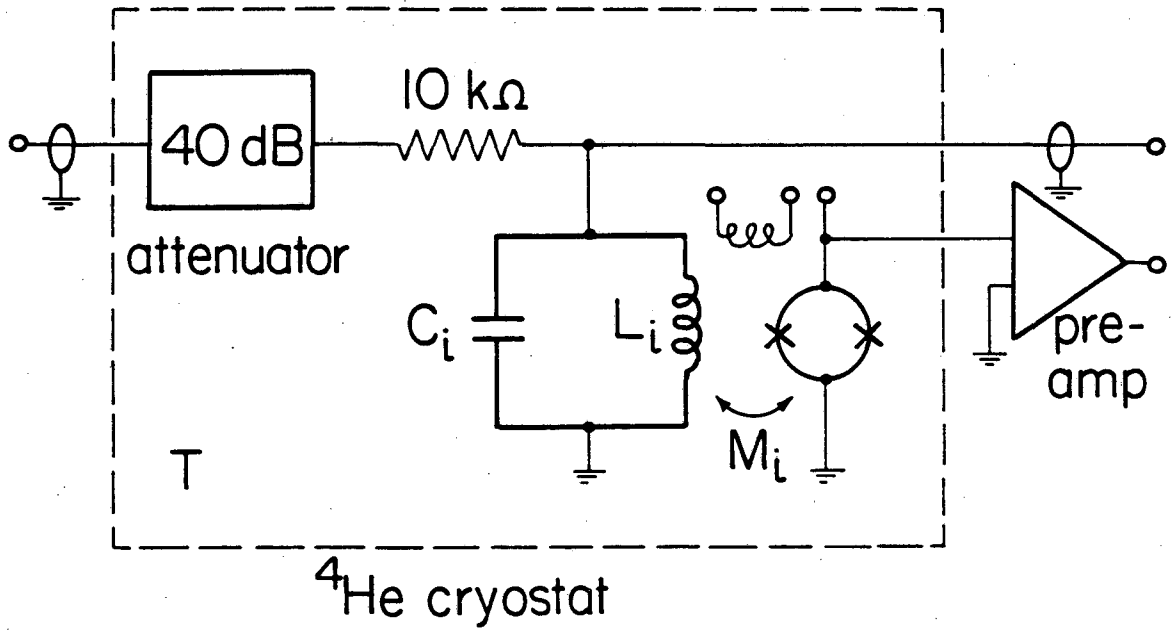
5. Dynamic Input Impedance of a dc SQUID

We now describe the experimental determination of the dynamic input impedance, and compare the data with the results of our simulations.

5.1 Experimental Measurements

To determine Z_T^* we measured the resonant frequency f_o and quality factor Q of a SQUID amplifier with a tuned input circuit as shown in Fig. 4.7. We used a 20-turn SQUID ($L_i \approx 120$ nH) with a capacitor $C_i \approx$ 18 nF connected directly across the input coil; thus the only losses in the input circuit itself arose from the capacitor and its leads. We note that this input circuit was far from optimal as far as the noise temperature was concerned, being designed to maximize the effects of the reflected SQUID impedance. The power gain was about 50 dB (McDonald, 1984). The Nyquist noise voltage in the input circuit was amplified by the SQUID, and we measured the spectral density of the noise at the output with a spectrum analyzer to determine the resonant frequency, f_o, and the full width at half-maximum (FWHM), Δf, as functions of I and ϕ.

To interpret our results, it was necessary to measure the resonant frequency f_o^o and bandwidth Δf^o of the unloaded input circuit. We biased the SQUID with a large current ($I \gg 2I_o$) so that the dynamic input impedance of the SQUID was very nearly 2R. In this condition (as

Fig. 4.7 Experimental configuration for the measurement of the dynamic input impedance of a dc SQUID amplifier.

verified on the simulator) the inductive screening of the input coil by the SQUID was negligible, while the resistance reflected into the input circuit, $\omega^2 M_i^2/2R$ could easily be computed and corrected for: it was typically less than 1 mΩ, an order of magnitude smaller than the intrinsic value of R_i. We connected the high-impedance input of the HP 3585 spectrum analyzer directly across the input circuit and measured its response to a signal injected via a cold 50 Ω, 40 dB attenuator in series with a cold 10 kΩ resistor (Fig. 4.7). The attenuator and resistor eliminated the 300K noise while imposing a relatively small loading on the tuned circuit. In addition, the current injected into the tuned circuit was thus very nearly constant, independent of frequency. For the series of measurements presented in this paper, we found $f_o^o = 2.94 \pm 0.01$ MHz and $\Delta f^o = 14.5 \pm 1$ kHz (after correction for the capacitive and resistive loading of the spectrum analyzer). We deduce $L_i + L_s \approx 160$ nH, yielding $\alpha_e^2 \approx 0.53$, and $R_i \approx 15$ mΩ.

In Fig. 4.8 we show f_o, Δf and $P(f_o)$, the output noise power at f_o, vs. Φ for three values of bias current in the vicinity of the normal operating bias, and at two temperatures. From the noise-rounded I-V characteristics, we estimated the maximum critical current of the SQUID to be 6 ± 1 μA at 4.2K and 7 ± 1 μA at 1.5K. The Q factor was typically 200. The minima in $P(f_o)$ were used to determine the value of Φ. The uncertainty in the results is smaller than the size of the data points. We see that both f_o and Δf are substantially affected by the presence of the SQUID, the effects tending to increase in magnitude as the bias current is lowered. The resonant frequency changes by up to $\pm$ 20%, while the bandwidth can be increased by a factor of up to 4 or reduced by a factor of up to 2. At the lowest bias current at each temperature,
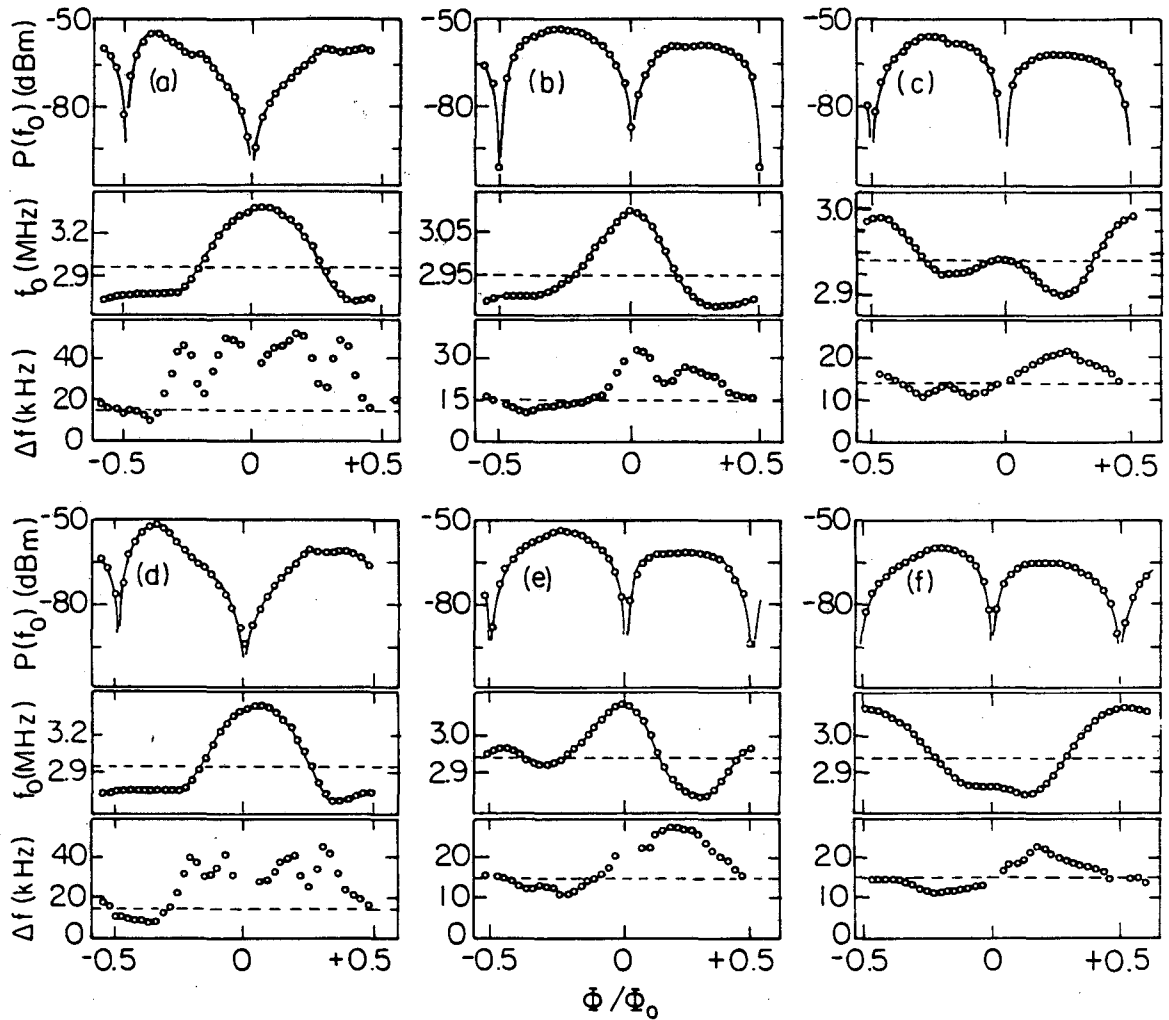
XBL8411-8269

Fig. 4.8 Noise power at resonance, $P(f_o)$, measured at SQUID output, re-
sonant frequency, f_o, and width of resonance, Δf, as functions
of ϕ/ϕ_o for 20-turn SQUID, at two different temperatures:
(a)-(c) T = 4.2K, (d)-(f) T = 1.5K. The bias current I was
constant for each set of data: (a) I = 4.0 μA, (b) I = 5.0 μA,
(c) I = 6.0 μA, (d) I = 5.0 μA, (e) I = 6.0 μA, (f) I = 7.0 μA.
The resonant frequency f_o^o and bandwidth Δf^o of the unloaded
circuit are shown as dashed lines.

there is more structure in Δf than at the higher bias currents. The output power at resonance is a maximum at bias currents near $1.6I_o$, where V_ϕ is a maximum. The value of $P(f_o)$ at the $\pm \phi_o/4$ bias points is asymmetric by as much as 10 dB for this particular SQUID. This asymmetry cannot be explained by a corresponding asymmetry in V_ϕ, which, in a separate experiment, was determined to be symmetric to within 20%. There is also some weak structure in $P(f_o)$ that appears to be related to structure in Δf.

The similarity between the data at 4.2K ($\Gamma \equiv 2\pi k_B T/I_o \phi_o \approx 0.06$) and 1.5K ($\Gamma = 0.02$) suggests that in this range temperature has little effect on the results, other than by changing the critical current: the sets of curves obtained at the two temperatures at approximately the same values of $I/2I_o$ are quite similar.

We have obtained similar results on 3 other SQUIDs with comparable critical currents in which the maximum values of $|f_o^o - f_o|$ and $|\Delta f - \Delta f^o|$ varied by up to a factor of 2. We have also measured a Q-value of up to 10^4 at 4.2K and up to 3×10^4 at 1.5K in SQUIDs with higher critical currents; in one case the circuit became unstable and oscillated at a frequency f_o^o for bias currents below $1.4I_o$.

5.2 Analysis and Interpretation of Results

The results presented above arise from a resonance in the gain of the amplifier, that is, from Eq. (4.1), in $1/Z_T^*$. It is straightforward to derive $\mathscr{L}^r$ and $\mathscr{R}^r$ from the experimental data. From Eq. (4.3) we obtain

$$\Delta L_i \equiv \alpha_e^2 L \left(\frac{R_i}{\mathscr{R}^r} - \frac{1}{\omega^2 C_i \mathscr{L}^r} \right) = \frac{1}{(2\pi)^2 C_i} \left[\frac{1}{f_o^2} - \frac{1}{(f_o^o)^2} \right], \qquad (4.4)$$

and

$$\Delta R_i \equiv \alpha_e^2 L\left(\frac{R_i}{\mathscr{L}^r} + \frac{1}{\mathscr{R}^r C_i}\right) \approx \frac{1}{2\pi C_i}\left[(1 + \alpha_e^2 \frac{L}{\mathscr{L}^r})\frac{\Delta f}{f_O^2} - \frac{\Delta f^O}{(f_O^O)^2}\right]. \quad (4.5)$$

In deriving Eq. (4.5), we have assumed that ΔR_i is evaluated at $\omega = \omega_O$, thereby ignoring its frequency dependence. This frequency dependence actually introduces a slightly non-Lorentzian line-shape into the resonance, which we observed for the low Q values (< 30) obtained at the lower bias currents. However, to first order the resistance at resonance, $\Delta R_i(f_O)$, is still given by the FWHM of the peak.

We derived V_ϕ^r from our data by noting that the Nyquist noise voltage in the input circuit has a spectral density $4k_B T R_i$ and that the voltage gain at resonance is $M_i V_\phi^r / (R_i + \Delta R_i)$. We find

$$\left|V_\phi^r(\omega_O)\right| = \frac{R_i + \Delta R_i}{M_i}\left[\frac{P(f_O)R_D^r}{k_B T R_i \eta B}\right]^{1/2}, \quad (4.6)$$

where B is the measured noise bandwidth of the spectrum analyzer, typically 2.6 kHz, and η is the power mismatch factor between the dynamic resistance of the SQUID, R_D^r, and the 50-Ω input impedance of the spectrum analyzer. For $R_D^r = 10\ \Omega$, $\eta = 5/9$.

The apparent values of $L/\mathscr{L}$, $R/\mathscr{R}$ and $\left|V_\phi\right|$ obtained from the data in Fig. 4.8 using Eqs. (4.4)-(4.6) are shown in Fig. 4.9. We note that, although the precision of the data shown in Fig. 4.8 is very good, the uncertainties in the parameters of the unloaded circuit, f_O^O and Δf^O, due to the corrections mentioned above, and in the value of R_D, could introduce a systematic error in the mean values of $L/\mathscr{L}$ ($\pm$ 0.02) and $R/\mathscr{R}$ ($\pm$ 1) and in the scaling of V_ϕ ($\pm$ 20%). In Fig. 4.10(a)-(d) we show simulated curves for a SQUID with $\beta = 1$, $\beta_c = 0.2$ and $\Gamma = 0.06$,
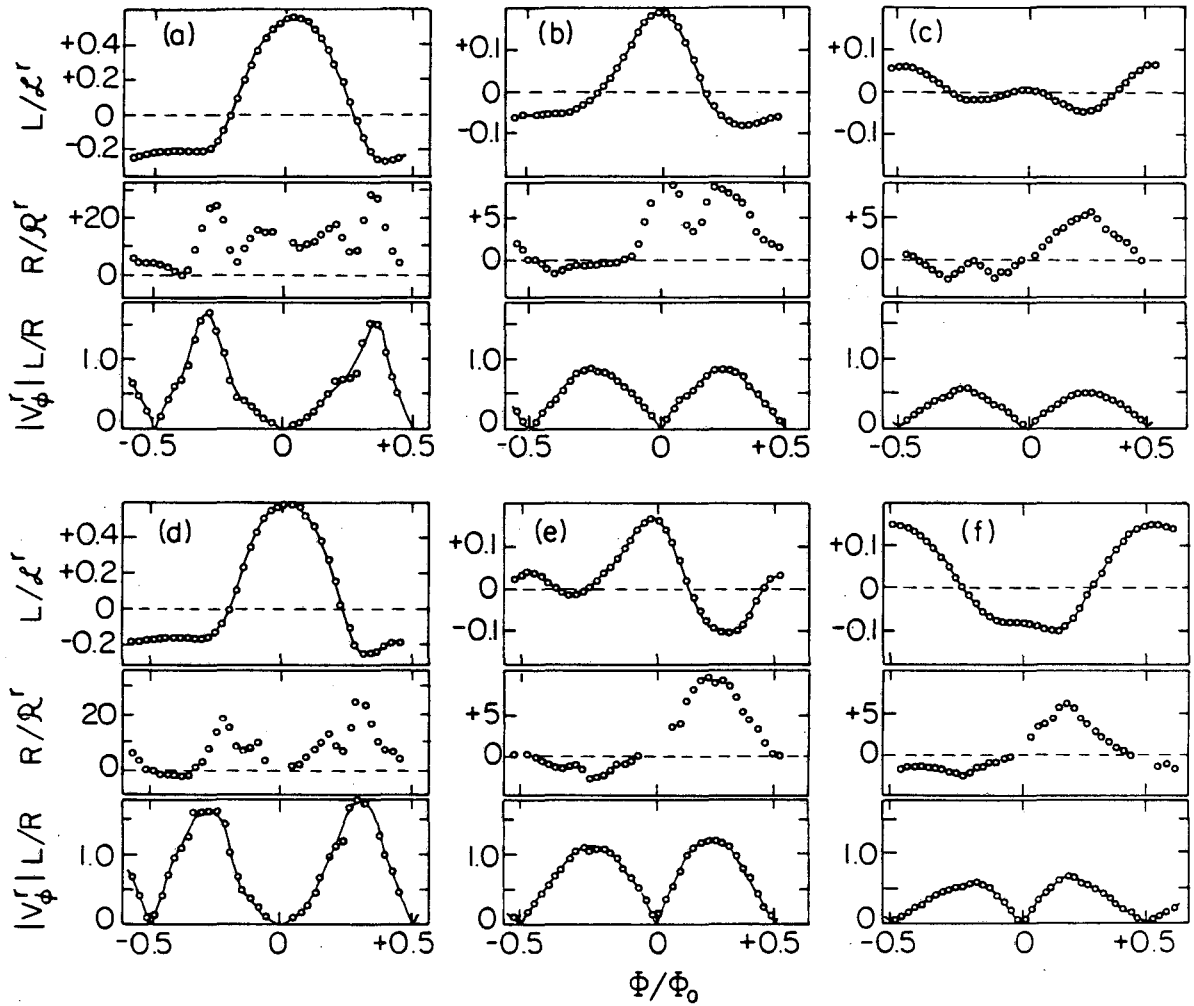
Fig. 4.9 Dynamic inductance, $L \mathcal{L}^r$, dynamic resistance $R \mathcal{R}^r$, and flux-to-voltage transfer function, $|V_\phi^r|$, vs. ϕ/ϕ_0 obtained from Fig. 4.10. Note the scales for $L \mathcal{L}^r$ and $R \mathcal{R}^r$ in (a) and (d) differ from those for the remaining figures.
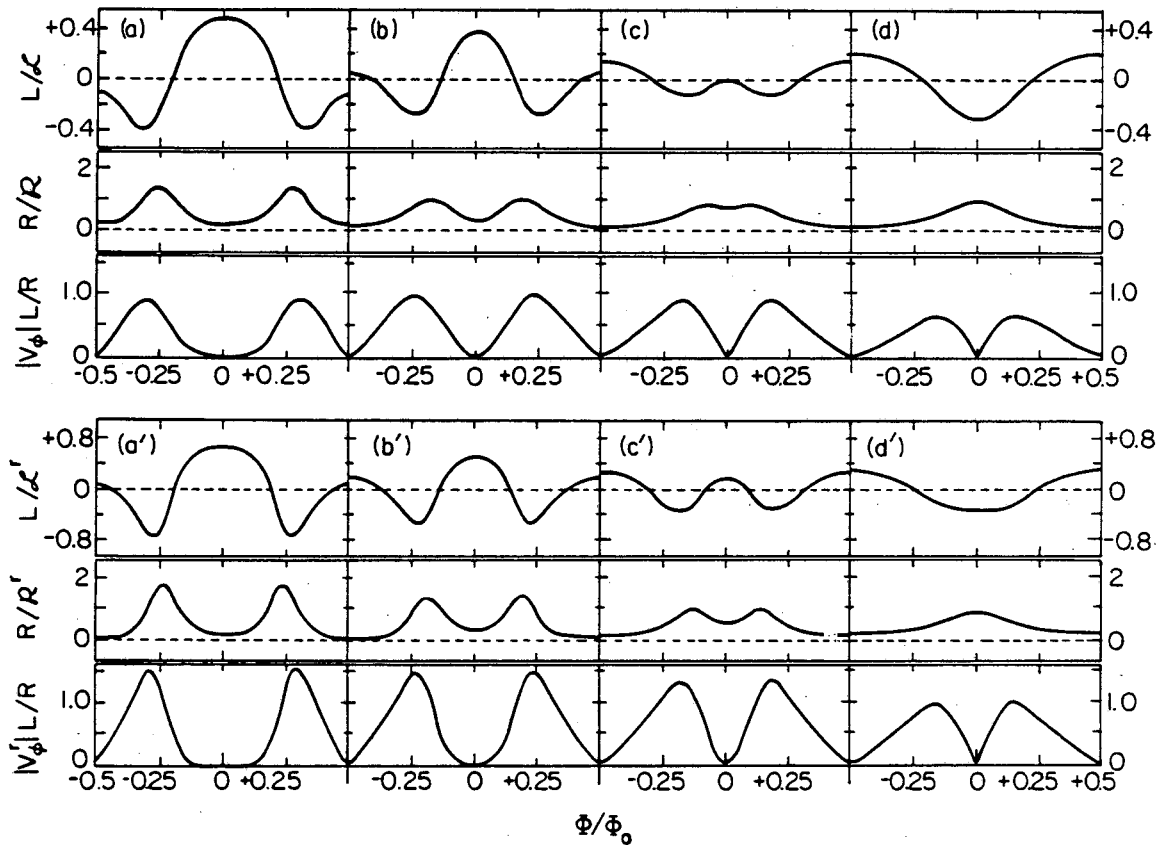
XBL8411-8271

Fig. 4.10 Dynamic inductance, dynamic resistance and flux-to-voltage
transfer function vs. Φ/Φ_0, obtained from analog simulator for
a bare SQUID with $\beta = 1$, $\beta_c = 0.2$ and $\Gamma = 0.06$ (a)-(d), and
for a reduced SQUID with $\beta^r = 0.47$, $\beta_c = 0.2$ and $\Gamma = 0.06$
(a')-(d'). The bias current was varied from $1.4I_0$ to $2.0I_0$ in
$0.2I_0$ steps from left to right for each SQUID.

corresponding to the <u>bare</u> SQUID in our experiments, while in Fig. 4.10 (a')-(d') we show simulated curves for the <u>reduced</u> SQUID with β^r = 0.47 corresponding to $\alpha_e^2 \approx 0.53$. As in Sec. 2, the precision is about 10%. We note that the trends indicated in the simulated values of $L/\mathscr{L}$, $R/\mathscr{R}$ and V_ϕ as the bias current is increased are rather similar for both values of β.

It is convenient first to discuss the behavior of V_ϕ. The curves are relatively symmetric about ϕ = 0. For each temperature, at the higher bias currents the shape and magnitude of V_ϕ are remarkably close to the simulations for β = 1, while at the lowest bias current, V_ϕ resembles the simulations for β^r = 0.47 more closely. A possible explanation for this trend is that the screening of the SQUID inductance is reduced at the higher currents (frequencies) over that at the lower currents because of the effects of parasitic capacitance. These observations are consistent with those made in Sec. 4.2: at relatively low bias currents, where V_ϕ is a maximum, the use of the reduced parameters is a reasonable approximation.

Turning now to the measured values of $L/\mathscr{L}$, we see that the overall trends as the bias current is increased follow the trends in the simulations quite well. Thus, at the lowest bias current, $L/\mathscr{L}$ shows a broad maximum at ϕ = 0 and a negative region around ϕ = $\pm$ $\phi_0/2$. As I is increased, the structure evolves until, in Fig. 4.9(f) for example, $L/\mathscr{L}$ has a minimum near ϕ = 0 and a maximum near ϕ = $\pm$ $\phi_0/2$. These features are clearly reproduced in the simulations, although there is some asymmetry in the experimental curves, arising, presumably, from asymmetries in the SQUID that are not present in the simulations. The overall magnitude of $L/\mathscr{L}$ is generally in fair agreement with the

simulated values; in particular, $L/\mathscr{L}$ is always small near $\Phi = \pm \Phi_0/4$.
As we found for V_Φ, there seems to be good agreement between $L/\mathscr{L}$ and the
simulations with $\beta^r = 0.47$ at the lower bias currents, whereas for the
higher bias currents there is somewhat better agreement with the
simulations for the bare inductance. We note, also, that the condition
$\int_0^{\Phi_0} d\Phi/\mathscr{L} = 0$ is satisfied to within the experimental uncertainties.
Thus, although none of the measured curves is represented precisely by
any one of the simulated curves, nonetheless we feel that the general
behavior of V_Φ and $\mathscr{L}$ is reasonably well described by our model. Both
sets of curves indicate that the screening of the SQUID inductance by
the input circuit is reduced at the higher Josephson frequencies,
presumably because of the presence of the parasitic capacitance.

Finally, we turn to the apparent values of $\mathscr{R}$ inferred from our
data. It is immediately obvious that, in contrast to $\mathscr{L}$ and V_Φ, the ex-
perimental values of $R/\mathscr{R}$, which vary between about $+30$ and -5 are in
sharp disagreement with the simulated values, which are positive with a
maximum value of about 2. The simulated curves have a symmetry about Φ
$= 0$ that is obviously lacking in the experimental curves. Thus, we are
forced to conclude that our model is incomplete, and that ΔR_i is domina-
ted by a mechanism other than the resistance reflected from the SQUID.

5.3 Feedback Model for ΔR_i

A clue to the origin of the qualitative and quantitative discrepanc-
ies between the measured and simulated values of $\mathscr{R}$ is provided by the
fact that, at least at the two higher bias currents, Δf and ΔR_i scale
roughly with V_Φ (see Fig. 4.8). This observation suggests that feedback
from the output of the SQUID to the input circuit via the distributed

capacitance between the SQUID and the input circuit may make the dominant contribution to ΔR_i. To simplify the model, we replace this distributed capacitance with a single capacitor, C_p, as indicated in Fig. 4.11(a). In the limits $1/\omega C_p \gg R_d$, where the capacitive feedback does not load down the output of the SQUID, and $\omega^2 L_i C_p \ll 1$, it is straightforward to show that the voltage gain of the amplifier is given by

$$G_V^!(\omega) = \frac{M_i V_\phi^r / Z_T^*}{1 - j\omega M_i C_p V_\phi^r (1 - j\omega L_i / Z_T^*)} . \tag{4.7}$$

(We have assumed that the bias current is in the range where V_ϕ^r is a better approximation than V_ϕ.) In general, the capacitive coupling produces a change in Z_T^* given by

$$\Delta Z_T^*(\omega) = - j\omega M_i C_p V_\phi^r [Z_T^*(\omega) - j\omega L_i]. \tag{4.8}$$

In general V_ϕ^r is a complex number (McDonald, 1984). However, analog simulations show that the phase shift in V_ϕ^r is less than 5° for $f < f_J/10$. Therefore we assume V_ϕ^r to be real in this simplified feedback model. At the resonant frequency of the amplifier and for high values of Q ($\omega L_i \gg R_i$), Eq. (4.7) produces a change in the input resistance only:

$$\Delta R_i(\omega_0) = - \omega_0^2 M_i L_i C_p V_\phi^r = - M_i V_\phi^r C_p / C_i. \tag{4.9}$$

The last two expressions are obviously equivalent for the circuit shown in Fig. 11(a). However, the situation changes when a substantial stray inductance, L_s, is introduced into the input circuit. Depending on whe-

(a)   (b)   (c)

R_i C_i C_P R_i C_i C_P R_i C_i C_P

V_i L_S V_i

L_i V_i L_i

          L_i L_S
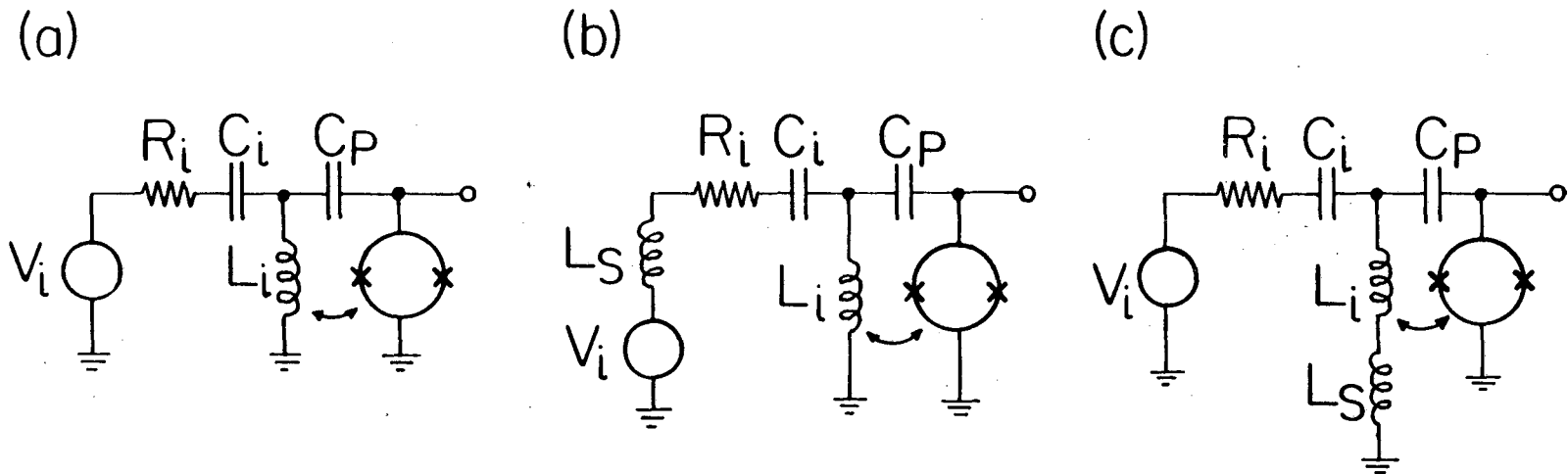
Fig. 4.11 Simplified model of capacitive feedback: (a) without stray inductance, (b) and (c) with stray inductance, L_s.

ther Fig. 11(b) or 11(c) is the more appropriate, the former or latter result in Eq. (4.9) applies. The distinction is of considerable importance for an amplifier with a small input coil (see later in this section). We note that, within our approximations and at the resonant frequency, feedback does not contribute to ΔL_i. We have also considered inductive feedback between the output current of the SQUID and the input circuit, but found these effects to be negligible. Typically, $|\Delta L_i| <$ 0.1 nH and $|\Delta R_i| < 0.1$ mΩ for a SQUID connected to a preamplifier with an input impedance of 50 Ω or higher.

We first estimate the maximum size of ΔR_i predicted by Eq. (4.9). If we take the measured values $L_i \approx 120$ nH, $M_i \approx 6$ nH, $f \approx 2.9$ MHz and $|V_\phi^r(\max)| \approx 20 \ \mu V \Phi_0^{-1}$, together with the value of $C_p \approx 5$ pF based on the self-resonance of the input coil at about 200 MHz, we find $|\Delta R_i(\max)| \approx$ 12 mΩ, a value about a factor of 2 greater than the observed value. Given the considerable simplification of replacing the distributed capacitance with a lumped capacitor, we feel that this factor of 2 discrepancy is acceptable.

We turn now to a discussion of the scaling predictions of Eq. (4.9). First, in all cases, ΔR_i is zero at or near the values of Φ where V_ϕ^r is zero. However, at the lowest bias currents [Figs. 4.9(a) and (d)], the extrema in ΔR_i are of the same polarity, rather than of opposite polarity as predicted by the model. This discrepancy may be due to the effects of resonances on the I-V characteristics. At the higher bias currents [Figs. 4.8(b), (c), (e) and (f)], ΔR_i has extrema of opposite polarity near the extrema of V_ϕ, as predicted by the model; however, the observed symmetry in ΔR_i is substantially greater than that in V_ϕ. Part of this asymmetry may arise from a small, bias-dependent shift

introduced into the curves by the inductive coupling of the dynamic SQUID impedance [Eq. (4.5)]. We believe, however, that this discrepancy arises mainly because the magnitude of the effective flux noise induced into the SQUID by the input circuit depends on ΔR_i, so that one averages over a different range of flux for positive and negative values of ΔR_i. To understand this effect, we note that the spectral density of the effective flux noise induced into the SQUID by the input circuit is $4k_B T R_i M_i^2/(R_i + \Delta R_i)^2$. The noise bandwidth is $(R_i + \Delta R_i)/4(L_i + L_s)$, where we have neglected the effect of ΔL_i, which is close to zero when ΔR_i has an extremum. Thus, the rms flux noise in the SQUID is

$$\phi_N^* = M_i \left[\frac{k_B T R_i}{(L_i + L_s)(R_i + \Delta R_i)} \right]^{1/2}, \qquad (4.10)$$

or about $\phi_o/30(1 + \Delta R_i/R_i)^{1/2}$ for our measurements at 1.5K. When $\Delta R_i = 0$, the peak-to-peak flux-noise amplitude is roughly $\phi_o/6$. Depending on whether ΔR_i is positive or negative, the peak-to-peak flux noise is reduced or increased. Consequently, when the average value of ΔR_i is negative, the flux noise averages J_ϕ over a wider range of flux than when ΔR_i is positive, thereby possibly including regions where ΔR_i is positive. As a result, the apparent negative resistance can be substantially smaller in magnitude than the apparent positive resistance. All of the 20-turn SQUIDs with β between 1 and 3 that we investigated at various bias currents showed similar asymmetric effects. We note that the averaging of the SQUID parameters over a variable range of flux, as well as the dependence of α_e^2 on the Josephson frequency the hence the bias point, imply that the requirement $\int_o^{\phi_o} d\phi/\mathscr{R} = 0$ is only approximately true.

A further potential complication arises from the voltage noise

induced into the input circuit by the circulating noise current in the SQUID, which we have neglected in our analysis. As shown in Chapter II for a lumped circuit model [see Eq. (2.19)], this contribution is equivalent to a voltage noise source with a spectral density $S(f) = (\alpha_e^2 L/M_i)^2(R_i^2 + 1/\omega^2 C_i^2)S_J^r(f)$ in the input circuit, where $S_J^r(f) = 2\gamma_J^r k_B T/R$ and the parameter γ_J^r can be computed by solving the SQUID circuit equations (Tesche and Clarke, 1977) for a bare SQUID with a reduced inductance $L(1 - \alpha_e^2)$. As this noise source is uncorrelated with the Nyquist noise of the input resistor R_i, its spectral density simply adds to that of the Nyquist noise, $4k_B T R_i$. Analog simulations show that the value of γ_J is relatively insensitive to the value of the reduced inductance for a given critical current and temperature. For a bare SQUID with $\beta \cong 0.5$ biased at $1.6I_0$ we obtained a maximum value of 8 ± 2 for γ_J at $\phi_0 \cong \phi_0/4$. For the data presented in Figs. 4.8 and 4.9 at about 3 MHz, we estimate $S(f)/4k_B T R_i \approx \gamma_J^r/35 \approx 1/4$ when the SQUID is biased near $\pm \phi_0/4$ and $1.6I_0$. At higher bias currents, say $2I_0$, the maximum ratio is about 1/10, and the effect is relatively unimportant. The effect of the SQUID noise on our estimate of ΔR_i arises because $S_V(f)$ scales as f^2, and will therefore add a non-Lorentzian component to the resonant peak. For the high-Q circuits described here, the effect on the bandwidth is not important. We note however, that the presence of non-negligible SQUID noise will cause us to overestimate our values of V_ϕ slightly. Since V_ϕ depends on the rms value of the noise, the maximum error will be about 10% at $1.6I_0$; at higher biases the error will be much smaller.

Returning to our feedback model, we observe that since M_i and C_p should scale as the number of turns on the input coil, n, while L_i

should scale as n^2, Eq. (4.9) predicts that ΔR_i should scale as $\omega^2 n^4$ or n^2/C_i, depending on the position of any stray inductance in the input circuit. To investigate this scaling, we tested a SQUID with a 4-turn input coil ($L_i \approx 5.6$ nH, $M_i \approx 1.2$ nH, $\alpha^2 \approx 0.65$) at two different frequencies. The results at 4.2K for a bias current of approximately $2I_0$ are shown in Fig. 4.12, and the relevant parameters are summarized in Table IV.II. We note the relatively low values of α_e^2, which imply that the effect of the input circuit on the SQUID should be almost negligible.

The behavior of the 4-turn SQUID is qualitatively similar to that of the 20-turn SQUID shown in Figs. 4.8 and 4.9. However, because of the reduced value of α_e^2, the fractional change in resonant frequency, $\Delta f_0/f_0$, is much smaller than for the 20-turn SQUID; since $\Delta L_i/(L_i + L_p + L_s)$ is nearly independent of frequency, $\Delta f_0/f_0$ has approximately the same value in Figs. 4.12(a) and (b). Since f_0 is constant to within a few percent, we can estimate ΔR_i from

$$\frac{\Delta R_i}{R_i} \approx \frac{\Delta f - \Delta f^0}{\Delta f^0} . \qquad (4.13)$$

Neglecting the difference in V_Φ, we find that the ratio of the values of ΔR_i(max) at the higher and lower frequencies, approximately 8, is in quite good agreement with the ratio of f_0^2 or $1/C_i$, about 9. This result does not enable us to distinguish between the models shown in Figs. 4.11(b) and (c). We can investigate the scaling with n by considering the ratio of ΔR_i for the 4-turn SQUID at 26.25 MHz to ΔR_i for the 20-turn SQUID at 2.94 MHz, approximately 3. Neglecting the small differences in V_Φ in Figs. 4.9(f) and 4.12(c), we find that the model of Fig. 4.11(c), which leads to a scaling with n^2/C_i, predicts a
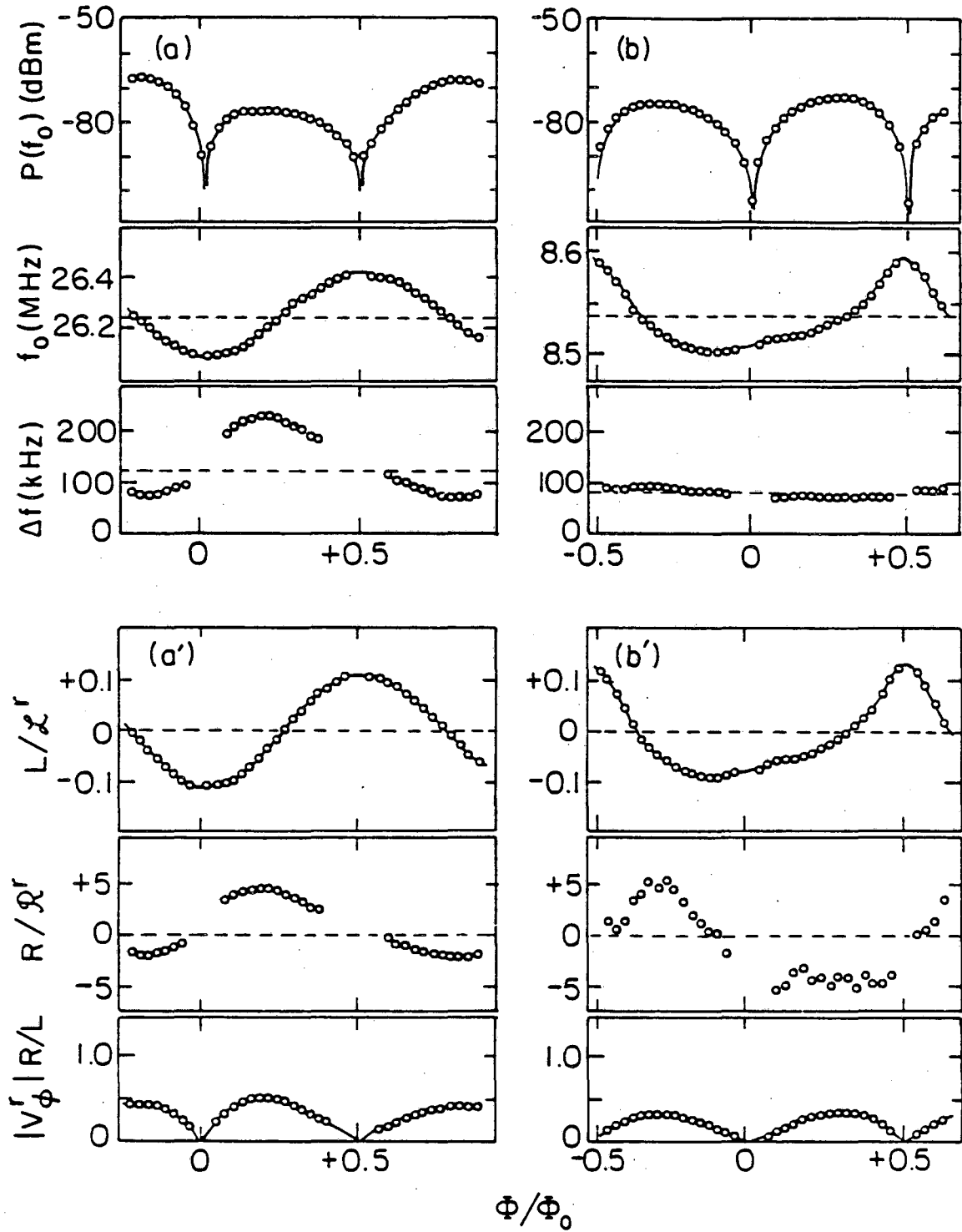
Fig. 4.12 Experimental results and derived SQUID parameters for a 4-turn
SQUID at two different frequencies. In Figs. (a) and (a') the
bias current was 8.0 μA, and the estimated critical current
was 7±1 μA. In Figs. (b) and (b') the bias current was 6.6 μA,
and the estimated critical current was 6 ± 1 μA. The tempera-
ture was 4.2K in both cases.

Table IV.II.   Summary of measured parameters for 4-turn SQUID at two frequencies.

C_i(nf)	f_o^o(MHz)	Δf(max)(kHz)	$L_i + L_p + L_s$(nH)	α_e^2	R_i(mΩ)	$|V_\phi^r$(max)$|$L/R	ΔR_i(mΩ)
1.1	26.25 ± 0.1	120	33	0.10	24	0.5	20
9.2	8.54 ± 0.05	84	38	0.09	19	0.4	2.5

ratio of 0.75, while the model of Fig. 4.11(b), which leads to a scaling with $\omega_o^2 n^4$, predicts a ratio of about 0.15. Thus, for the particular scheme that we used, it appears that the model of Fig. 4.11(c) gives a better description of our results. The remaining discrepancy, about a factor of 4, is by no means negligible, but probably arises in part from our oversimplified model and in part from variations in the magnitude of the effect from device to device.

As a final comment on Fig. 4.12(c) and (d), we note that ΔR_i is more nearly antisymmetric about $\Phi = 0$ than is the case in Fig. 4.9. This may be due to the smaller value of α_e^2 that implies a smaller rms flux noise in the SQUID and, consequently, an averaging of J_Φ^r over a smaller range. Furthermore, for this 4-turn SQUID with a smaller parasitic capacitance than the 20-turn SQUID, ΔR_i scales with V_Φ^r even at the lower bias currents where V_Φ^r is a maximum. This confirms our suspicion that the anomalous behavior of ΔR_i for a 20-turn SQUID at the lowest bias current is due to self-resonances on the I-V characteristic generated by parasitic capacitance.

Considering the simplicity of our feedback model, we believe that its predictions are not unreasonable. The model overestimates ΔR_i for the 20-turn case by a factor of 2 and underestimates ΔR_i for the 4-turn case by a similar factor. For large parasitic capacitances, the model fails to explain the behavior near resonant steps.

6. Concluding Summary

We have investigated the effects of an open and shorted input coil on the critical current modulation and maximum flux-to-voltage transfer coefficient of a planar dc SQUID. From the change in the critical cur-

rent modulation, which is measured at zero Josephson frequency, we conclude that the shorted coil, as expected, screens the inductance of the SQUID to a reduced value $L^r = (1 - \alpha_e^2)L$, where, for our devices, $\alpha_e^2 = 0.64 \pm 0.06$. When the coil was shorted, there was an increase in V_ϕ(max) by a factor of typically 1.5, indicating that, despite the presence of parasitic capacitance, the SQUID is still effectively screened at the Josephson frequency when it is operated at maximum gain.

The most obvious effect of the parasitic capacitance is to induce current steps on the I-V characteristics at voltages corresponding to the resonant frequency of the stripline formed by the input coil and the SQUID. The voltages at which these steps appeared were very similar for SQUIDs with 50-, 20-, or 4-turn input coils, although the amplitude of the steps decreased as the number of turns was reduced. These steps are quite prominent, but we can minimize their effect in a practical amplifier by operating at bias points well aways from them.

The major part of this chapter has been concerned with measurements of the dynamic input impedance and flux-to-voltage transfer function as functions of the bias current and flux. We used the lumped circuit model (which neglects parasitic capacitance) to derive the values of these parameters from the resonant behavior of the tuned amplifier. The values obtained for the SQUID dynamic inductance and transfer function at lower bias currents, where one normally operates a SQUID, agree remarkably well with the predictions of our simulator using L^r, thereby confirming the results of our measurements of V_ϕ(max) for an open and shorted input coil. At higher bias currents, however, the measured values of V_ϕ and $\mathscr{L}$ tend to agree more nearly with the predictions for the unscreened SQUID, indicating that the effective coupling between the

SQUID and the input circuit decreases as the Josephson frequency increases, presumably as a result of the parasitic capacitance.

On the other hand, the lumped circuit model that involves only inductive coupling between the SQUID and the input circuit is unable to account for the observed change in the input resistance of the amplifier. This resistance is dominated by feedback from the SQUID to the input circuit via the parasitic capacitance. A simple model that replaces the distributed capacitance with a lumped capacitor accounts reasonably well for the observed effects, except near resonant steps on the I-V characteristic. The model accounts for the observed resistance to within a factor of 2; this factor is comparable with variations from SQUID to SQUID. We emphasize that this feedback mechanism is dominant only for substantial values of self-capacitance: if the SQUID and input coil were to be separated by a substantially greater distance, presumably lowering both α^2 and C_p, capacitive feedback might well be negligible so that the lumped circuit model could account for the input resistance.

In concluding, we emphasize again the considerable importance of parasitic capacitance on the behavior of this type of SQUID amplifier: in inducing steps on the I-V characteristics, in reducing the inductive screening of the SQUID loop at higher Josephson frequencies, and in producing capacitive feedback that dominates the input resistance. Although we cannot claim to be able to fit our measured curves of $1/\mathscr{L}$, V_ϕ and ΔR_i to our model to better than a factor of 2, this accuracy, together with our understanding of the scaling of ΔL_i and ΔR_i with the relevant parameters, is sufficient to enable us to design the input circuit of an amplifier so as to minimize the effects of ΔL_i and ΔR_i.

In particular, we feel justified in using the lumped circuit model, with the addition of capacitive feedback, to compute the parameters for amplifiers using the type of SQUID described in this thesis, at least at the values of bias current where V_ϕ is at or near its maximum value. In the following chapters, we apply these results to the design of rf amplifiers based on dc SQUIDs, and compare the measured gain and noise temperature with the predictions of the model.
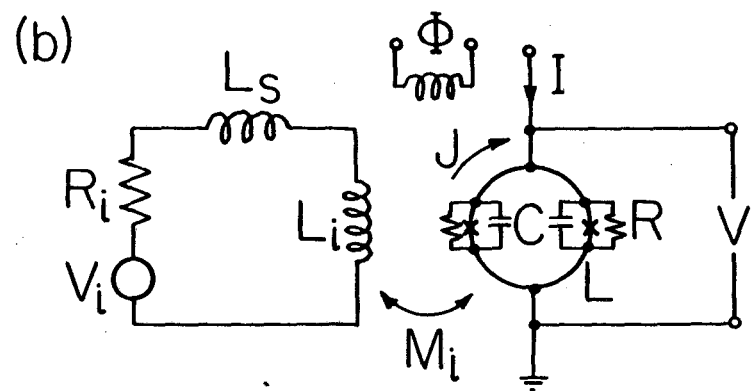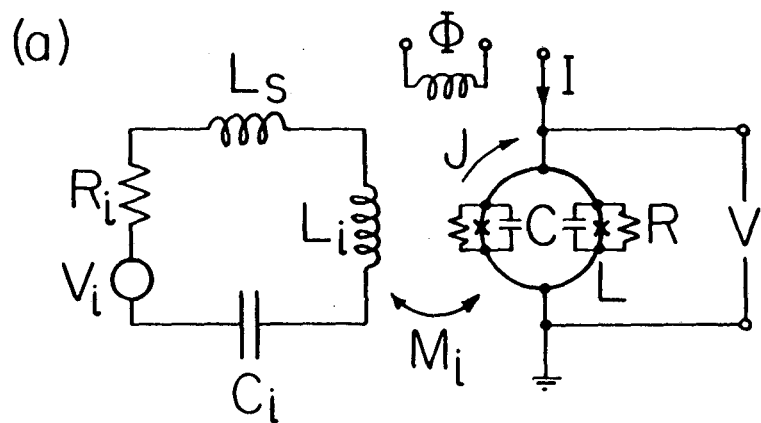
CHAPTER V

DC SQUIDS AS RADIO-FREQUENCY AMPLIFIERS: OPTIMIZATION THEORY

1. Introduction

In this chapter, we give a detailed description of the theoretical optimization of the SQUID input circuit and the predicted performance of radio-frequency amplifiers based on dc SQUIDs, both in the tuned and the untuned case.

This theory is based on the results of the preceding chapters. Chapter II was concerned with the theory of a SQUID coupled to an input circuit, and Chapter IV contained a discussion of the practical effects of the parasitic capacitance between the SQUID and the input coil: the lumped circuit model, with the addition of capacitive feedback, was found to be a relatively good approximation for a SQUID amplifier in its normal operating regime, that is, near maximum gain. We thus feel justified in using this model and the theory based on it to calculate the signal gain, the optimized source resistance and the optimized noise temperature of both tuned (Section 2) and untuned (Section 3) amplifiers. In Section 4 we also discuss the effects of parasitic capacitance on the input circuit. Section 5 contains some concluding remarks.

Figures 5.1(a) and (b) show a dc SQUID coupled to an input circuit consisting of a signal source $V_i(t)$ with resistance R_i in series with the input coil of inductance L_i, some stray inductance L_s, and, in the case of the tuned amplifier, a capacitance C_i. For convenience, we assume L_p to be zero here. The total impedance of the unloaded input circuit is Z_T and we define Z_i to be $Z_T - j\omega(L_i + L_s)$. As was shown in

Fig. 5.1 Configuration of (a) tuned and (b) untuned dc SQUID amplifiers.

XBL852-5898

the previous chapters, the coupled SQUID can be described in the lumped circuit approximation in terms of the parameters of a bare SQUID with a reduced inductance $L^r = (1 - \alpha_e^2)L$ [see Eq. (2.10)]. If we neglect the loading of the SQUID output, and assume $\partial J/\partial I$ to be zero, as is the case for a symmetric SQUID, we can write the voltage across a SQUID coupled to an input circuit as [Eq. (2.19)]

$$V(\omega) = V_N^r(\omega) + [M_i V_i + \alpha_e^2 L Z_i J_N^r(\omega)]V_\phi^r/Z_T^*(\omega), \tag{5.1}$$

where

$$Z_T^*(\omega) = Z_T(\omega) - \alpha_e^2 L J_\phi^r Z_i(\omega). \tag{5.2}$$

The voltage gain of the amplifier can be written in the form

$$G_V = V_o/V_i = M_i V_\phi^r/Z_T^*(\omega), \tag{5.3}$$

where V_o is the output signal voltage, while the power gain is

$$G = \left|\frac{V_o}{V_i}\right|^2 \frac{R_i}{R_D} = \frac{M_i^2(V_\phi^r)^2 R_i}{R_D|Z_T^*(\omega)|^2}. \tag{5.4}$$

Here, R_D is the dynamic output resistance of the SQUID.

The noise temperature of the amplifier is defined by

$$T_N(f) = S_V(f)/4k_B R_i G_V^2(f), \tag{5.5}$$

where $S_V(f)$ is the spectral density of the voltage noise at the output of the coupled SQUID, $V_N(t)$.

2. Tuned Amplifier

For the tuned amplifier shown in Fig. 5.1(a), Eq. (5.1) becomes

$$V_N(\omega) = V_N^r(\omega) + \alpha_e^2 L V_\phi^r (R_i + 1/j\omega C_i) J_N^r(\omega)/Z_T^*(\omega), \qquad (5.6)$$

where, from Eq. (5.2) and the reduced form of Eq. (4.2),

$$Z_T^*(\omega) = [R_i + \alpha_e^2 L(R_i \mathscr{L}^r + 1 \mathscr{R}^r C_i)] + j\omega[(L_i + L_s) + \alpha_e^2 L R_i \mathscr{R}^r]$$

$$+ (1 + \alpha_e^2 L \mathscr{L}^r)/j\omega C_i. \qquad (5.7)$$

We now assume that the amplifier is operated at the resonant frequency $f_0 = \omega_0/2\pi$ at which the imaginary term in Z_T^* tunes to zero:

$$\omega_0 = [(L_i + L_s + \alpha_e^2 L R_i \mathscr{R}^r) C_i/(1 + \alpha_e^2 L \mathscr{L}^r)]^{-1/2}. \qquad (5.8)$$

At the resonant frequency, Eqs. (5.6) and (5.7) simplify to

$$V_N(\omega_0) = V_N^r(\omega_0) + \frac{\alpha_e^2 L(R_i + 1/j\omega_0 C_i) J_N^r(\omega_0) V_\phi^r}{R_i + \Delta R_i}, \qquad (5.9)$$

where

$$\Delta R_i = \alpha_e^2 L(R_i \mathscr{L}^r + 1 \mathscr{R}^r C_i). \qquad (5.10)$$

We now assume that the quality factor, Q, is high so that $R_i \ll |1/j\omega C_i|$. Later is this section, we show that the optimization of a tuned amplifier implies $\alpha_e^2 Q \approx 1$, so that $\alpha_e^2 \ll 1$ in the high Q limit. Thus, in this limit, to an excellent approximation the SQUID parameters

resume their bare values. The resonant frequency becomes $\omega_o \approx [(L_i + L_s)C_i]^{-1/2}$ and Eq. (5.9) reduces to

$$V_N(\omega_o) \approx V_N^0(\omega_o) - j\omega_o M_i^2 V_\phi J_N(\omega)/(R_i + \Delta R_i), \qquad (5.11)$$

where $V_N^0(\omega_o)$ is the voltage noise across a bare, unreduced SQUID. In the approximation made here, we should also neglect ΔR_i in Eq. (5.11). However, because ΔR_i is, in practice, dominated by feedback via parasitic capacitance, it is convenient to retain this term for use later in the paper.

We can easily obtain the spectral density, $S_V(\omega_o)$, from Eq. (5.11). We optimize $T_N(f_o)$, obtained from Eq. (5.5), by setting $\partial T_N/\partial R_i = 0$ to find the optimal source resistance

$$R_i^{opt} = [(R_{io}^{opt})^2 + (\Delta R_i)^2]^{1/2}, \qquad (5.12)$$

where we have assumed ΔR_i to be independent of R_i, as is the case when ΔR_i is dominated by feedback (see Sec. 4). Here

$$R_{io}^{opt} = (\gamma_J/\gamma_V)^{1/2}\omega_o M_i^2 V_\phi/R \qquad (5.13)$$

is the optimal source resistance if ΔR_i can be neglected. We define γ_V and γ_J via the spectral densities of V_N and J_N, $S_V(f) = 2\gamma_V k_B TR$ and $S_J(f) = 2\gamma_J k_B T/R$. The optimized noise temperature is

$$T_N^{opt}(f_o)/T = \gamma_V R(R_i^{opt} + \Delta R_i)/M_i^2 V_\phi^2. \qquad (5.14)$$

For practical purposes, we now assume $\Delta R_i \ll R_{io}^{opt}$, and that for a SQUID with $\beta = 2LI_o/\Phi_o \approx 1$, $(\gamma_J/\gamma_V)^{1/2} \approx 1$ and $V_\phi \approx R/L$. Equations

(5.12), (5.13), and (5.14) reduce to

$$R_{io}^{opt} \approx \alpha^2 \omega_o L_i \qquad (5.15)$$

and

$$T_{No}^{opt}(f_o) \approx (\gamma_V \gamma_J)^{1/2} \omega_o L T / R. \qquad (5.16)$$

In addition, since $Q \approx \omega_o (L_i + L_s)/(R_i + \Delta R_i)$, the optimum value of Q is

$$Q \approx [1 + L_s/L_i]/\alpha^2 \qquad (5.17)$$

or

$$Q \alpha_e^2 \approx 1. \qquad (5.18)$$

The low value of α_e^2 implied by Eq. (5.18) for large values of Q justifies the use of the bare SQUID parameters. Finally, the power gain at resonance, Eq. (5.4), reduces to

$$G_o^{opt}(f_o) = M_i^2 V_\phi^2 / R_i R_D \approx V_\phi / \omega_o, \qquad (5.19)$$

where we have set $R_D \approx R$.

An important feature of any amplifier is its dynamic range, which we define as $\xi^2 \phi_o^2 / \langle \phi_N^2 \rangle$. Here, $\langle \phi_N^2 \rangle$ is the mean square equivalent flux noise, and $\xi \phi_o$ is the maximum rms flux that can be applied to the SQUID without introducing a serious nonlinearity; ξ is typically of the order of 10^{-1}. From the equipartition theorem,

$$\langle \Phi_N^2 \rangle = M_i^2 k_B (T + T_N)/(L_i + L_s) \approx L k_B (T + T_N)/Q, \qquad (5.20)$$

where we have used Eqs. (2.10) and (5.18). Thus, the dynamic range, D, is given by

$$D \approx \xi^2 \Phi_o^2 / \langle \Phi_N^2 \rangle \approx \xi^2 Q \Phi_o^2 / L k_B (T + T_N). \qquad (5.21)$$

The fact that D scales with Q indicates the desirability of operating with high values of Q.

To conclude this section, we list numerical estimates for the principal results we have obtained. For a SQUID with $L \approx 4 \times 10^{-10}$ H, $R \approx 8\Omega$, $\alpha^2 \approx 0.7$ and $\beta \approx 1$ and taking the computed values $V_\Phi \approx 2 \times 10^{10}$ s^{-1}, $\gamma_V \approx 8$ and $\gamma_J \approx 5.5$, for $f_o \approx 100$ MHz and $\xi^2 \approx 0.1$ we find $R_{io}^{opt} \approx 0.7 \, \omega_o L_i$, $T_N^{opt} \approx 0.2$ T, $G \approx 15$ dB, and $D \approx 6$ Q/(T/1K).

3. Untuned Amplifier

In the case of the untuned amplifier, shown in Fig. 5.1(b), the output voltage noise across the coupled SQUID is

$$V_N(\omega) = V_N^r(\omega) + \alpha_e^2 V_\Phi^r L R_i J_N^r(\omega)/Z_T^*, \qquad (5.22)$$

where

$$Z_T^*(\omega) = R_i(1 + \alpha_e^2 L \mathscr{L}^r) + j\omega[L_i(1 + \alpha_e^2 L R_i \mathscr{R}^r L_i) + L_s]. \qquad (5.23)$$

From Eq. (5.22) we find

$$S_V(\omega) = S_V^r(\omega) + \frac{2 S_{VJ}^r(\omega) \alpha_e^2 L R_i V_\Phi^r \mathrm{Re}(Z_T^*) + S_J^r(\omega)(\alpha_e^2 V_\Phi^r L R_i)^2}{|Z_T^*|^2}, \qquad (5.24)$$

where S_{VJ}^r is the cross-spectral density of $V_N^r(t)$ and $J_N^r(t)$. Equations (5.5) and (5.24) lead to

$$T_N(f) = \frac{S_V^r |Z_T^*|^2 + 2S_{VJ}^r \alpha_e^2 L R_i V_\phi^r \mathrm{Re}(Z_T^*) + S_J^r (\alpha_e^2 V_\phi^r L R_i)^2}{4k_B R_i M_i^2 (V_\phi^r)^2} . \qquad (5.25)$$

To make further progress, we now assume that the terms $\alpha_e^2 L/\mathscr{L}^r$ and $\alpha_e^2 L R_i/L_i \mathscr{R}^r$ in $Z_T^*(\omega)$ [Eq. (5.9)] may be neglected with respect to unity, even in the case $L_s = 0$ for which $\alpha_e = \alpha$ may approach unity. These approximations are valid since $L/\mathscr{L}^r < 1/10$ for ϕ near $\phi_0/4$ or $3\phi_0/4$, and $L R_i/L_i \mathscr{R}^r \sim \omega L/R \ll 1$. In this approximation Eq. (5.25) reduces to

$$T_N(f) \approx \frac{1}{4k_B M_i^2 (V_\phi^r)^2} \left\{ \frac{\omega^2 (L_i + L_s)^2 S_V^r}{R_i} + R_i [S_V^r + 2\alpha_e^2 L V_\phi^r S_{VJ}^r + (\alpha_e^2 L V_\phi)^2 S_J^r] \right\}. \qquad (5.26)$$

In practice, ΔL_i is dominated by capactive feedback, and its value involves R_i. Hence, the optimization procedure is complicated when this term is retained. To simplify matters, since the value of $|\Delta L_i|$ due to capacitive feedback is typically less than $0.2L_i$, we have neglected ΔL_i in the optimization. The error introduced is no larger than the uncertainties in the parameters of the SQUID.

Optimizing with respect to R_i for a given frequency, coupling and inductance in the input circuit, we find

$$R_i^{opt}(f) \approx \omega(L_i + L_s) \left[1 + \frac{2\alpha_e^2 L V_\phi^r \gamma_{VJ}^r}{\gamma_V^r R} + \left(\frac{\alpha_e^2 L V_\phi^r}{R} \right)^2 \frac{\gamma_J^r}{\gamma_V^r} \right]^{-1/2} . \qquad (5.27)$$

The corresponding optimized noise temperature is

$$T_N^{opt}(f) \approx \omega^2 (L_i + L_s) \gamma_V^r R T / \alpha_e^2 L (V_\phi^r)^2 R_i^{opt}(f). \qquad (5.28)$$

We now estimate the noise temperature of an untuned amplifier using the (unreduced) parameters of the SQUID described in Sec. 3.1, namely $L \approx 4 \times 10^{-10}$ H, $R \approx 8$ Ω, $\alpha^2 \approx 0.7$, and $\beta \approx 1$. Assuming $\alpha_e^2 \approx 0.6$, we obtain $\beta^r \approx 0.4$ and, from analog and digital simulations (Tesche and Clarke, 1977, 1979; de Waal et al., 1984), $V_\Phi^r \approx 2.5 \times 10^{10}$ s^{-1}, $\gamma_V^r \approx 9$, $\gamma_J^r \approx 6$ and $\gamma_{VJ}^r \approx 6$. Thus, Eq. (5.27) predicts $R_i^{opt}/\omega(L_i + L_s) \approx 0.7$. At 100 MHz the predicted noise temperature is $T_N^{opt}/T \approx 1.5\gamma_V^r \omega R/\alpha_e^2 L(V_\Phi^r)^2 \approx 0.6$. The optimized source resistance is relatively insensitive to the values of α_e^2, V_Φ^r, γ_V^r, γ_J^r, γ_{VJ}^r and hence of β^r because of the square root-dependence on these quantities. The predicted noise temperature is higher than for the tuned amplifier by a factor of about 3, largely because the voltage gain is lowered by the inductive impedance of the input coil. We also note that the dynamic range for the untuned amplifier is much smaller than for the tuned amplifier because of the strong coupling ($\alpha_e^2 \approx 1$) required to obtain a low noise temperature [see Eq. (5.28)]. The first equality in Eq. (5.20) yields a dynamic range of about 8/(T/1K).

4. Capacitive Feedback

As mentioned earlier in this chapter and discussed extensively in the preceding chapter, in practice the input impedance of a dc SQUID (as well as the parameters of the SQUID) is modified not only by inductive coupling between the SQUID and the input coil, but also by capacitive feedback via parasitic capacitance between the SQUID and the input coil. Hence, the total effective input impedance of the amplifier can be written as

$$Z_T^*(\omega) = Z_T(\omega) + \Delta Z_T^{(1)}(\omega) + \Delta Z_T^{(2)}(\omega). \qquad (5.29)$$

Here, $\Delta Z_T^{(1)}(\omega) = - \alpha_e^2 L J_\phi^r Z_i(\omega)$ is due to inductive coupling and $\Delta Z_T^{(2)}(\omega)$ is caused by capacitive feedback. To simplify our calculations we use the model shown in Fig. 4.11(a), in which we replace the distributed parasitic capacitance between the SQUID and the input circuit by a lumped capacitor C_p, and neglect any stray inductance. In the limits $1/\omega C_p \gg R_D$, where the feedback does not load the voltage across the SQUID, and $\omega^2 \ll 1/L_i C_p$, the voltage gain of the amplifier becomes [see Eq.(4.7)]

$$G_V \approx M_i V_\phi^r [Z_T^*(\omega) - j\omega M_i V_\phi^r C_p Z_i(\omega)]^{-1}. \qquad (5.30)$$

In the second term we have assumed $Z_T^*(\omega) - j\omega L_i \approx Z_i(\omega)$; the input impedance changes due to inductive coupling are small, typically less than 10%. Thus, we see that

$$\Delta Z_T^{(2)}(\omega) \approx - j\omega M_i V_\phi^r C_p Z_i(\omega). \qquad (5.31)$$

This impedance change due to capacitive feedback adds to the change due to inductive coupling to the SQUID, and should also be taken into account in the optimization procedure as indicated in Secs. 2 and 3.

We note that the SQUID voltage noise that is fed back capacitively into the input circuit can be shown to contribute less than 10% to the total output voltage noise for any practical set of parameters. Thus, this noise can be neglected in the optimization procedure, that is, we consider any reflected resistance to be noiseless.

4.1 Tuned Amplifier

Our investigation in Chapter IV showed that, for the planar, thin-film SQUIDs with tightly-coupled input coils the inductance change

in a high-Q input circuit is dominated by the inductive coupling, whereas the resistance change is dominated by the capacitive feedback. With these approximations, we can write the total effective input impedance at the resonant frequency as

$$Z_T^*(\omega_o) \approx Z_T(\omega_o) - j\omega_o\alpha^2(L/\mathscr{L})L_i - \omega_o^2 M_i V_\phi C_p L_i, \qquad (5.32)$$

where the last term on the right-hand side is the real part of $\Delta Z_T^{(2)}(\omega_o)$. As mentioned in Sec. 2, the reduced SQUID parameters can be replaced by the bare SQUID parameters in the high-Q case.

From Eq. (5.32) we can easily deduce the fractional change in the resonant frequency due to its magnetic coupling to the SQUID,

$$\frac{\Delta f_o}{f_o} \approx - \frac{\Delta L_i}{2L_i} \approx - \frac{\Delta L_i}{2\alpha^2 Q L_i} \approx \frac{L}{2Q\mathscr{L}}, \qquad (5.33)$$

and the fractional change in Q, due to capacitive feedback,

$$\frac{\Delta Q}{Q} \approx - \frac{\Delta R_i}{R_i^{opt}} \approx \frac{\omega_o M_i V_\phi C_p}{\alpha^2}. \qquad (5.34)$$

The fractional change in f_o is independent of f_o and inversely proportional to Q, while the fractional change in Q scales as ω_o.

4.2 Untuned Amplifier

For an untuned amplifier, from Eq. (5.31) we find an additional change in the input impedance:

$$\Delta Z_T^{(2)} \approx - j\omega M_i V_\phi^r C_p R_i. \qquad (5.35)$$

Numerical estimates suggest that in this case changes in the input in-

ductance are likely to be dominated by capacitive feedback. This change will affect the frequency response of the amplifier. For example, the fractional change in the roll-off frequency, $f' = R_i/2\pi(L_i + \Delta L_i)$, is given approximately by

$$\frac{\Delta f'}{f'} = -\frac{\Delta L_i}{L_i} = +\frac{M_i V_\phi^r C_p R_i}{L_i} .$$
(5.36)

5. Concluding Summary

We have discussed the optimization of tuned and untuned radiofrequency amplifiers based on the noise theory and experimental measurements of the input impedance presented in the previous chapters . The theory assumes that the lumped circuit model is valid and that α^2 is not necessarily small. In each case, the optimization procedure leads to an expression for the optimal ratio $R_i/\omega L_i$ and thus to the optimized gain, noise temperature and dynamic range. For the case of a tuned amplifier, optimum performance is obtained when the conditions $R_i \approx \alpha^2 \omega L_i$ and $Q\alpha_e^2 \approx 1$ are satisfied. The latter condition implies that when Q is reasonably large and α_e^2 correspondingly small, the modification of the SQUID parameters by the input circuit is negligible.

In the practical amplifiers we have studied, the parasitic capacitance between the SQUID and the input inductance produces feedback from the output to the input circuit. For the tuned amplifier, this feedback produces an additional (cold) resistance in the input circuit that dominates that due to the dynamic input impedance of the SQUID. For the untuned case, the feedback produces an additional inductance that similarly dominates the contribution from the SQUID.

As a final comment on the theory, we emphasize that R_i is the

(given) resistance of the voltage source. If the voltage source happens to be a superconducting coil with $R_i = 0$, as would be the case for a magnetometer, our results should <u>not</u> be interpreted as implying that one should necessarily add an additional resistance to optimize the performance.

CHAPTER VI

## DC SQUIDS AS RADIO-FREQUENCY AMPLIFIERS: EXPERIMENTAL RESULTS

1. Introduction

We now discuss the performance of untuned and tuned rf amplifiers that are designed according to the prescriptions obtained in the previous chapter. The dc SQUIDs used were described in Chapter III. We describe the experimental realization of the amplifiers and compare their measured performance with the predictions of our model calculations in Chapter V.

2. Untuned Amplifier

Our design was based on a source impedance, R_i, of 50 Ω and a signal frequency of 100 MHz. The corresponding value of L_i for an optimized design is 120 nH, which is approximately the value of a 20-turn input coil (Ketchen and Jaycox, 1982). The mutual inductance, M_i, is about 6 nH, and $\alpha_e^2 \approx 0.7$.

The experimental configuration used to measure the power gain and noise temperature is shown in Fig. 6.1. The SQUID was enclosed in a superconducting shield and connected directly through a 50-Ω rigid coaxial cable to a low-noise, room temperature amplifier with a 50-Ω input impedance (MITEQ AV-2A-0150, with a bandwidth of 1-500 MHz and a noise temperature for a 50 Ω-source of about 120K). Since the dynamic output resistance of the SQUID, R_D, was about 10 Ω, only about 55% of the available signal power was coupled into the amplifier. The output of the amplifier was coupled to a spectrum analyzer that was used to observe the SQUID response directly, and that served as a narrow-
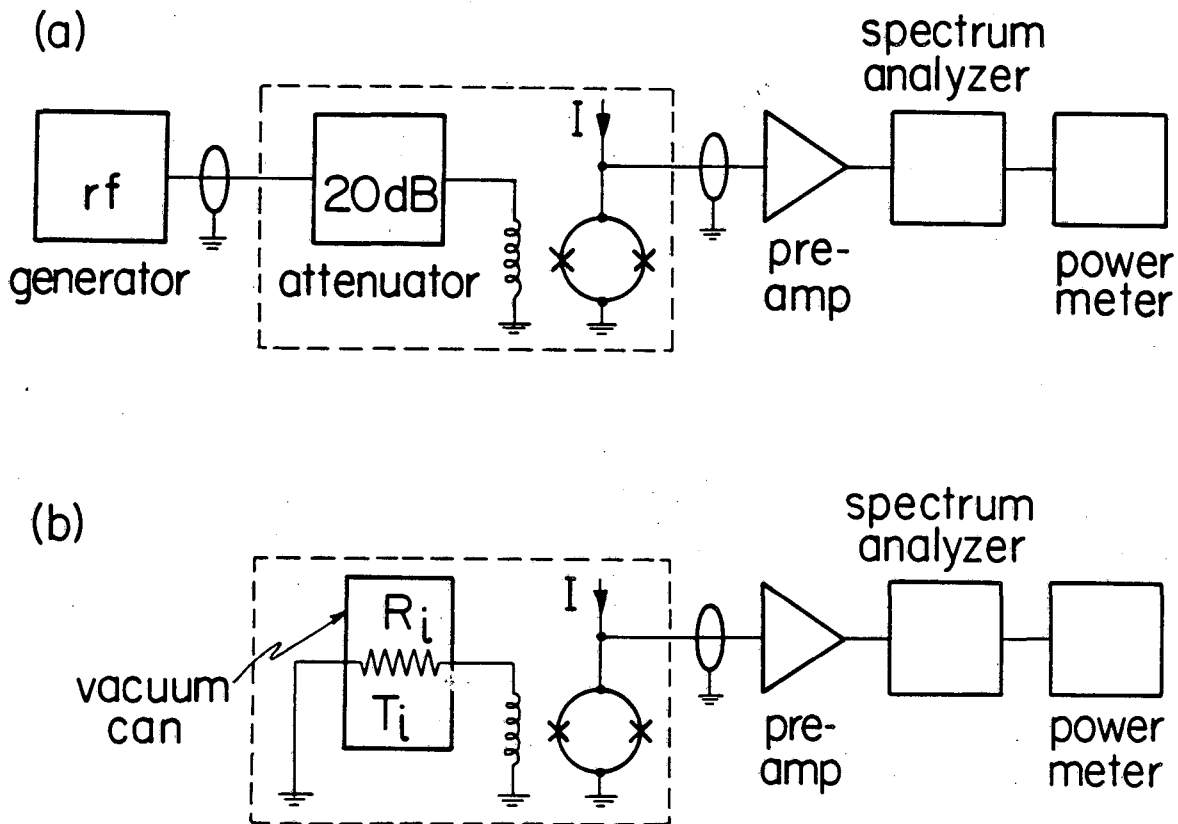
Fig. 6.1 Circuits to measure (a) power gain and (b) noise temperature of untuned SQUID amplifier.

bandpass, tunable mixer; power measurements were made by means of a power meter connected to the IF output of the analyzer.

To measure the gain [Fig. 6.1(a)], we injected a calibrated signal, typically 10^{-15} W, into the input coil via a cold, 20-dB attenuator that reduced the room-temperature noise to an acceptable level and presented a cold, 50-Ω impedance to the input coil. To measure the noise temperature of the amplifier [Fig. 6.1(b)], we connected the input coil to a 50-Ω resistor that was enclosed in a vacuum can (see Fig. 6.2). The temperature, T_i, of this resistor could be raised above the bath temperature by means of a heater. The 50-Ω resistor was a SMA coaxial terminator connected via a 50 mm-long rigid, stainless steel, coaxial cable to a SMA feedthrough with a glass-to-metal-seal that was soft-soldered into the brass vacuum can. The stainless steel, coaxial cable (2 mm o.d. with teflon dielectric) minimized the heat flow between the heated terminator and the helium bath, while adding only 2 Ω of electrical resistance. To reduce temperature gradients across the terminator even further, it was glued inside a tight-fitting copper tube. A metal-film resistor and a carbon resistor were glued to the outside of the copper tube as a heater and a thermometer, respectively. These resistors were connected to electrical feedthroughs in the can. We used fine manganin wires (0.05 mm diam) for the thermometer leads to minimize temperature gradients across it. The diameter of the copper wires (0.1 mm) for the heater, however, was chosen to provide a thermal time-constant of 10-30 sec. A small quantity of powdered charcoal was added to the can before sealing it to adsorb any traces of helium gas at liquid helium temperatures.

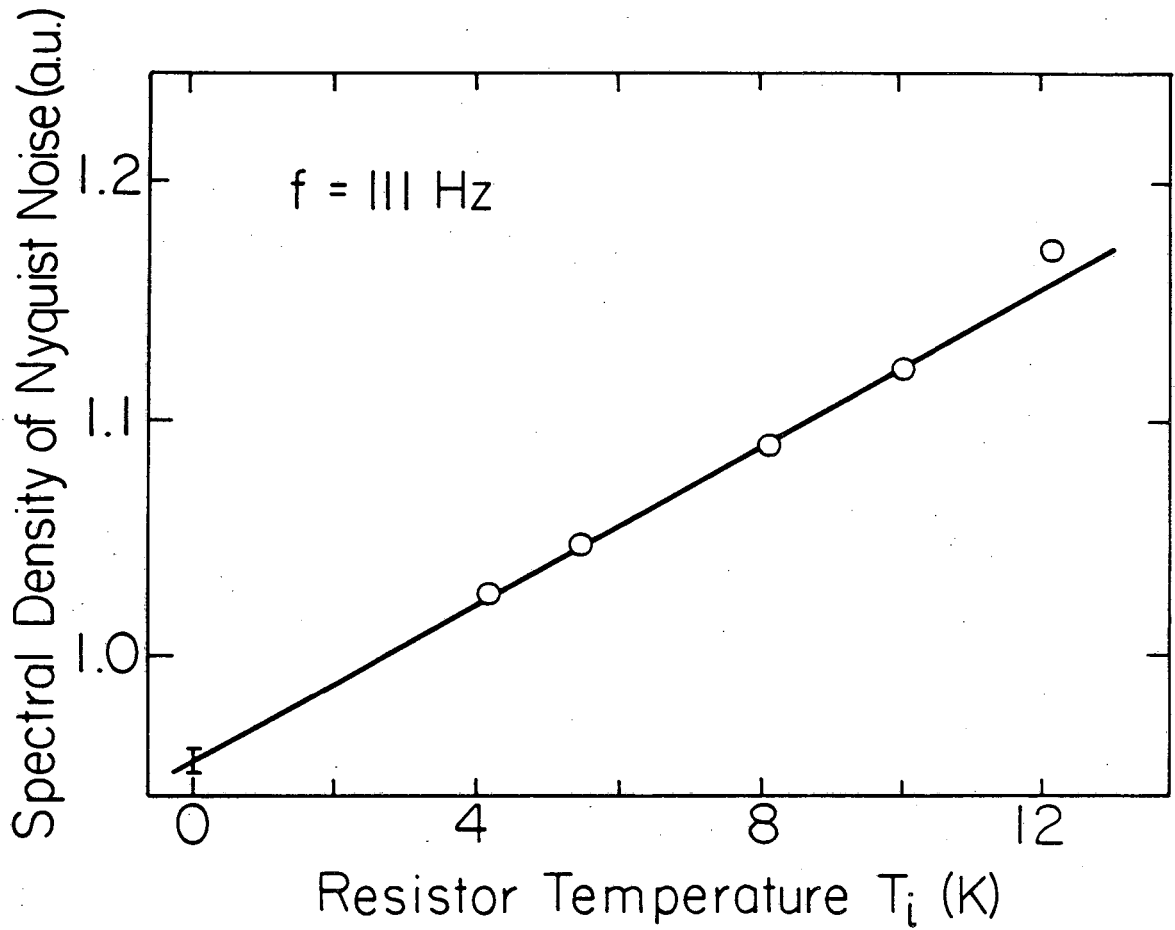The calibration of the carbon resistance thermometer was confirmed
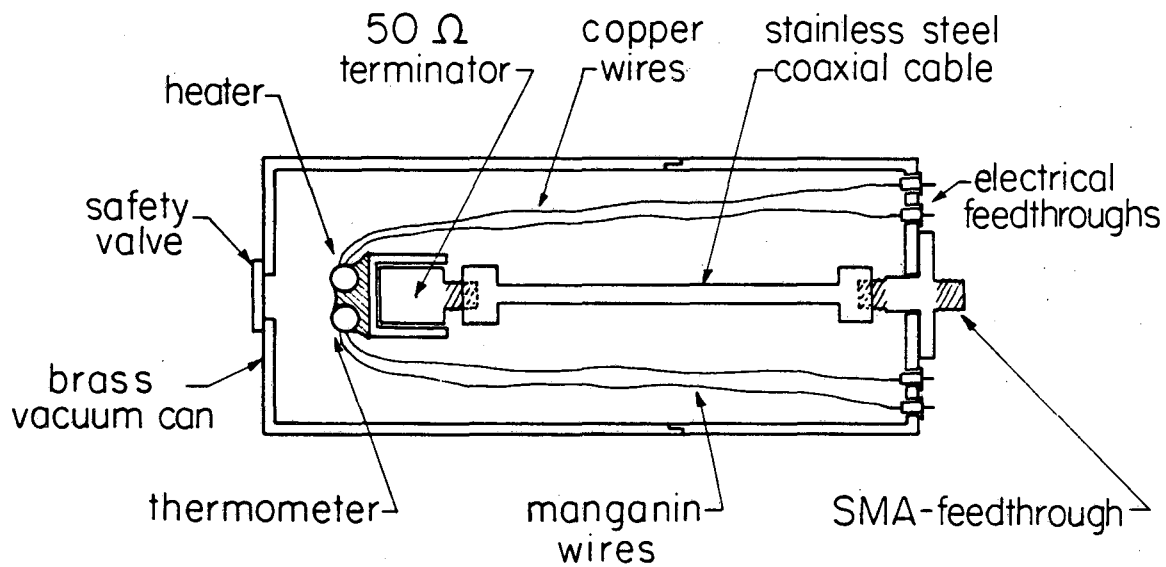
Fig. 6.2   Variable temperature Nyquist noise source for noise temperature measurements.

in a separate experiment in which we measured the Nyquist noise of the 50 Ω resistor at 111 Hz as a function of the temperature indicated by the thermometer. The 50 Ω resistor was matched to a PAR 113 preamplifier by means of a PAR 190 transformer, and the spectral density of the Nyquist noise was obtained with a spectrum analyzer. The results of this calibration are shown in Fig. 6.3. The straight line is a least squares fit to the reference points at 4.2K, 77K and 295K. The data points obtained in the temperature range from 4 to 10K are in good agreement with this line.

For the measurements of the gain and noise temperature of the SQUID amplifiers, we adjusted the flux and current biases to maximize the gain. The bias voltage was typically 20 μV, corresponding to a Josephson frequency of about 10 GHz. For the gain measurements we used a SQUID with $\beta \approx 3$ and $V_\phi^r \approx 4 \times 10^{-10}$ s^{-1} at 4.2K. The power gain at 100 MHz predicted from Eq. (5.4) is about 16.5 dB assuming $R_D \approx R \approx 8$ Ω.

Figure 6.4 shows the power gain vs. frequency for a typical SQUID amplifier at 4.2K. Note that the impedance mismatch between the SQUID and the room-temperature amplifier introduced a loss of about 3 dB. Curves (a) and (b) were obtained with flux biases of $\phi = (n \pm 1/4)\phi_0$, for which the values of V_ϕ^r were approximately equal in magnitude but opposite in sign. The gain drops by about 5 dB as the frequency increases from 10 to 100 MHz, as a result of the increasing impedance of the inductive input. At about 160 MHz, there is a resonance that, depending on the sign of V_ϕ^r, produces either a dip or a peak in the gain, and which arises presumably, from the self-resonance of the input coil. The resonant frequency, $1/2\pi(L_i C_p)^{1/2}$, corresponds to a parasitic capacitance of about 8 pF in this particular device, in

Fig. 6.3 Calibration of carbon resistance thermometer: spectral density of Nyquist noise (in arbitrary units) vs. temperature.
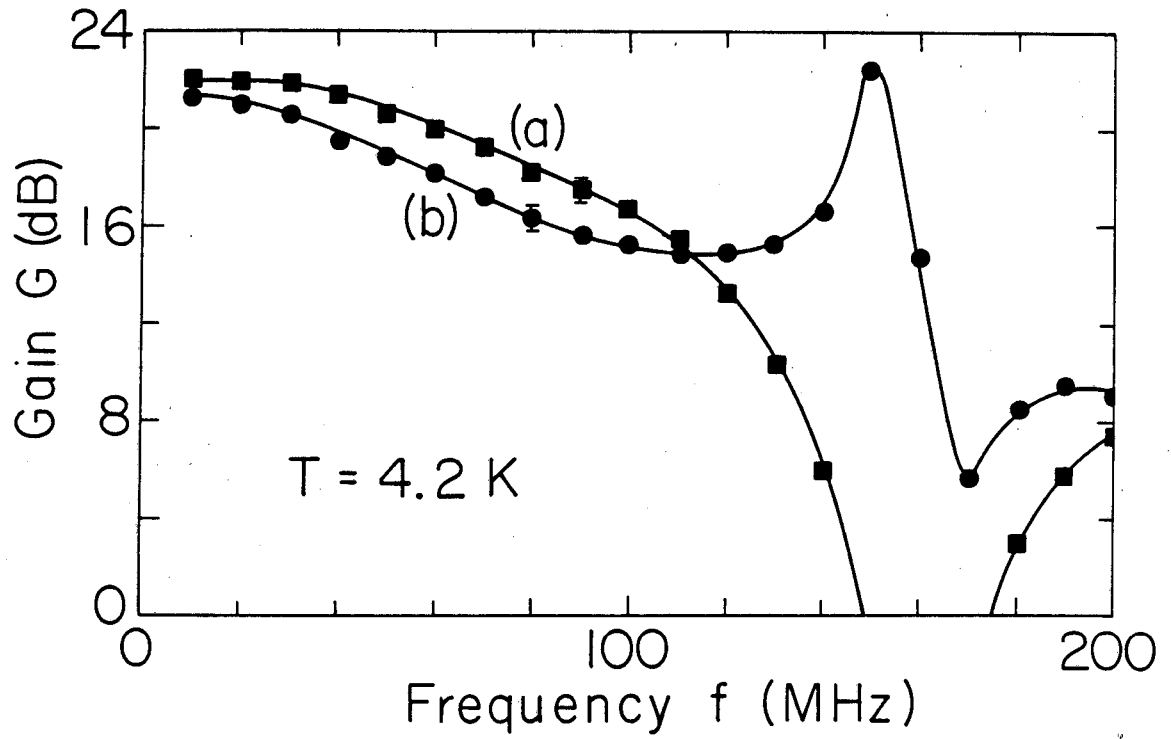
Fig. 6.4   Gain vs. frequency for untuned dc SQUID amplifier for (a) ne-
gative and (b) positive V_Φ.

reasonable agreement with our estimate of about 5 pF in Chapter IV. At frequencies above this resonance, the amplifier exhibited gain up to about 500 MHz, and a discernible response up to well above 1 GHz. The two gain curves fall to 3 dB below their low frequency values at frequencies that differ by about 25 MHz, corresponding to a fractional change of about ± 0.2. This shift arises from changes in the input inductance due to capacitive feedback; from Eq. (5.36), we predict $\Delta f'/f' \approx \pm 0.6$. As for the change in resistance in the tuned case (see Chapter IV), our simple model overestimates the effect.

The dynamic range was about 10^8 per unit bandwidth, or approximately unity in the full bandwidth of the amplifier.

When the SQUID was cooled to 1.5K, the gain below the resonance increased by about 3 dB: this effect was due to the increase in V_ϕ^r, which, in turn, arose from the reduced noise rounding of the current-voltage characteristics.

For the noise temperature measurements, we used a SQUID with $\beta \approx 2$ for which $V_\phi^r \approx 2.5 \times 10^{10}$ s^{-1} at 4.2K. The total noise temperature of the system, T_N^T, referred to the input of the amplifier, is

$$T_N^T = T_N + T_i + T_N^A(R_D)/G, \qquad (6.1)$$

where T_N^A is the noise temperature of the room temperature amplifier, which depends on R_D. We measured $T_N^A(R_D)$ by replacing the SQUID with a cold resistor, and measuring the noise from the amplifier. We determined the contribution, T_i, of the 50-Ω resistor by plotting the total output noise power vs. T_i, as shown in Fig. 6.5. The slope of the plot yields the total system gain, which is higher at the lower tempera-
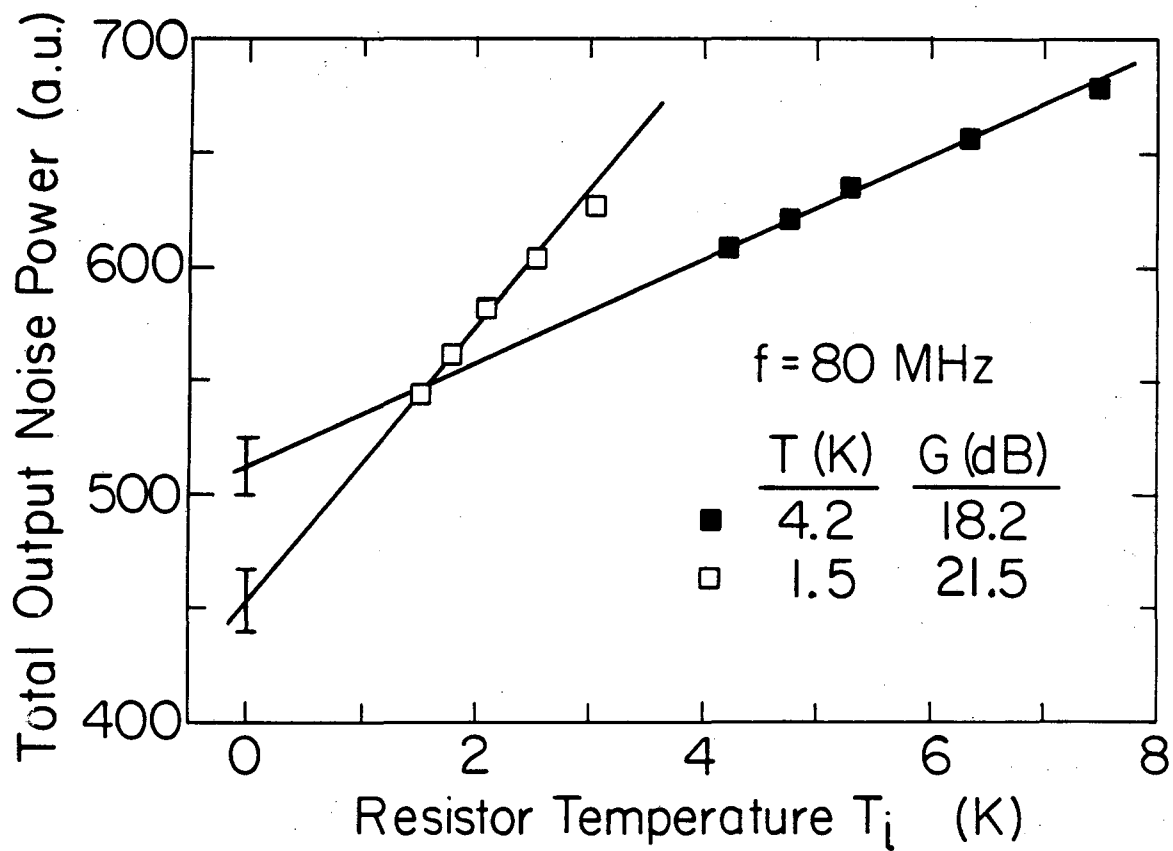
Fig. 6.5 Total output noise power (arbitrary units) vs. T_i at 80 MHz at 4.2K and 1.5K for untuned dc SQUID amplifier.

ture. The extrapolation of the lines through the data to $T_i = 0$ yields $T_N + T_N^A/G$, from which the latter term can be subtracted.

The values of G and T_N obtained at three frequencies and two operating temperatures are listed in Table VI.I. At each frequency, as the temperature is lowered from 4.2K to 1.5K the gain increased by about 3 dB, while the noise temperature was reduced by a factor somewhat greater than the ratio of the bath temperatures, presumably because of the increase in V_ϕ^r. At 4.2K, the noise temperature was roughly equal to the bath temperature, while at 1.5K the noise temperature was roughly 2/3 of the bath temperature. These values should be compared with the value predicted by Eq. (5.28) using $\gamma_V^r \approx 16$ and $\alpha_e^2 \approx 0.6$, about 0.6T.

3. Tuned Amplifier

For the tuned amplifier, we used a SQUID with a 4-turn input coil, which had roughly five times less parasitic capacitance than the 20-turn coil. In this case, $\beta \approx 4$, $M_i \approx 1$ nH, $L_i \approx 5.6$ nH, $\alpha^2 \approx 0.6$, and the measured value of V_ϕ was about 3×10^{10} s^{-1}. The self-resonance of the input coil was about 450 MHz with a Q of about 100, so that one might expect to be able to use this amplifier at frequencies up to about 300 MHz.

We first made measurements of the impedance reflected into the input circuit at a frequency of about 27 MHz. At this relatively low frequency we were able to connect a spectrum analyzer with a high input impedance across the input circuit without reducing its Q substantially. The general behavior of this relatively high-β SQUID was very similar to that described in Chapter IV. The maxima of $|L/\mathscr{L}|$ occurred at $\phi = n\phi_0/2$; their values were somewhat higher than for a SQUID with $\beta = 1$,

but never exceeded 0.6 for any values of the bias parameters. Thus, the maximum fractional change in input impedance, $|\Delta L_i/L_i| = \alpha^2|L/\mathscr{L}|$, never exceeded 0.4. In practice, one operates the amplifier within $\pm\, \Phi_0/10$ of the $(n \pm 1/4)\Phi_0$ bias points, a range over which $|\Delta L_i/L_i| < 0.15$. The change in input resistance, ΔR_i, scales with V_Φ and thus has its maximum magnitude near the operating point of the amplifier. At 27 MHz, we found $|\Delta R_i(max)| = 30$ mΩ. Hence, at 100 MHz, we expect $|\Delta R_i|$ not to exceed 0.4 Ω, a correction of about 20% to the optimal input resistance $(\alpha^2\omega L_i)$ of about 2 Ω. Over the operating range, ΔR_i should not change by more than 7%.

These preliminary measurements, together with Eqs. (5.10), (5.11), (5.30), and (5.31), enable us to make the following predictions for a tuned amplifier at 4.2K and at 100 MHz: $|\Delta f/f_0| < 1/3Q$ and $|\Delta Q/Q| < 0.2$ for any bias conditions, and $T_N^{opt} = 1.1$K, using the values $\Upsilon_V = 25$ and $\Upsilon_J = 6$ (obtained from our analog simulator with $\beta = 4$). The predicted power gain, $M_i^2 V_\Phi^2/R_i R_D$ is about 17 dB, assuming $R_i = 2\ \Omega$ and $R_D = 8\ \Omega$.

We tested our tuned rf amplifier at frequencies near 100 MHz with $R_i = 2\ \Omega$ and $C_i = 20$ pF. A cold, 50-Ω signal source (as for the untuned amplifier) was connected across the input resistance. The resonant frequency and average Q of the input circuit were about 113 MHz and 36. This resonant frequency corresponds to a stray series inductance, L_s, of about 90 nH, so that $\alpha_e^2 = 0.036$. Hence the value of $Q\alpha_e^2$ was about 1.3, close to the optimal value. The maximum shift in the resonant frequency as the flux bias was varied over a flux quantum was ± 0.8 MHz or less than $\pm 1\%$ of f_0, as expected. The fractional change in Q between $\Phi = (n + 1/4)\Phi_0$ and $(n - 1/4)\Phi_0$ was $\pm 25\%$, in approximate agreement with our prediction, and, furthermore, verifying that ΔR_i

scales with ω^2. The associated change in power gain was ± 2.7 dB.

We measured the power gain and noise temperature (Fig. 6.6) of the amplifier using a configuration similar to that shown in Fig. 6.1(b), with a 2 Ω source resistor in the vacuum can. In this case, we eliminated the resistance of the steel center conductor of the rigid coaxial cable by using a niobium wire. In this configuration, the stray inductance was increased somewhat, and the resonant frequency was reduced to 93 MHz. At a bath temperature of 4.2K, the measured gain was 18.6 ± 0.5 dB and the noise temperature was 1.7 ± 0.5K (Table VI.I).

The dynamic range in the bandwidth of the tuned input circuit was about 40 for Q ≈ 45.

4. Concluding Summary

The measured performance of the radiofrequency amplifiers is summarized in Table VI.I. The predicted performance is also listed, based on the measured low frequency values of V_ϕ (which are within ± 50% of model predictions) and computed values of γ_V and γ_J. We note, in particular, that we have neglected the effects of stray capacitance on the noise parameters. The measured gain could have been increased by 2 or 3 dB with the aid of a matching circuit between the output of the SQUID and the room temperature preamplifier. Given the uncertainties in the values of various parameters, the error in the predicted power gain might be as high as 3 dB, and the predicted noise temperatures might be in error by as much as 50%. We feel that the agreement between the measured and predicted values is very reasonable. Thus, a lumped circuit model with the addition of capacitive feedback, although a relatively crude approximation to the real device, appears to give an adequate description of
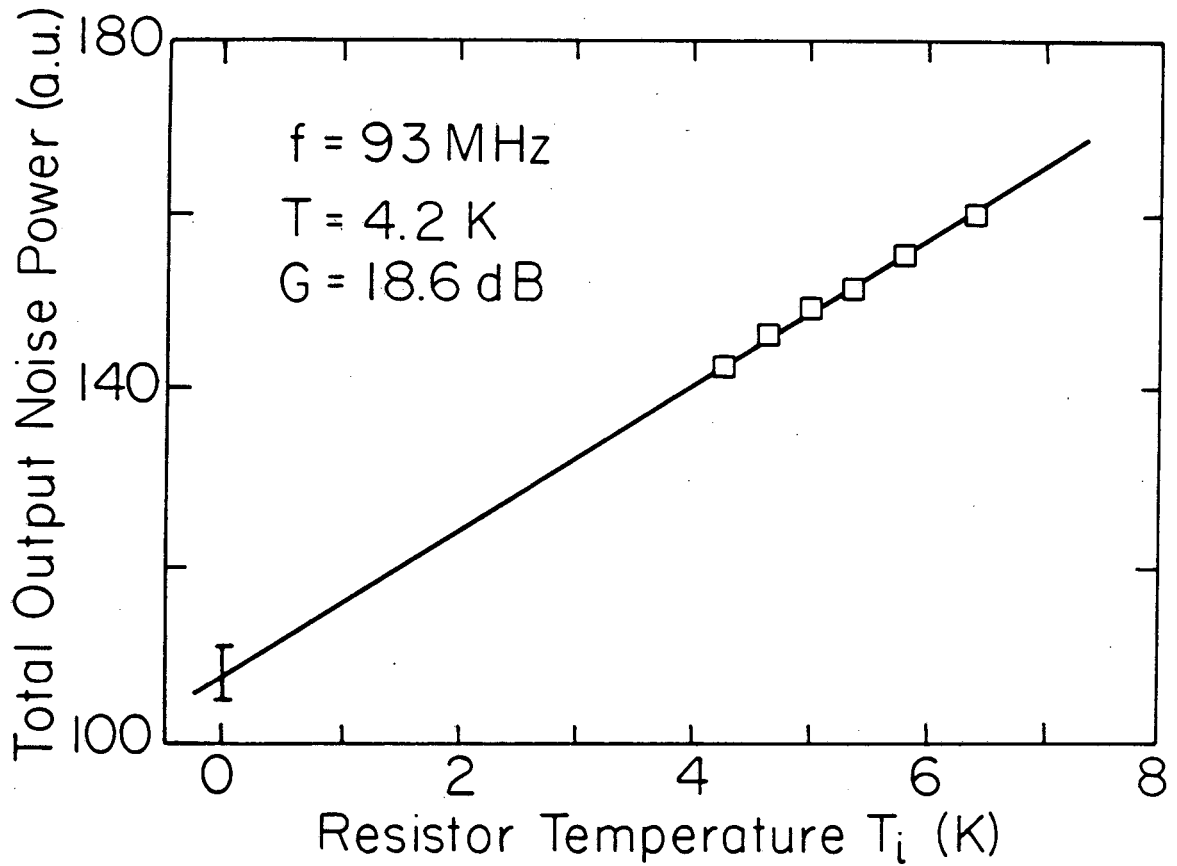
XBL852-5897

Fig. 6.6   Total output noise power (arbitrary units) vs. T_i at 93 MHz at 4.2K for tuned dc SQUID amplifier.

Table VI.I. Measured and predicted power gain G and noise temperatures

T_N for a dc-SQUID radiofrequency amplifier.

	Frequency (MHz)	G(dB)		T_N(K)	
		measured	predicted	measured	predicted
T = 1.5K untuned	60	24,0 ± 0.5		1.2 ± 0.3	
	80	21.5 ± 0.5		0.9 ± 0.3	
	100	19.5 ± 0.5	18.5	1.0 ± 0.4	0.9
T = 4.2K untuned	60	20.0 ± 0.5		4.5 ± 0.6	
	80	18.0 ± 0.5		4.1 ± 0.7	
	100	16.5 ± 0.5	16.5	3.8 ± 0.9	2.5
T = 4.2K tuned	93	18.6 ± 0.5	17	1.7 ± 0.5	1.1

the performance of SQUID amplifiers.

In the experiments on the tuned amplifier described here, a low value of α_e^2 was achieved by means of a substantial series inductance in the input circuit.   In the future design of SQUIDs for tuned amplifiers, however, it would be advantageous to lower α^2 by increasing the separation between the SQUID and the input coil, thereby substantially reducing the parasitic capacitance, perhaps to a negligible level.

CHAPTER VII

DEVELOPMENT OF A PULSED SQUID-NQR SYSTEM

1. Introduction

Superconducting devices have been used for almost two decades for the detection of magnetic resonance (Silver and Zimmerman, 1967; Hirschkoff et al., 1970; Bishop et al., 1971; Day, 1972; Meredith et al., 1973; Webb, 1977; Chamberlin et al., 1979; Suzuki et al., 1980; Pickens et al., 1984; Ehnholm et al., 1979; Wennberg et al., 1984). Most of this work has taken advantage of the high sensitivity of SQUIDs as magnetometers in the audio frequency range. As a result, measurements have been restricted to the study of magnetic resonance at low frequencies or to changes in the static susceptibility of a sample induced by a resonance at high frequency. However, the development of extremely low noise radio-frequency [rf] amplifiers based on dc SQUIDs described in the previous Chapters, now enables one to use these devices for the direct detection of pulsed magnetic resonance at frequencies up to about 300 MHz. In this chapter (Hilbert et al., 1985) we describe a system for the detection of nuclear quadrupole resonance [NQR] (Bloom et al., 1954) at about 30 MHz using a dc SQUID as a rf amplifier.

2. Experimental apparatus

Figure 7.1 is a schematic of the experimental set-up. A rf generator feeds a continuous, sinusoidal signal into a gate that is triggered by a pulse generator. The resulting rf pulse is amplified and coupled into the cold transmitter coil via an impedance matching circuit. The sample is located inside a pick-up coil that is connected in series with
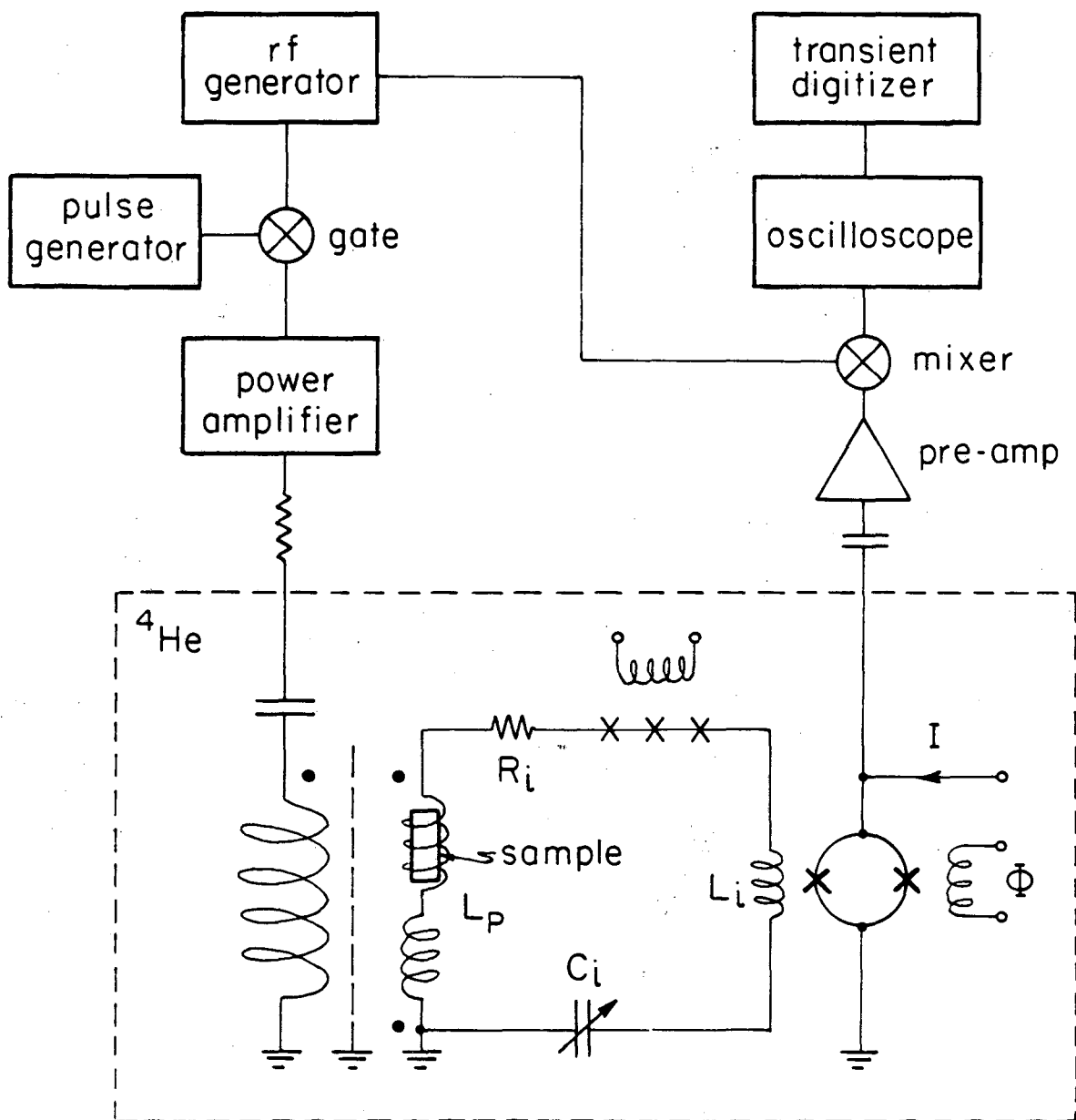
Fig. 7.1   Schematic layout for SQUID-based detection of NQR.

XBL 855-6216

an identical, oppositely-wound coil. Both coils are actually situated inside the transmitter coil, and can be moved along their mutually concentric axis so as to minimize their inductive coupling to the transmitter coil. In addition, a grounded Faraday shield between the transmitter and pick-up coils minimizes capacitive coupling. An optimum balance of about 3 parts in 10^5 is possible. The gradiometer-like configuration protects the SQUID from the rf-pulses: A sufficiently large current induced into the input circuit could trap flux in the Josephson junctions of the SQUID or even drive the input coil normal and damage the SQUID permanently. After the rf pulse is turned off, the precessing magnetization of the sample induces a signal voltage across the pick-up coil. The pick-up coils are connected in series with an air-capacitor C_i (adjustable from the top of the cryostat), the input coil L_i of a dc SQUID, and a series array of 20 Josephson tunnel junctions. The resistor R_i represents contact resistance and losses in the capacitor. The dc SQUID is a planar, thin-film device tightly coupled to a 4-turn spiral input coil, and has been described in Chapters III and VI. The SQUID is attached to a fiberglass mount, together with an auxiliary flux bias coil, and enclosed in a super-conducting Nb shield. The SQUID output is matched to a low noise, room temperature amplifier via a capacitor that, together with the coaxial line, transforms the output resistance to 50 Ω. The amplified signal is mixed down by a double balanced mixer with a reference supplied by the rf generator. The mixed-down signal is passed through a low-pass filter and observed on an oscilloscope, and, after digitizing, stored in a computer for further analysis or averaging.

A novel feature of the input circuit is the series array of twenty

10 μm × 10 μm Nb-NbOx-PbIn Josephson tunnel junctions. Each junction has a critical current of about 4 μA, and a hysteretic current-voltage characteristic with a resistance of about 50 Ω at voltages above the sum of the energy gaps. For signal currents below the critical current, the array has zero resistance. On the other hand, the relatively large current induced by each rf pulse causes the junctions to switch rapidly to the resistive state with a total resistance of about 1 kΩ. Thus, the array acts as a Q-spoiler, not only providing additional protection for the SQUID but, more importantly, reducing the ring-down time of the tuned circuit after the end of the rf pulse. An array is used to avoid damage to the junction that might occur if a single junction were used, and to obtain sufficient damping. The quality factor Q is about 1/2 with the junctions in the resistive state. The switching threshold of the Q-spoiler, that is, the critical current of the junctions, can be varied by means of a static magnetic field (shielded from the sample) applied parallel to the plane of the films.

3. System Test

We tested our pulsed SQUID-NQR detector using approximately 0.32 cm^3 of powdered $NaClO_3$. The filling factor, referred to both pick-up coils, was 0.13. At 4.2K the ^{35}Cl nuclei exhibit a quadrupole resonance at 30.6856 MHz. The spin-lattice relaxation time T_1 was reduced to about 20 min at 4.2K by γ-ray irradiation; the spin-spin relaxation time T_2 was 240 μs. The inductance L_i of the input coil was 5.6 nH while the combined inductance L_p of the pick-up coils was 2.5 μH, yielding an effective coupling coefficient $\alpha_e^2 = \alpha^2/(1 + L_p/L_i)$ of about 10^{-3}; here $\alpha^2 \approx 0.6$ is the coupling coefficient between the SQUID and the input

coil. Most of the tests were performed with $R_i \approx 0.2 \, \Omega$, yielding a Q of 2,500 at the ^{35}Cl resonant frequency. Thus, $Q\alpha_e^2$ was of the order of unity, as required by Eq. (5.18) for optimum operation of the amplifier.

In operation, the static current and flux biases of the SQUID were adjusted to maximize the flux-to-voltage transfer coefficient V_ϕ. The voltage gain of the amplifier was calibrated with respect to the emf induced across the pick-up coil by tuning the input circuit away from the ^{35}Cl resonance, and injecting a continuous rf signal into the transmitter coil at the resonant frequency of the input circuit. If we assume that the voltage across the SQUID is sinusoidal in the input flux with period ϕ_o, the output voltage at the fundamental frequency f is proportional to $J_1(2\pi\phi/\phi_o)$, where $\phi(f)$ is the amplitude of the flux and J_1 the Bessel function of the first order. The first zero of J_1 thus defines the value of ϕ in terms of ϕ_o. We then reduced the applied rf signal to produce a flux amplitude of $\phi_o/20$ at the SQUID, and measured the output voltage. Knowing the values of R_i from the measurement of Q, and the mutual inductance between the SQUID and the input coil, we obtained the required calibration. As a check on this calibration, we also made an absolute calibration of the NQR signal. The calibrations agreed to within 5%. At 4.2K with a Q of 2,500, the voltage gain was 120, and the overall system noise temperature, including the Nyquist noise from R_i, was 6 ± 1K. The power dynamic range in the 12 kHz bandwidth of the tuned circuit was about 3,300, in good agreement with the value of 6 Q/T predicted by Eq. (5.21).

Figure 7.2 illustrates the mixed-down signals that follow an rf pulse in the absence of the Q-spoiler. The rf signal and the resonant frequency of the tuned circuit were at the resonance of the ^{35}Cl nuclei.

(a) (b)
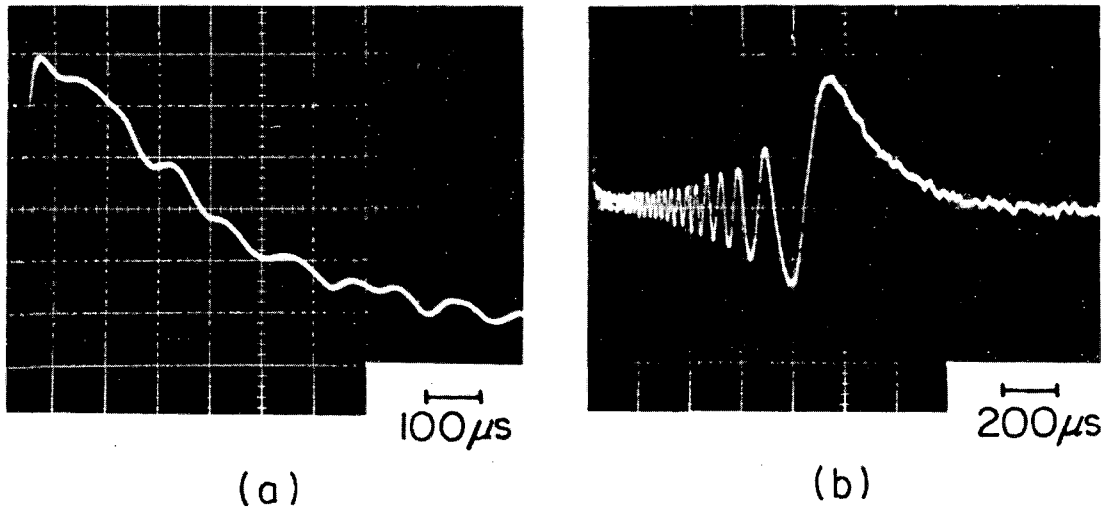
XBB 855-4157

Fig. 7.2 Oscilloscope traces of free-induction decay of ^{35}Cl in the absence of the Q-spoiler: (a) small signal ($\Phi \ll \Phi_0$), (b) large signal ($\Phi \gg \Phi_0$).

Figure 7.2(a) shows a single oscilloscope trace of the free induction decay following an initial tipping angle of 2×10^{-4} rad. The initial rms voltage induced across the pick-up coil was about 20 nV in a bandwidth of 10 kHz. Figure 7.2(b) shows the oscillatory response of the SQUID to a large signal ($\Phi \gg \Phi_0$) resulting from a tipping angle of about 0.16 rad. As mentioned in the previous paragraph, we expect the output voltage at the fundamental frequency f to be proportional to $J_1(2\pi\Phi/\Phi_0)$, where J_1 is the first-order Bessel function. As the amplitude of the input signal decays exponentially, we observe the predicted behavior. By measuring the spin tipping angle required to obtain a signal-to-noise ratio of unity, we determined that the minimum number of ^{35}Cl spins observable with a single pulse in a bandwidth of 10 kHz was about 2×10^{16}. This is equivalent to about 2×10^{16} nuclear Bohr magnetons. For a $\pi/2$-pulse, the signal-to-noise ratio in the same bandwidth decayed to unity after approximately $11T_2 \approx 2.6$ ms.

Figure 7.3 illustrates the effect of the Q-spoiler on the ring-down time of the tuned circuit after the rf pulse. The upper trace on each photograph is the input pulse, while the lower is the mixed-down output signal. The traces were triggered by the onset of the rf pulse. These measurements were performed with the rf frequency and the resonant frequency of the tuned circuit about 150 kHz below the ^{35}Cl resonance to reduce interference between the NQR signal and the ring-down of the tuned circuit. The Q was 2,500, corresponding to a voltage ring-down time constant, τ, of about 26 μs at 30.5 MHz. Figure 7.3(a) shows the response to a rf pulse corresponding to a peak-to-peak magnetic field of about 5 μT at the sample, in the absence of the Q-spoiler. The time for the tuned circuit to recover is about 250 μs or 10 τ. Figure 7.3(b)
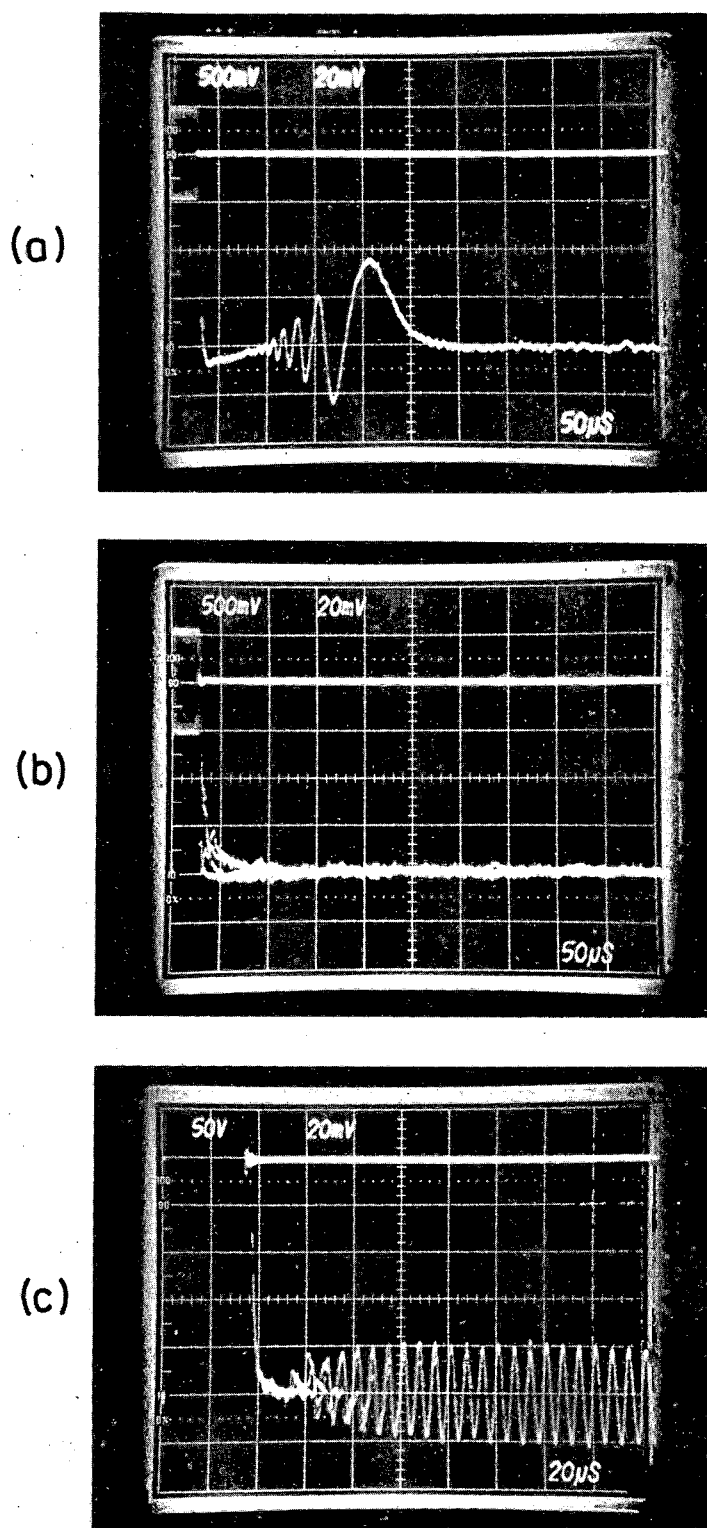
Fig. 7.3 Oscilloscope traces showing ring-down of tuned circuit (lower traces) following the rf pulse (upper traces), with Q = 2,500: (a) without Q-spoiler; (b) and (c) with Q-spoiler. Rf pulses correspond to peak-to-peak pulses of 5 μT in (a) and (b) and to 5 mT in (c). The rf pulse in (c) is off-scale. XBB 853-2203

shows the response to the same rf pulse in the presence of the Q-spoiler, with its critical current reduced by a magnetic field: The recovery time has been reduced to about 50 μs or 2 τ. More importantly from a practical point of view, Fig. 7.3(c) demonstrates that for a much larger rf pulse, about 5 mT peak-to-peak, the recovery time is still only about 50 μs. Incidentally, the system is so sensitive that we can now observe the NQR signal beating with the reference frequency, even though the former is about 12 bandwidths away from the resonant frequency of the tuned circuit.

The Q-spoiler was also tested on a tuned circuit with a Q of 100, corresponding to τ = 1 μs. With an input pulse of 1.5 mT peak-to-peak, the overall recovery time was reduced from 17 μs to about 4 μs, as illustrated in Fig. 7.4.

4. Conclusion

In summary, we have developed a small-signal amplifier for NQR based on a dc SQUID that combines a very high sensitivity with a good tolerance for large rf pulses. We emphasize, however, that the SQUID as a linear amplifier is limited to small signals ($<$ 0.2 μA rms) unless one unfolds the output signal from the oscillatory response illustrated in Fig. 7.2(b). The system offers several advantages over conventional systems with room temperature amplifiers: (i) an improvement in voltage resolution of 1 to 2 orders of magnitude, due to both the low noise temperature of the SQUID and the fact that one may use a high Q; (ii) the elimination of any amplifier dead-time, since the SQUID itself recovers from the rf pulse within a few Josephson oscillations ($<$ 1 ns); (iii) the elimination of losses in the tuned circuit arising from the
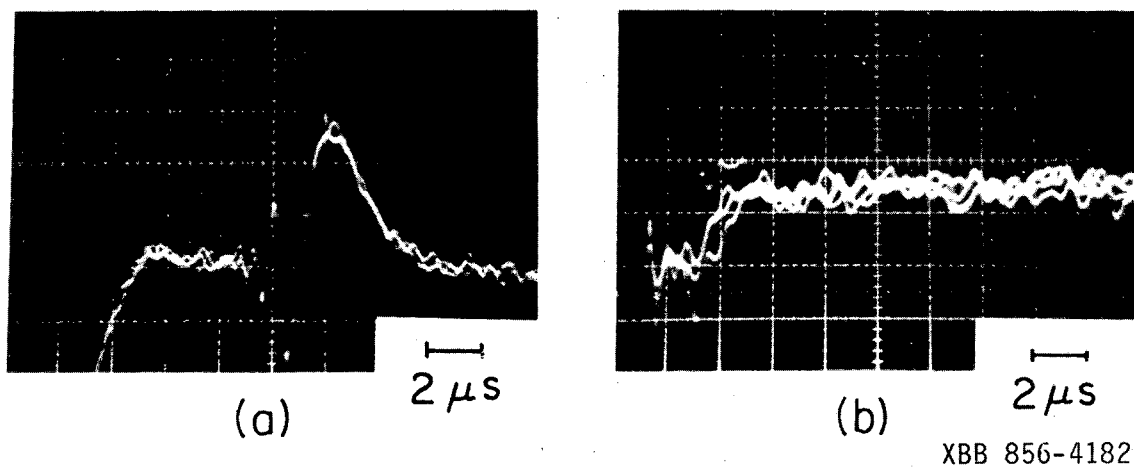
(a)   2 μs   (b)   2 μs

XBB 856-4182

Fig. 7.4   Oscilloscope traces showing ring-down of tuned circuit with Q = 100: (a) without Q-spoiler; (b) with Q-spoiler. Rf pulses correspond to peak-to-peak pulses of 1.5 mT . The traces are triggered at the end of the rf pulses.

cable connecting it to a room temperature amplifier; and (iv) a wide tuning range, from about 1 to 300 MHz. In addition, we have developed a novel Q-spoiler consisting of a series array of hysteretic Josephson tunnel junctions. The Q-spoiler both protects the SQUID and reduces the ring-down time of the tuned circuit after the rf pulse by a substantial factor. The recovery time of the circuit could probably be reduced even further by applying a pulse of magnetic field to the junctions to reduce their critical current to zero until just after the rf pulse has been turned off. We note also that the Q-spoiler could be used in conjunction with any low temperature circuit for the detection of pulsed magnetic resonance, whether or not the amplifier incorporates a SQUID. Finally, a similar system to the one described here could readily be used for NMR, with the proviso that the SQUID would have to be shielded from the static magnetic field applied to the sample and pick-up coils.

CHAPTER VIII

NOISE-NQR AND NUCLEAR SPIN FLUCTUATIONS

1. Introduction

In his pioneering paper on nuclear induction, F. Bloch (1946) noted that in the absence of any external rf driving field a sample of N spins of magnetic moment μ contained in a pick-up coil would induce very small voltage fluctuations proportional to $N^{1/2}\mu$. In this chapter (Sleator et al., 1985) we report the observation of these temperature-independent fluctuations at liquid ^{4}He temperatures arising from the ^{35}Cl nuclei in NaClO$_3$ at the nuclear quadrupole resonance frequency of about 30 MHz.

2. Theory

In the experiment, a sample of nuclear spins is placed in the inductor L_p of a tuned LCR circuit and the spectral density of the current fluctuations is measured over the bandwidth of the circuit. The circuit resistance R_i produces a Nyquist voltage noise and therefore a current noise that, in the absence of a sample, has a Lorentzian spectral density. The presence of the sample is found to modify the shape of this noise power spectrum in the region of the NQR frequency. The influence of the sample is determined from its complex spin susceptibility (Slichter, 1980) $\chi(\omega) = \chi'(\omega) - j\chi''(\omega)$, where χ' and χ'' are the dispersion and absorption. The complex impedance of the coil in the presence of the sample is written as

$$Z_p' = j\omega L_p' = j\omega L_p[1 + 4\pi\xi\chi(\omega)] \qquad (8.1a)$$

$$= j\omega[L_p + L_s(\omega)] + R_s(\omega), \qquad (8.1b)$$

where $\xi = \mathcal{V}_s/\mathcal{V}_c$ is the sample filling factor; $\mathcal{V}_s$ and $\mathcal{V}_c$ are the volume of the sample and the pick-up coil. The added spin inductance $L_s = 4\pi\xi L_p\chi'$ shifts the circuit resonant frequency, while the added spin resistance $R_s = 4\pi\xi\omega L_p\chi''$ modifies the damping of the circuit and acts as a source of Nyquist noise. This noise is due to spin fluctuations in the transverse direction. To observe these fluctuations in a reasonable averaging time one requires, first, that R_s/R_i be not too small, and, second, that the noise current be measured by an amplifier with a noise temperature comparable with or smaller than the bath temperature T.

We can compute the Nyquist noise generated by the spins in terms of the microscopic parameters of the sample. Since the NQR sample is equivalent to a two-level system (Bloom et al., 1955), we take as a model an ensemble of spins in an external magnetic field $H_z\hat{z}$ with spin $I = 1/2$, spin density $n = N/\mathcal{V}_s$, and Larmor frequency $\omega_s/2\pi = \Upsilon H_z/2$, where Υ is the gyromagnetic ratio. The axis of the pick-up coil is along the x-direction. We ascribe a spin temperature T_s to the magnetization

$$M_z = (n\Upsilon\hbar/2)\tanh(\hbar\omega_s/2k_B T_s). \qquad (8.2)$$

We assume that Bloch's equations apply, so that $\chi'' = \chi'/\Delta\omega T_2$ is given by

$$\chi''(\omega) = M_z\Upsilon T_2/2[1 + (\Delta\omega)^2 T_2^2], \qquad (8.3)$$

where $\Delta\omega = \omega_s - \omega$, and the linewidth is given by $\Delta f_s = 1/\pi T_2$. The spectral density of the Nyquist noise voltage produced by R_s is (Callen and

Welton, 1951)

$$S_v^S(\omega) = \frac{2}{\pi} R_S \frac{\hbar\omega}{2} \coth\left(\frac{\hbar\omega}{2k_BT}\right). \tag{8.4}$$

Combining Eqs. (8.2)-(8.4) with $R_S = 4\pi\xi\omega L_p\chi''$, and neglecting terms of order $\Delta\omega/\omega_S \ll 1$, we obtain

$$S_v^S(\omega) = \frac{\xi L_p\omega_S^2 n\gamma^2\hbar^2 T_2}{1 + (\Delta\omega)^2 T_2^2}. \tag{8.5}$$

Remarkably, because of the cancellation of the hyperbolic terms in Eqs. (8.2) and (8.4), $S_v^S(\omega)$ is independent of temperature throughout both the quantum ($\hbar\omega \gg k_BT_S$) and classical ($\hbar\omega \ll k_BT_S$) regimes for a two-level system. This temperature independence can be understood in a different way by applying Faraday's law of induction to obtain the total mean square voltage $\langle V_S^2\rangle = 4\pi\xi L_p\omega_S^2\mathcal{V}_S\langle M_X^2\rangle$ across the coil in terms of the mean square magnetization $\langle M_X^2\rangle$. For a sample with N spins, $\langle M_X^2\rangle = N\langle\mu_X^2\rangle/\mathcal{V}_S^2 = n\gamma^2\hbar^2\langle I_X^2\rangle/\mathcal{V}_S$, where the magnetic moment of a single spin is $\mu_X = \gamma\hbar I_X$ and $\langle I_X^2\rangle = 1/4$ for spin $I = 1/2$. Making these substitutions, we find $\langle V_S^2\rangle = \pi\xi L_p\omega_S^2 n\gamma^2\hbar^2$, which is just $\int_{-\infty}^{+\infty} S_v^S(\omega)d\omega$.

3. Experiment

The configuration of the experiment is shown in Fig. 8.1. The sample is contained in a superconducting coil L_p which is in series with a capacitor C_i that can be adjusted from outside the cryostat. Also in series is the 4-turn input coil of a SQUID amplifier which measures the current fluctuations in the tuned circuit coupled to the sample. The resistance R_i represents contact resistance and losses in the capacitor. The output from the SQUID is recorded by a spectrum analyzer interfaced
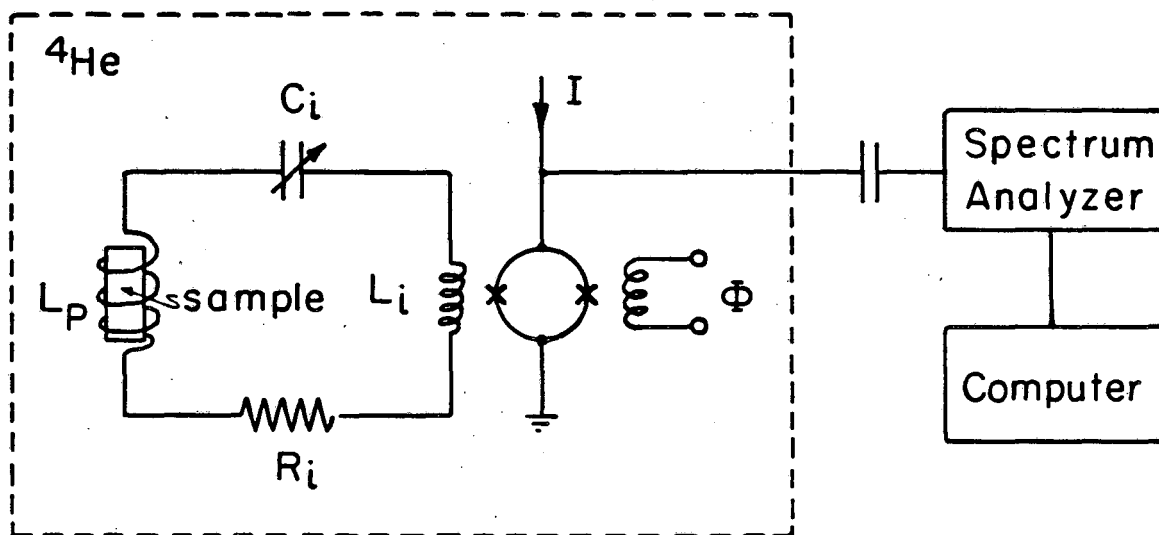
XBL 856-6348

Fig. 8.1 Experimental configuration. Components in dashed box are immersed in liquid ^{4}He.

to a computer.

Noise measurements were made on 0.63 cm^3 of powdered NaClO$_3$, with a filling factor $\xi = 0.35$. The ^{35}Cl nucleus with I = 3/2 has two doubly degenerate energy levels with a transition frequency at 1.5K of $\omega_s/2\pi$ = 30.6857 MHz and a transverse relaxation time T$_2$ = 240 μs corresponding to a linewidth Δf_s = 1.3 kHz. We neglect departures from ideal behavior that occur in a solid, for example, inhomogeneous broadening, and assume that χ has the form given by Eq. (8.3) with the value of T$_2$ given above.

We carried out measurements for two cases. In the first, the spin-lattice relaxation time T$_1$ of the sample was reduced from the order of days to 20 min by γ-ray irradiation of the sample, and the spins were allowed to reach equilibrium (T$_s$ = T) with the helium bath at 1.5K. In the high temperature limit $\hbar\omega \ll k_BT$, the spectral density of the current noise in the input circuit is given by

$$S_I(\omega)\Big|_{T_s=T} = \frac{(2/\pi)k_BT[R_i + R_s(\omega)]}{[R_i + R_s(\omega)]^2 + |X|^2} , \qquad (8.6)$$

where $X = j\omega[L_p + L_i + L_s(\omega)] - j/\omega C_i$. When the circuit is tuned exactly to the Larmor frequency ($\omega = [(L_p + L_i)C_i]^{-1/2}$), Eq. (8.6) reduces approximately to $2k_BT/\pi[R_i + R_s(\omega)]$ near resonance if we assume that Δf_s is much less than the circuit bandwidth Δf_c. Under these conditions the effect of the spins is to produce a "dip" in the spectral density as ω is scanned through the NQR frequency and $R_s(\omega)$ passes through a maximum. An example of such data, averaged over 3 hours, is shown in Fig. 8.2; each of the 1,001 data points was averaged over a bandwidth of about 300 Hz. The minimum of the dip occurs at the ^{35}Cl NQR frequency (indicated by an arrow), which was measured in a separate, pulsed NQR experiment at the same temperature. Taking into account impedance reflected from
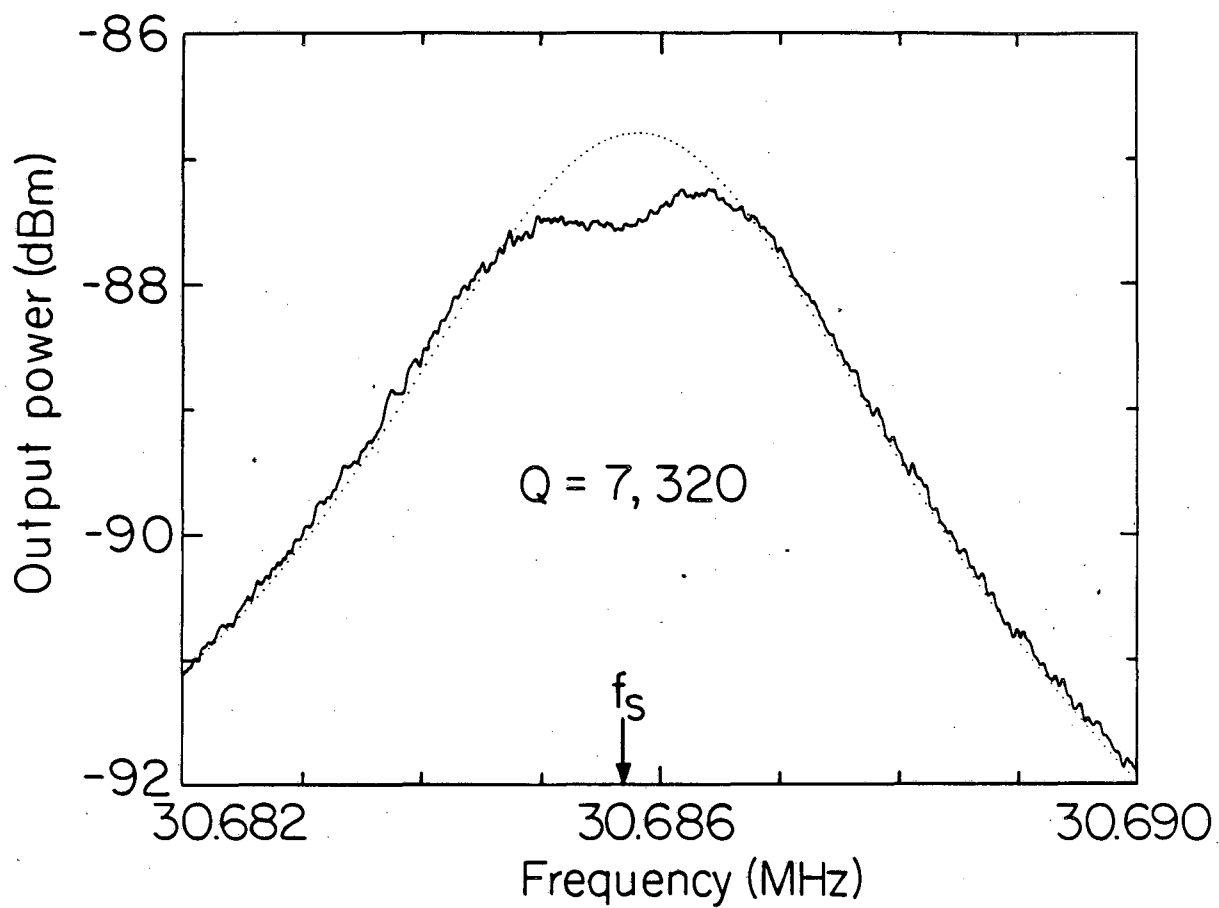
XBL856-6338

Fig. 8.2 Spectral density of noise current for a $NaClO_3$ sample in ther-
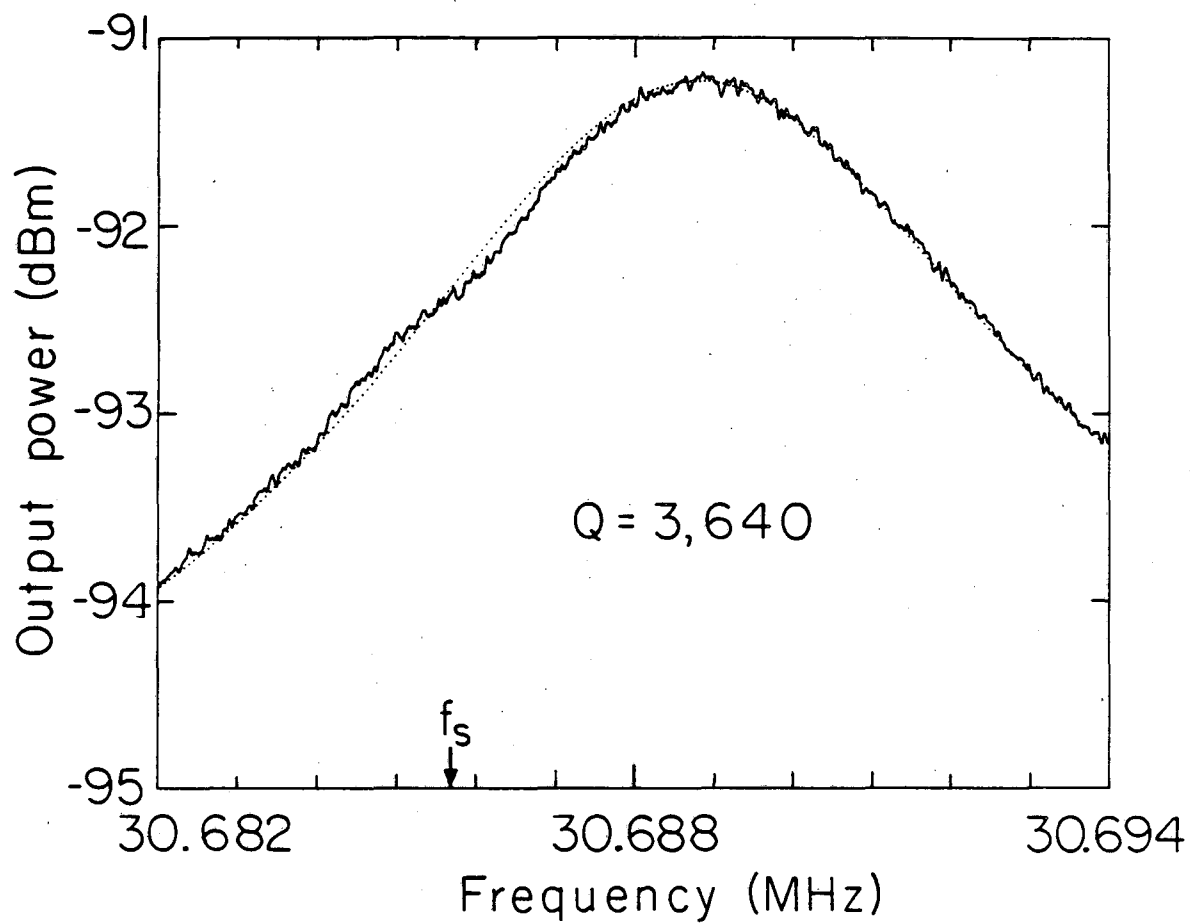mal equilibrium at 1.5K.

the SQUID, we fit the data to Eq. (8.6), and find good agreement with the parameters ω_s and T_2 measured separately. The data are consistent with the values $Q = 7,310$ and $R_s(\omega_s)/R_i = 0.12$, where Q is the quality factor of the circuit in the absence of the sample. These values lead to $R_s(\omega_s)/R_i Q = 4\pi\xi\chi''(\omega_s) = 1.6 \times 10^{-5}$. The dotted line in Fig. 8.2 indicates the response we would expect from this fit in the absence of the sample.

Fig. 8.3 shows a second set of data obtained when the circuit resonance is tuned away from the spin transition frequency. Under these conditions the effects of spin absorption, dispersion and noise combine to produce a "wiggle" in the spectral density. From a fit to Eq. (8.6), we obtain $Q = 3,640$, $R_s(\omega_s)/R_i = 0.07$ and $4\pi\xi\chi''(\omega_s) = 1.9 \times 10^{-5}$. The slight discrepancy with the previous data is due to the limited precision in $R_s(\omega_s)/R_i$.

In the second case, the spins of a sample of $NaClO_3$ with an extremely long T_1 (days) were saturated by applying continuous rf excitation at resonance. After the excitation was turned off, the spectral density was measured over a time much less than T_1. A saturated sample has zero spin population difference, so that $M_z = \chi = R_s = L_s = 0$ and $T_s = \infty$. However, according to Eq. (8.5), the product $R_s(\omega)T_s$ (for $\hbar\omega \ll k_B T$) is independent of T_s for a given frequency. The spectral density of the current becomes

$$S_I(\omega)\Big|_{T_s=\infty} = \frac{(2/\pi)k_B[R_i T + R_s(\omega)T_s]}{R_i^2 + [\omega(L_p + L_i) - 1/\omega C_i]^2} . \qquad (8.7)$$

Thus, one would expect to observe a "bump" in the spectral response arising from the term $R_s T_s$ in the numerator of Eq. (8.7). An example of our data, averaged over 7 hours, is shown in Fig. 8.4(a) with the NQR

XBL 858-6535

Fig. 8.3 Spectral density of noise current for a NaClO$_3$ sample in thermal equilibrium at 1.5K.

frequency indicated by an arrow. Fitting the data to Eq. (8.7) we find $Q = 3,430$, $R_s(\omega_s)T_s/R_iT = 0.06$ and $4\pi\xi\chi''(\omega_s) = 1.7 \times 10^{-5}$, a value in good agreement with that obtained in the previous (equilibrium) case. The dotted line indicates the expected power spectrum in the absence of the sample. Figure 8.4(b) shows the excess noise in Fig. 8.4(a) due to the spins, and represents the first observation of nuclear spin noise.

We repeated the same experiment under identical conditions on a powdered sample of $KClO_3$. In this sample the ^{35}Cl nuclei have a nuclear quadrupole resonance at 29.0389 MHz, and a linewidth of about 800 Hz, corresponding to a transverse relaxation time $T_2 \approx 400\mu s$. The result is shown in Fig. 8.5. From a fit to Eq. (8.7) we obtain $Q = 5,230$, $R_s(\omega_s)T_s/R_iT = 0.10$ and hence $4\pi\xi\chi''(\omega_s) = 1.9 \times 10^{-5}$.

4. Comments

To discuss our results, we note that the spin system at temperature T_s is coupled to the resistance R_i at bath temperature T by absorbing noise power P_R generated by R_i, and simultaneously emitting power P_s into R_i. The net power flow $\Delta P = P_s - P_R$ into R_i (assuming $\Delta f_s \ll \Delta f_c$ and $\hbar\omega \ll k_BT$) is

$$\Delta P = \int_{-\infty}^{\infty} \frac{2k_BR_iR_s(\omega)}{\pi[R_i + R_s(\omega)]^2} (T_s - T)d\omega. \qquad (8.8)$$

Alternatively, we can derive this expression in terms of the dynamics of the spin system if we express the power ΔP in terms of Bloch's equations, modified to include the effect of the circuit (radiation damping; Bloom, 1957). For $R_s \ll R_i$ we find

$$\Delta P = \gamma_s H_z dM_z/dt$$
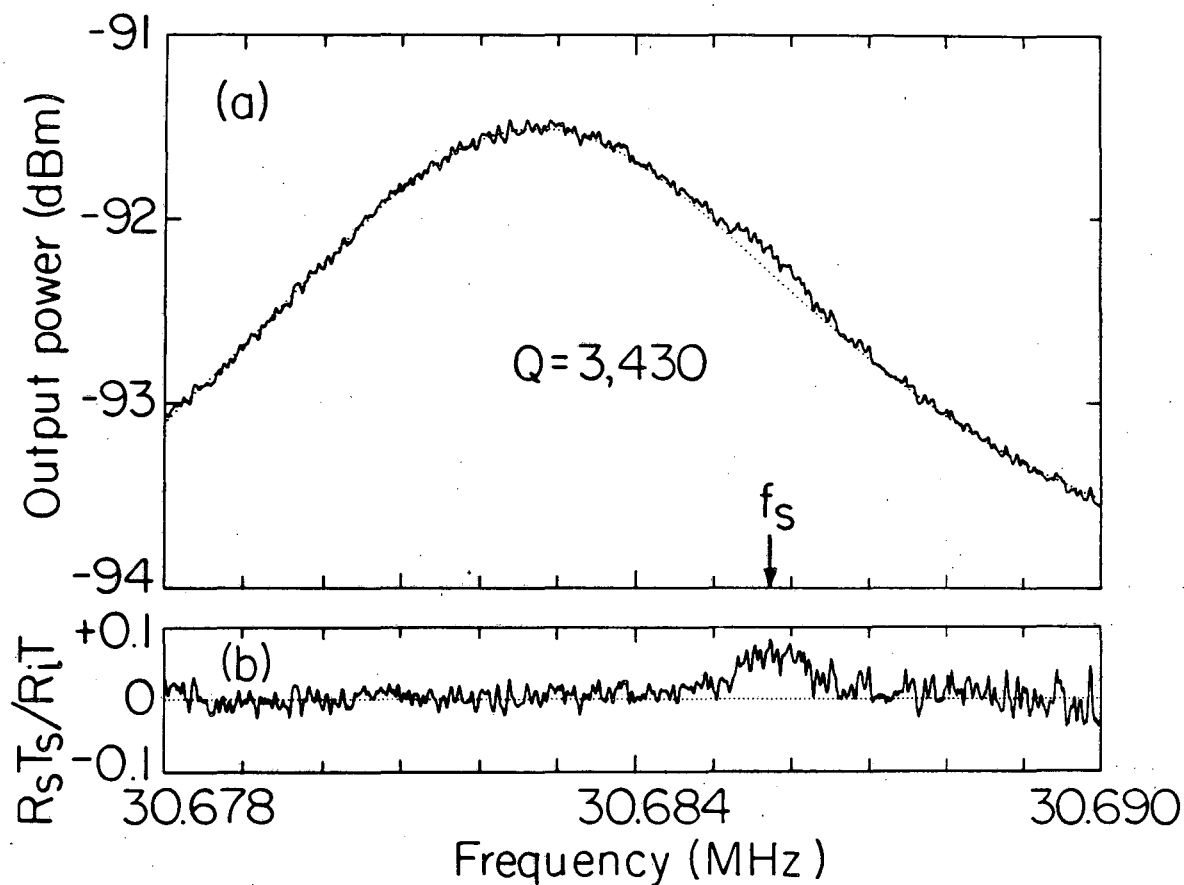
Fig. 8.4 Spectral density of (a) noise current for a $NaClO_3$ sample with saturated spins ($T_s = \infty$), and (b) nuclear spin noise of $NaClO_3$ sample obtained from (a).

XBL 856-6339
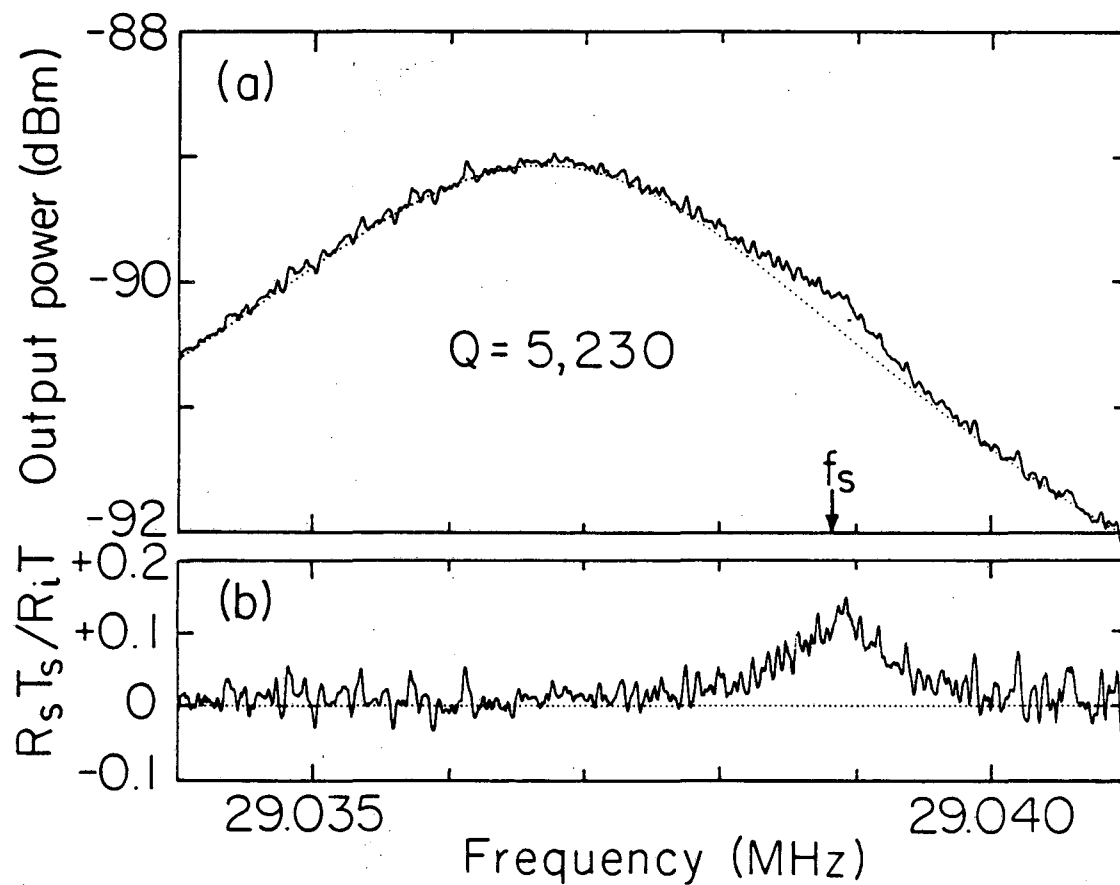
XBL 858-6534

Fig. 8.5 Spectral density of (a) noise current for a $KClO_3$ sample with saturated spins ($T_s = \infty$), and (b) nuclear spin noise of $KClO_3$ sample obtained from (a).

$$= 4\pi\xi\mathcal{V}_s Q\omega_s \langle M_x^2 \rangle - \mathcal{V}_s \omega_s S_H(\omega_s) \int_{-\infty}^{\infty} \chi'' d\omega, \qquad (8.9)$$

where $\langle M_x^2 \rangle = n\gamma^2 \hbar^2 / 4\mathcal{V}_s$. The first term on the right-hand side of Eq. (8.9) is the power P_s emitted by the spins into R_i and arises from the radiation damping·of fluctuations in M_x. This power can also be expressed as $P_s = 2k_B T_s / \tau_R$ (for $k_B T_s \gg \hbar\omega$) where $1/\tau_R = 2\pi\xi\gamma M_z Q$ is the radiation damping rate (Bloom, 1957; Bloembergen and Pound, 1954). The second term on the right-hand side of Eq. (8.9) represents the absorption by the spins of the magnetic field energy produced by noise in R_i at temperature T. The spectral density $S_H(\omega_s)$ of the magnetic field H_x is determined from

$$\frac{S_H(\omega_s)}{8\pi} = \mathcal{D}_c(\omega_s) \frac{\hbar\omega_s}{4} \coth\left(\frac{\hbar\omega_s}{2k_B T}\right), \qquad (8.10)$$

where $\mathcal{D}_c(\omega_s) = 2Q/\pi\omega_s \mathcal{V}_c$ is the density of states for the single cavity mode. With some manipulation Eq. (8.9) results in the familiar form of Einstein's detailed balance equation

$$\Delta P = (\hbar\omega_s/2) d\Delta N(T_s)/dt$$

$$= \frac{\hbar\omega_s}{2} A\left[N - \Delta N(T_s)\coth\left(\frac{\hbar\omega_s}{2k_B T}\right)\right], \qquad (8.11)$$

where $\Delta N(T_s)$ is the total spin population difference and $A = 2\pi Q\hbar\gamma^2/\mathcal{V}_c$ is the spontaneous emission rate into a resonant cavity (Purcell, 1946; Gabrielse and Dehmelt, 1985). Eqs. (8.9) and (8.11) are identical to Eq. (8.8) to first order in R_s/R_i ($\ll 1$). To obtain agreement to higher

order, we take into account the effect of R_s on the density of states by writing $Q = \omega(L_p + L_i)R_i/(R_i + R_s)^2$ in the steps leading to Eq. (8.9). This yields a result in agreement with Eq. (8.8) to second order in R_s/R_i. The equivalence of Eqs. (8.9) and (8.11) demonstrates the close connection between spin fluctuations and spontaneous emission and shows that the bumps observed in Figs. 8.4 and 8.5 represent spontaneous emission from the spins into the circuit.

Although for our experiment the spontaneous emission rate for one spin is extremely low, $A = 2 \times 10^{-16} \sec^{-1}$ (about one spin flip in 10^8 years), since $N = 2 \times 10^{21}$ the total emission rate $(NA/2)$ is $\approx 2 \times 10^5$ $\sec^{-1}$, corresponding to a total emissive power $P_s \approx 5 \times 10^{-21} W$. This power is about 5% of the Nyquist noise power $4k_BT/\pi T_2 \approx 10^{-19}$ W generated in the bandwidth of the spin noise $1/\pi T_2$.

In conclusion, we note that the value of T_1 does not affect the noise measurements except to determine the rate at which the sample reaches thermal equilibrium. This longitudinal relaxation process would induce very small voltage fluctuations about zero frequency across a pick-up coil with its axis parallel to the direction of the spin polarization. Finally, this method of observing fluctuations from saturated spins provides a means for determining the resonant frequency and linewidth in systems where T_1 is impractically long for conventional techniques.

REFERENCES

1) Berthel, K.H., and F. Dettmann, 1984, Planar thin-film dc SQUID, fabrication and measuring system, Physica 126 B+C, 197.

2) Bishop, J.H., E.C. Hirschkoff, and J.C. Wheatley, 1971, Very-low-temperature static magnetic properties of certain metals possibly useful as magnetic thermometers, J. Low Temp. Phys. 5, 607.

3) Bloch, F., 1946, Nuclear induction, Phys. Rev. 70, 460.

4) Bloembergen, N., and R.V. Pound, 1954, Radiation damping in magnetic resonance experiments, Phys. Rev. 95, 9.

5) Bloom, S., 1957, Effect of radiation damping on spin dynamics, J. Appl. Phys. 28, 800.

6) Bloom, M., E.L. Hahn, and B. Herzog, 1955, Free magnetic induction in nuclear quadrupole resonance, Phys. Rev. 97, 1699.

7) Boughn, S.P., W.N. Fairbank, R.P. Giffard, J.N. Hollenhorst, M.S. McAshan, H.J. Paik, and R.C. Taber, 1977, Observation of mechanical Nyquist noise in a cryogenic gravitational-wave antenna, Phys. Rev. Lett. 38, 454.

8) Bruines, J.J.P., V.J. de Waal, and J.E. Mooij, 1982, Comment on: "Dc SQUID: Noise and optimization" by Tesche and Clarke, J. Low Temp. Phys. 46, 383.

9) Callen, H.B., and T.A. Welton, 1951, Irreversibility and generalized noise, Phys. Rev. 83, 34.

10) Carelli, P., and V. Foglietti, 1985, Problems in coupling a dc SQUID to the external world, IEEE Trans. Magn. MAG-21, 424.

11) Chamberlin, R.V., L.A. Moberly, and O.G. Symko, 1979, High-sensitivity magnetic resonance by SQUID detection, J. Low Temp. Phys. 35, 337.

12) Claassen, J.H., 1975, Coupling considerations for SQUID devices, J. Appl. Phys. 46, 2286.

13) Clarke, J., C.D. Tesche, and R.P. Giffard, 1979, Optimization of dc SQUID voltmeter and magnetometer circuits, J. Low Temp. Phys. 37, 405.

14) Day, E.P., 1972, Detection of NMR using a Josephson-junction magnetometer, Phys. Rev. Lett. 29, 540.

15) Dettman, F., W. Richter, G. Albrecht and W. Zahn, 1979, Monolithic thin-film dc SQUID, Phys. Stat. Sol.(a) 51, K185.

16) de Waal, V.J., T.M. Klapwijk, and P. van den Hamer, 1983, High-performance dc SQUIDs with submicrometer niobium Josephson-junctions, J. Low Temp. Phys. 53, 287.

17) de Waal, V.J., P. Schrijner, and R. Llurba, 1984, Simulation and optimization of a dc SQUID with finite capacitance, J. Low Temp. Phys. 54, 215.

18) Ehnholm, G.J., J.P. Ekstrom, M.T. Loponen, and J.K. Soimi, 1979, Transversal SQUID NMR, Cryogenics 19, 673.

19) Freeman, M.R., M.L. Roukes, R.S. Germain, and R.C. Richardson, 1984, dc SQUID small signal amplifiers for NMR, Physica 126 B+C, 267.

20) Gabrielse, G., and H. Dehmelt, 1985, Observation of inhibited spontaneous emission, Phys. Rev. Lett. 55, 67.

21) Germain, R.S., M.L. Roukes, M.R. Freeman, R.C. Richardson, and M.B. Ketchen, 1984, Source impedance effects on dc SQUID performance, Physica 126 B+C, 203.

22) Giffard, R.P., and J.N. Hollenhorst, 1978, Measurement of forward and reverse signal transfer coefficients for an rf-biased SQUID, Appl. Phys. Lett. 32, 767. .

23) Henry, R.W., and D.E. Prober, 1981, Electronic analogs of double-junction and single-junction SQUIDs, Rev. Sci. Instr. 52, 902.

24) Hilbert, C., and J. Clarke, 1983, Radio-frequency amplifier based on a dc superconducting quantum interference device, Appl. Phys. Lett. 43, 694.

25) Hilbert, C., and J. Clarke, 1984, Dynamic input impedance of an amplifier based on a dc superconducting quantum interference device, Appl. Phys. Lett. 45, 799.

26) Hilbert, C., and J. Clarke, 1985a, dc SQUID as a tuned radio-frequency amplifier, IEEE Trans. Magn. MAG-21, 1029.

27) Hilbert, C., and J. Clarke, 1985b, Measurements of the dynamic input impedance of a dc SQUID, J. Low Temp. Phys. 61, 237.

28) Hilbert, C., and J. Clarke, 1985c, dc SQUIDs as radio-frequency amplifiers, J. Low Temp. Phys. 61, 263.

29) Hilbert, C., J. Clarke, T. Sleator, and E.L. Hahn, 1985, Nuclear quadrupole resonance detected at 30 MHz with a dc superconducting quantum interference device, Appl. Phys. Lett. 47, 637.

30) Hirschkoff, E.C., O.G. Symko, L.L. Vant-Hull, and J.C. Wheatley, 1971, Observation of the static nuclear magnetism of pure metallic copper in low magnetic fields, J. Low Temp. Phys. 2, 653.

31) Jaklevic, R.C., J. Lambe, A.H. Silver, and J.E. Mercereau, 1964, Quantum interference effects in Josephson tunneling, Phys. Rev. Lett. 12, 159.

32) Jaycox, J.M., 1981, Master's Thesis, MIT.

33) Josephson, B.D., 1962, Possible new effects in superconductive tunneling, Phys. Rev. Lett. 1, 251.

34) Ketchen, M.B., and J.M. Jaycox, 1982, Ultra-low-noise tunnel

junction dc SQUID with a tightly coupled planar input coil, Appl. Phys. Lett. 40, 736.

35) Koch, R.H., 1982, Quantum noise in Josephson junctions and dc SQUIDs, Ph.D. Thesis, University of California, Berkeley.

36) Martinis, J.M., and J. Clarke, 1983, Measurements of current noise in dc SQUIDs, IEEE Trans. Magn. MAG-19, 446.

37) Martinis, J.M., and J. Clarke, 1985, Signal and noise theory for a dc SQUID amplifier, J. Low Temp. Phys. 61.

38) McDonald, D.G., 1984, Power gain of a SQUID amplifier, Appl. Phys. Lett. 44, 556.

39) Meredith, D.J., G.R. Pickett, and O.G. Symko, 1973, Application of a SQUID magnetometer to NMR at low temperatures, J. Low Temp. Phys. 13, 607.

40) Muhlfelder, B., and W.W. Johnson, in "Optical bistability 2", C.M. Bowden, H.M. Gibbs, and S.L. McCall (eds.), Plenum, New York, 375.

41) Muhlfelder, B., J.A. Beall, M.W. Cromar, R.H. Ono, and W.W. Johnson, 1985, Well-coupled low-noise dc SQUIDs, IEEE Trans. Magn. MAG-21, 427.

42) Pegrum, C.M., D. Hutson, G.B. Donaldson, and A. Tugwell, 1985, dc SQUIDs with planar input coils, IEEE Trans. Magn. MAG-21, 1036.

43) Pickens, K.S., D.I. Bolef, M.R. Holland, and R.K. Sundfors, 1984, Superconducting quantum interference device detection of acoustic nuclear quadrupole resonance of ^{121}Sb and ^{123}Sb in antimony metal, Phys. Rev. B30, 3644.

44) Purcell, E.M., 1946, Spontaneous emission probabilities at radio-frequencies, Phys. Rev. 69, 681.

45) Silver, A.H., and J.E. Zimmerman, 1967, Multiple quantum resonance

spectroscopy through weakly connected superconductors, Appl. Phys. Lett. $\underline{10}$, 142.

46) Sleator, T., E.L. Hahn, C. Hilbert, and J. Clarke, 1985, Nuclear spin noise, Phys. Rev. Lett. $\underline{55}$, 1742.

47) Slichter, C.P., 1980, "Principles of magnetic resonance" (2nd ed.), Springer Verlag, New York.

48) Stewart, W.C., 1968, Current-voltage characteristics of Josephson junctions, Appl. Phys. Lett. $\underline{12}$, 277.

49) Suzuki, H., Y. Higashino, and T. Ohtsuka, 1980, SQUID NMR studies of $TmPO_4$, J. Low Temp. Phys. $\underline{41}$, 449.

50) Tesche, C.D., 1982a, Optimization of dc SQUID linear amplifiers and the quantum noise limit, Appl. Phys. Lett. $\underline{41}$, 490.

51) Tesche, C.D., 1982b, Analysis of a double-loop dc SQUID, J. Low Temp. Phys. $\underline{47}$, 385.

52) Tesche, C.D., 1983a, Analysis of strong inductive coupling on dc SQUID systems, IEEE Trans. Magn. $\underline{MAG-19}$, 458.

53) Tesche, C.D., 1983b, Quantum limit constraints on dc SQUID amplifiers, in "Noise in physical systems and 1/f noise", M. Savelli, G. Lecoy, and J.P. Nougier (eds.), North-Holland, Amsterdam, 137.

54) Tesche, C.D., and J. Clarke, 1977, dc SQUID: Noise and optimization, J. Low Temp. Phys. $\underline{29}$, 301.

55) Tesche, C.D., and J. Clarke, 1979, dc SQUID: Current noise, J. Low Temp. Phys. $\underline{37}$, 397.

56) Tesche, C.D., K.H. Brown, A.C. Callegari, M.M. Chen, J.H. Greiner, H.C. Jones, M.B. Ketchen, K.K. Kim, A.W. Kleinsasser, H.A. Notarys, G. Proto, R.H. Wang, and T. Yogi, 1985, Practical dc SQUIDs with extremely low 1/f noise, IEEE Trans. Magn. $\underline{MAG-21}$, 1032.

57) Webb, R.A., 1977, New technique for improved low-temperature SQUID NMR measurements, Rev. Sci. Instr. 48, 1585.

58) Wennberg, A.K.M., L.J. Friedman, and H.M. Bozler, 1984, Pulsed NMR using a dc SQUID, Physica 126 B+C, 265.

59) Zimmerman, J.E., 1971, Sensitivity enhancement of superconducting quantum interference devices through use of fractional-turn loops, J. Appl. Phys. 42, 4483.